ARE STANNERN-GROUP EUCRITES PRODUCTS OF PARTIAL MELT CONTAMINATION? CONSTRAINING THE PETROGENESIS OF THE H.E.D. PARENT BODY THROUGH EXPERIMENTAL PETROLOGY

by

SAMUEL D. CROSSLEY

Bachelor of Science, 2010

Hardin-Simmons University

Abilene, TX

Submitted to the Graduate Faculty of the

College of Science and Engineering

Texas Christian University

in partial fulfillments of the requirements

for the degree of

Master of Science

August 2016

Acknowledgements

When I think back on my experiences at TCU, I am overwhelmed with gratitude for all of the people who made the last two years possible. There are so many that I doubt I would be able to list all of them by name, but I'll do my best for those were most closely involved with this research and with me during all of it.

To those academic professionals who helped me conduct research directly, thank you for taking the time to help me learn how to do research, operate scientific equipment that I'd never even heard of two years ago, interpret results, and expand my academic horizons. Just some names that come to mind here are Dr. Nicole Lunning (thank you for walking me through the experiments, teaching me how to use the SEM, talking with me about meteorites over lunch, and always doing so with patience and understanding that I can only hope to emulate), Dr. Tim McCoy (thanks for your insights, guidance, and lunch that one time that I left my wallet at the museum), Dr. George Morgan (thanks for the hours of helping me with EMPA while listening to jazz on holiday, and thanks for running a lot of those experiments again when the EMP broke down after I left), Munir Humayun and Shuying Yang (thanks for running LA-ICP-MS for us—and for free, at that).

My thesis committee: Dr. Tim McCoy, I'd thank you again, but I don't want to seem unctuous. Dr. Richard Hanson, you have, literally, taught me almost everything that I know about Geology. I came in knowing practically nothing, and now I know marginally more than nothing! Honestly, though, thank you for everything that you put into teaching your classes. They were the most challenging Geology courses I've had, and I loved them. Thanks for swapping stories with me of our adventures through Africa, and for leading the best field trips I've ever been a part of. You make me wish I was a field geologist (and that I could grow a fuller beard). Feel free to put that band name to use (Bulk D and the Magmatic Misfits). Dr. Rhiannon Mayne, I can't thank you enough for the incredible opportunities that you've made available to me. You took a chance on a lackluster student who geeked out at the amazing and totally underrated Monnig Meteorite Collection, and gave me a chance to work with some of the best researchers in the world. Never would I have thought that I'd get to do what I've done over the last two years, much less what we'll continue working on as I move toward a Ph.D. You've changed the direction of my life for the better—thank you so, so much… What? No, I'm not crying… you're crying! Oh, thank you for all the coffee and sweet potato chips, too.

My fellow graduate students: thanks for all the fun times and commiserating! Thanks in particular to Julia Gregory (aka Jules P. McGregory), who took every single class with me, listened to me rant for hours on road trips to conferences, eagerly helped me with math, and froze to death while I played with pretty space rocks in the vault.

My friends and family: I love you. Thanks for just being you. I missed you so much while I was in the Peace Corps, and it gave me a new appreciation for living so close to you (and/or with you) again. I'll miss you terribly while I'm doing my Ph.D. in Maryland.

My dog: Who's a good boy? Well, I think it's time you learned: you were the good boy all along, Erebos. Thank you for listening to me talk out loud about my research, and only occasionally talking back when I hadn't gotten enough sleep.

Lastly, I would like to thank you, the reader. They say that only about 1.5 people on average will ever read your entire thesis, including yourself. Are you up for the challenge? I hope you enjoy it and find it as stimulating as I have.

Sam Crossley

Table of Contents

Vita

Abstract

List of Figures

List of Tables

List of Equations

1.0 Background and Research Goals

Historically, the petrogenesis of basaltic eucrites has not been well-constrained (e.g. Barrat et al., 2007, 2008; Mittlefehldt, 2015). The Stannern-group eucrites, one of three geochemical subgroups of basaltic eucrites, are particularly problematic because they cannot be explained by major competing models of eucrite parent body petrogenesis (e.g. Stolper, 1977; Righter and Drake, 1997; Barrat et al., 2007). Currently, the most widely accepted model asserts that Stannern-group eucrites could have formed via the partial melting of a residual eucritic crust, in which the partial melt product contaminated Main-group eucritic magmas (Barrat et al., 2007). Though generally acknowledged as a plausible explanation for Stannern-group eucrites, the model has never been experimentally verified. Recently, melting experiments have been conducted with eucrites at near-solidus temperatures (Yamaguchi et al., 2013). These experiments did not yield enough partial melt product in some samples to be analyzed. However, expanding upon previous experimental conditions by increasing temperature should yield a greater percent partial melt. The composition can then be analyzed and used to test the currently accepted model of Stannern-group eucrite petrogenesis.

The central focus of this research is to experimentally determine if Stannern-group eucritic compositions can be produced by the assimilation of partial melts of Main-group eucritic crust into typical Main-group eucritic magmas, as suggested by Barrat et al. (2007). We attempted to achieve this goal through the following processes:

- acquisition of a meteorite that is suitable for melting experiments
- establishment of a petrogenetic history of the meteorite
- experimental partial melting of the meteorite
- detailed analyses of major and trace element compositions of the meteorite and experimental partial melts
- calculation of magma mixture compositions

Calculated results that produce compositions within that of the Stannern-group would suggest that the model could be a plausible explanation for the group's anomalous characteristics. A negative result may suggest that Stannern-group eucrite petrogenesis occurred along a different evolutionary path, placing new constraints not only on their petrogenesis, but perhaps on the HED parent body as a whole.

2.0 Introduction

The HED meteorite clan, consisting of howardites, eucrites, and diogenites, is one of the most widely studied groups of achondritic meteorites (Figure 1). Achondrites are meteorites whose parent bodies were originally chondritic in composition (i.e. original material that condensed from the solar nebula) but have undergone extensive melting, completely erasing the spherical chondrules that are texturally diagnostic of primordial chondritic material. Achondrites are sourced from differentiated parent bodies that melted to such an extent that they formed a metallic core (iron meteorites), a mantle, and a crust (achondrites). Howardites are consolidated breccias (rocks sourced from the outermost surficial layer of impact-pulverized crustal material) that are composed of both eucritic and diogenitic clasts (Fredriksson and Keil, 1963). Evidence for howardites as regolith material includes abundant impact melt clasts, enrichment in noble gases due to solar wind implantation, and carbonaceous chondrite xenoliths (e.g. Fredriksson and Keil, 1963). Diogenites are coarse-grained, cumulate orthopyroxenites that formed at depth with respect to howardites and eucrites, and commonly contain minor olivine, clinopyroxene, troilite, chromite, anorthite, and Fe-Ni metal. Eucrites, composed primarily of pyroxene (pigeonite and augite) and plagioclase, can be divided into two groups: gabbroic cumulate eucrites, which precipitated in magma chambers via fractional crystallization, and basaltic eucrites, which rapidly crystallized from surficial lava flows or shallow intrusions (Duke and Silver, 1968). Based on effects of impact processes, eucrites can further divided into monomict breccias, sourced from a single lithologic unit, or polymict breccias, which formed from multiple lithologic units. Geochemical groupings are more complex and will be discussed in section 2.4 (page 12).

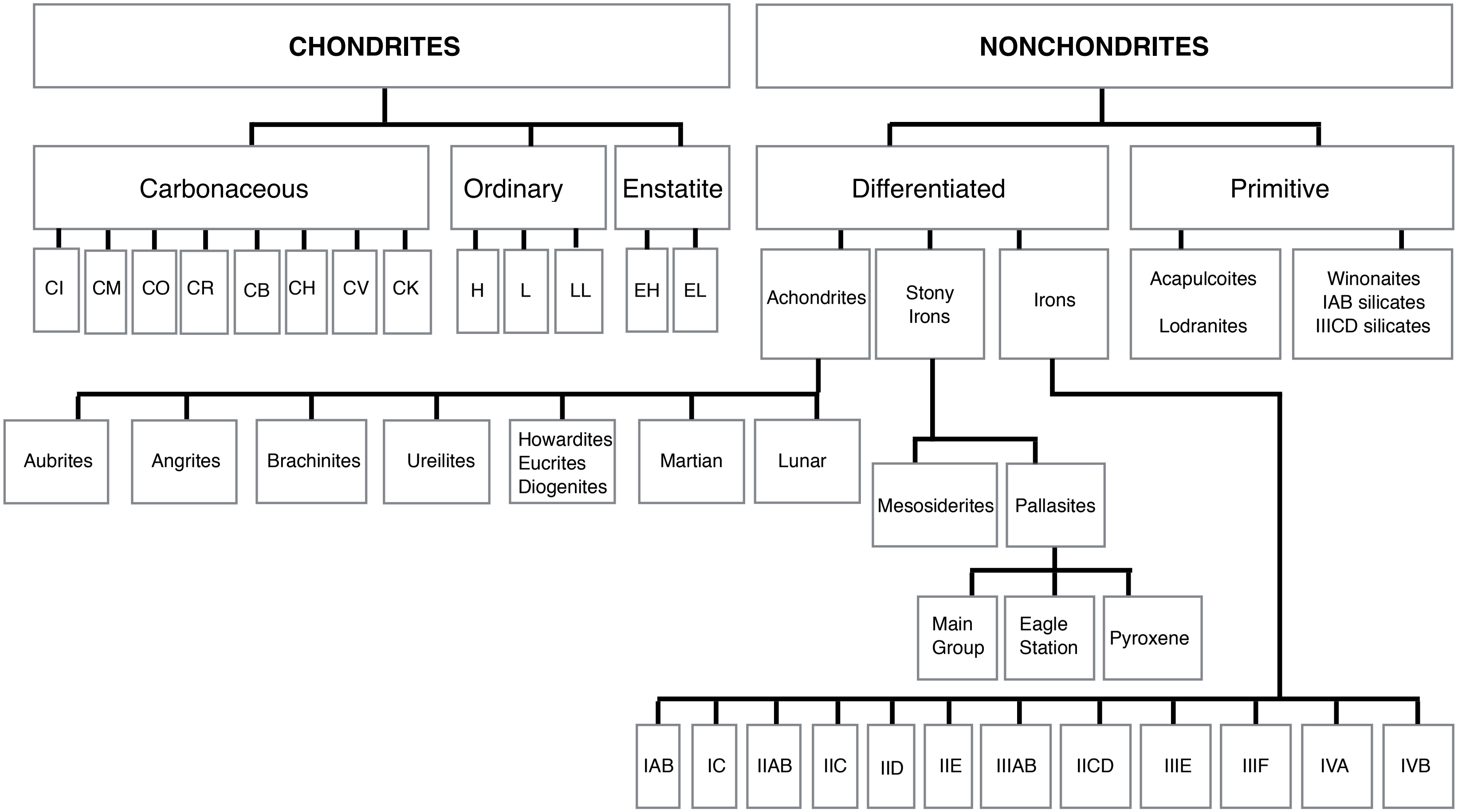

Figure 1: Classification Scheme of Meteorites
This flow chart shows the classification scheme of meteorites after Krot et al. (2014). Meteorite "clans" believed to be sourced from common parent bodies are grouped together in single tabs. Chondrites include relatively unaltered material condensed from the solar nebula, while nonchondrites have undergone varying degrees of subsequent igneous processes. Eucrites, which are the focus of this study, are extensively differentiated material (achondrites) belonging to the HED clan.

2.1 The Association of HED Meteorites within a Single Parent Body

A wealth of evidence has led to the association of howardites, eucrites, and diogenites within a singular parent body, including similar oxygen isotopic compositions (Clayton and Mayeda, 1996), similar Fe/Mn ratios in pyroxenes (e.g. Papike, 1998), polymict breccias (i.e. howardites) containing both diogenitic and eucritic material (Fredriksson and Keil, 1963), and meteorites that are intermediate between eucrites and diogenites (Takeda et al., 1985).

2.1.1 Oxygen Isotopic Compositions of HEDs

Oxygen isotopic compositions in primitive chondrites reveal heterogeneity in the distribution of the three stable isotopes of oxygen: ^{16}O, ^{17}O, and ^{18}O (Clayton et al., 1973). These variations in isotopic composition are inferred to be the products of interactions between gases and dust within the solar nebula, as well as between minerals and fluids within parent bodies (Clayton et al., 1991). However, differentiated planetary bodies, such as the HED parent body, have undergone large-scale melting and homogenization (Greenwood et al., 2005). These processes erase pre-accretionary isotopic data but create distinct isotopic compositional groups (Figure 2) that can be used to distinguish parent bodies from one another (Clayton and Mayeda, 1996). Assuming complete homogenization, any isotopic variations that occur within a body after homogenization are products of mass-dependent fractionation, and in a three-isotope diagram will fall along a slope defined as:

$$\partial^{17}O = 0.52\partial^{18}O, \qquad [1]$$

where $\partial^{X}O = (^{X}O/^{16}O)x1000$. For a specific parent body, the Y-intercept of the resulting line is determined by:

$$\partial^{17}O = 0.52\partial^{18}O + \Delta^{17}O, \qquad [2]$$

where $\Delta^{17}O$ is the offset from from the mass-dependent fractionation line. These values are all normalized to standard mean ocean water (SMOW). For terrestrial and lunar samples, $\Delta^{17}O = 0$, and is ~0.3‰ for martian samples and ~0.24‰ for HEDs (Clayton and Mayeda, 1983). These

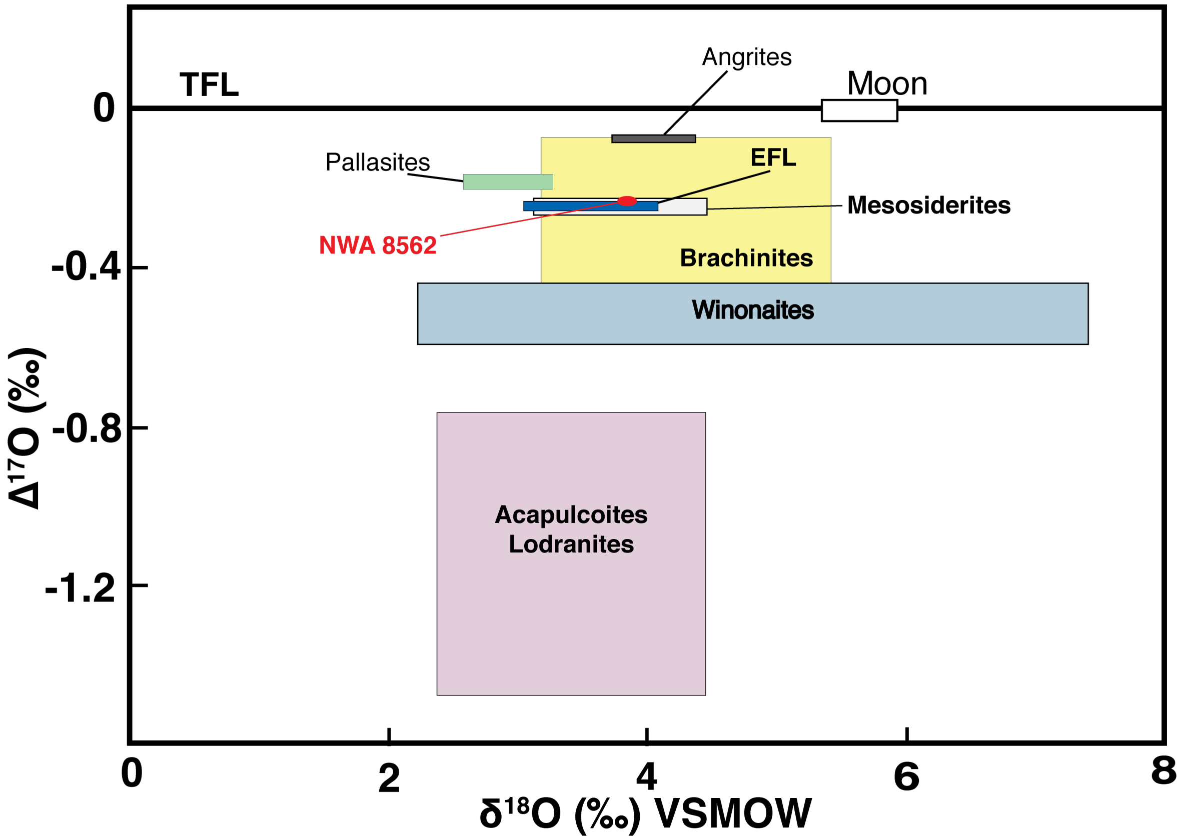

Figure 2: Oxygen Isotope Fractionation Trends
Oxygen isotope fractionation trends are presented for stony-irons, primitive achondrites, and eucrites. Earth oxygen-isotopic ratios are shown by the terrestrial fractionation line (TFL) and HEDs are represented by the eucrite fractionation line (EFL). Data for the eucrite NWA 8562 are from this study. All other data are from Greenwood et al. (2014).

distinct groups suggest that the corresponding parent bodies accreted from different isotopic reservoirs in the solar nebula (Clayton and Mayeda, 1983). Distribution of oxygen isotopes in the solar nebula is not well constrained, and assigning meteorite groups to shared parent bodies can be problematic if done with oxygen isotopic data alone. For example, enstatite chondrites plot along the terrestrial fractionation line, despite being composed of undifferentiated, extremely reduced material (Clayton et al., 1984). Additionally, several groups of iron meteorites fall within error of the HED fractionation line, leading some workers (e.g. Wasson, 2013) to conclude that they originated within the same reservoir in the solar nebula.

2.1.2 Fe/Mn Ratios in HED Pyroxenes

Chemical compositions of minerals from different planetary bodies reflect the chemical reservoirs and thermodynamic conditions in which they formed. Papike (1998) and Papike et al. (2003) found that atomic Fe/Mn ratios in the pyroxenes of basaltic achondrites can be used to distinguish parent bodies. These studies suggested that Fe/Mn variations among parent bodies are controlled by heliocentric distance (Figure 3), with secondary effects according to oxygen fugacity and metal segregation. The role of heliocentric distance relies upon the assumption that Vesta is the parent body for HEDs (evidence for this is reviewed in the following section). Additionally, the correlation between Fe/Mn and heliocentric distance also assumes that sources for basaltic achondrites have not migrated since accreting; however, planetary migration is a common feature in many dynamical models (e.g. Tsiganis et al., 2005). The average Fe/Mn ratio for basaltic eucrites is ~30 (Mayne et al., 2009).

2.2 The Vesta-HED Connection

The HED meteorite clan is particularly valuable to the meteoritical community because, apart from martian and lunar samples (Stolper et al., 1979; Bogard, 1983), it is the only clan of meteorites that has been attributed to a specific extant parent body, the asteroid 4-Vesta (e.g. Consolmagno and Drake, 1977; De Sanctis et al., 2012; McSween et al., 2013a). Vesta orbits

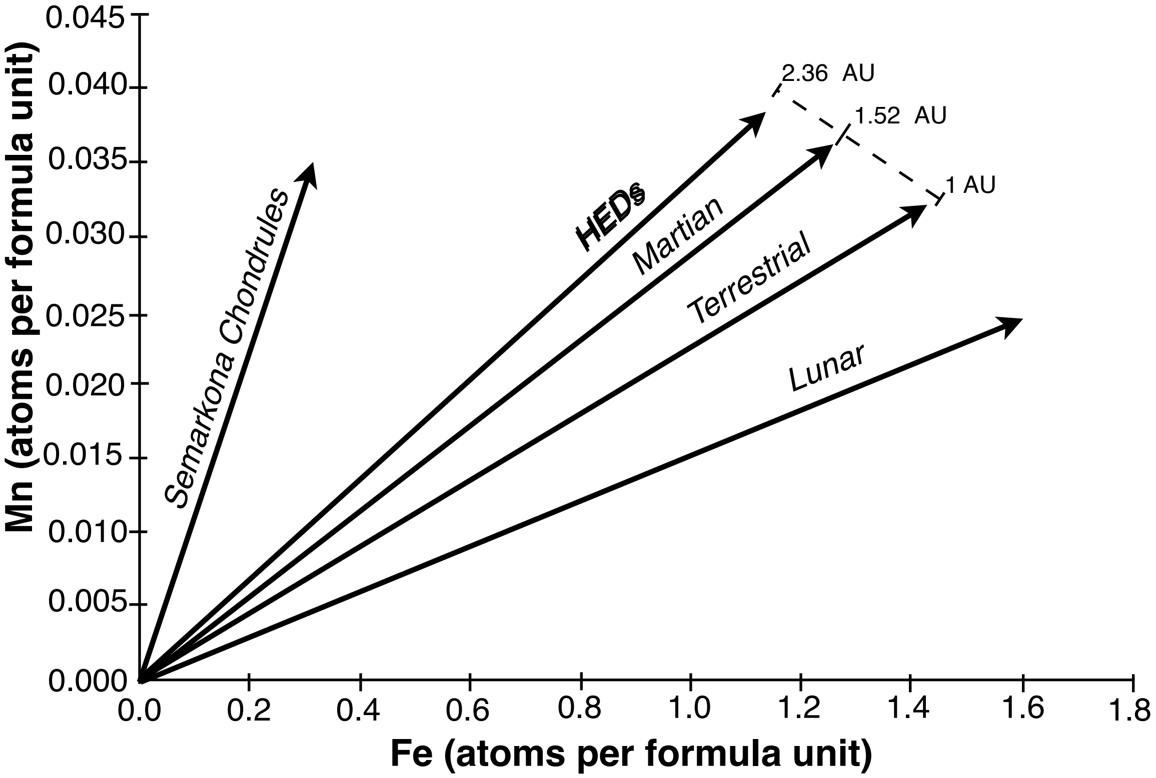

Figure 3: Fe/Mn Ratios for Pyroxenes from Different Parent Bodies
Fe/Mn ratios in pyroxenes can be used as genetic identifiers for meteorite parent bodies. These ratios appear to increase with distance from the Sun (see text), possibly relict from gradational Fe/Mn distribution in the solar nebula. Core formation may also play a role, which could account for discrepancies between the Earth and its moon. Adapted from Papike (1998).

within the inner asteroid belt at a heliocentric distance of 2.36 AU. With a mean diameter of 525 km, it is the third largest asteroid in the main belt according to the classification by Thomas et al. (1997). The size and composition of Vesta make it a unique subject for both planetary and terrestrial geologic research, as it provides a window into the early processes of planetary differentiation. Through examining the petrogenesis of Vesta and its constituents in the meteoritical record, a better understanding of processes that formed the early terrestrial planets can be achieved, circumventing the issue that such processes have been overprinted by subsequent tectonic activity on Earth.

2.2.1 Spectral Properties of Vesta and HEDs

Spectral data from ground-based observations (Figure 4) have suggested a relationship between 4-Vesta and the HED clan of meteorites from as early as the work by McCord et al. (1970). Both basaltic eucrites and the vestan surface exhibit spectral absorption features at wavelengths of 0.9 and 2 μm (McCord et al., 1970; Gaffey, 1976).

Recently, NASA's Dawn orbital reconnaissance mission has yielded abundant data regarding the composition of the surface of Vesta (e.g. De Sanctis et al., 2012). Interpretations of the spectral reflectivity suggest a composition that is primarily analogous to eucrites and howardites, with diogenitic compositions identified less frequently (Figure 5). McSween et al. (2013b) examined the exposed stratigraphy of the 480-km-wide Rheasilvia impact basin in the southern hemisphere of Vesta, and concluded that the crater walls display a stratigraphic sequence similar to models of vestan crust, with basaltic eucrites overlying orthopyroxenite diogenites.

2.3 Complexities in Assigning 4-Vesta as the HED Parent Body

The Vesta-HED connection is supported by a growing body of evidence for relating a suite of meteorites to its respective parent body, but the connection is not yet fully resolved.

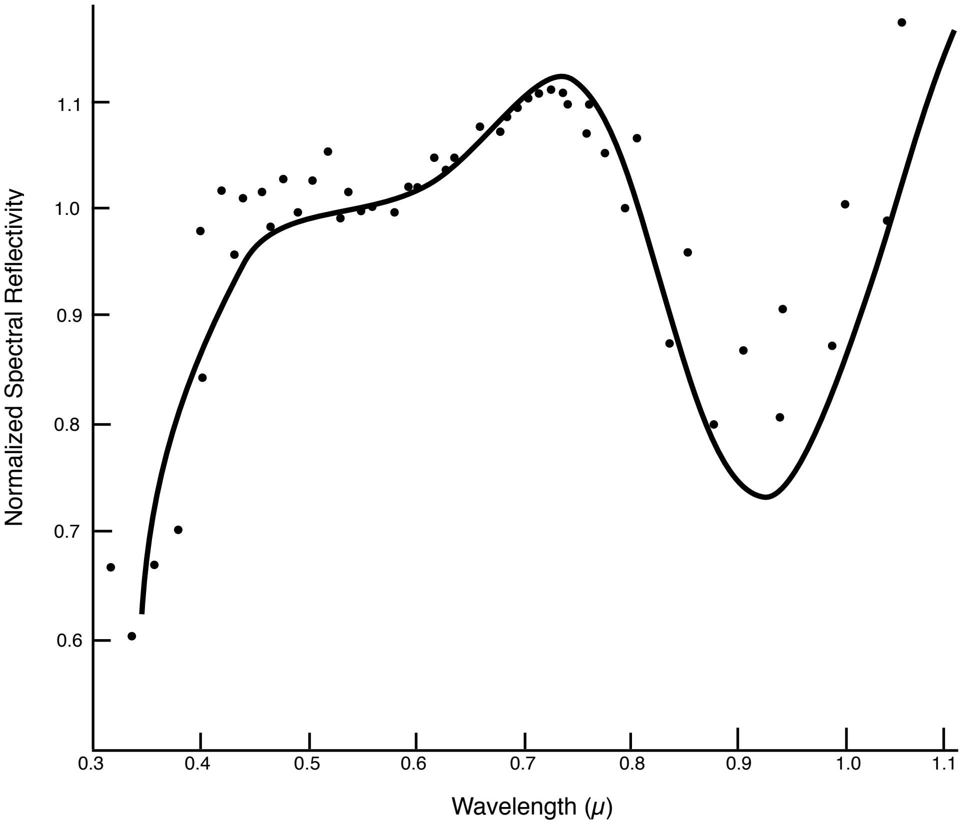

Figure 4: Spectral Absorption Features for Eucrites and 4-Vesta
Data points represent ground-based measurements of 4-Vesta's spectral reflectivity. The overlain absorption curve is for eucrites, showing a spectral correlation between Vesta and the meteorites, most notably in the ~0.92 μm wavelength, indicative of Fe^{2+} in the pyroxene M2 site. Figure after McCord et al. (1970).

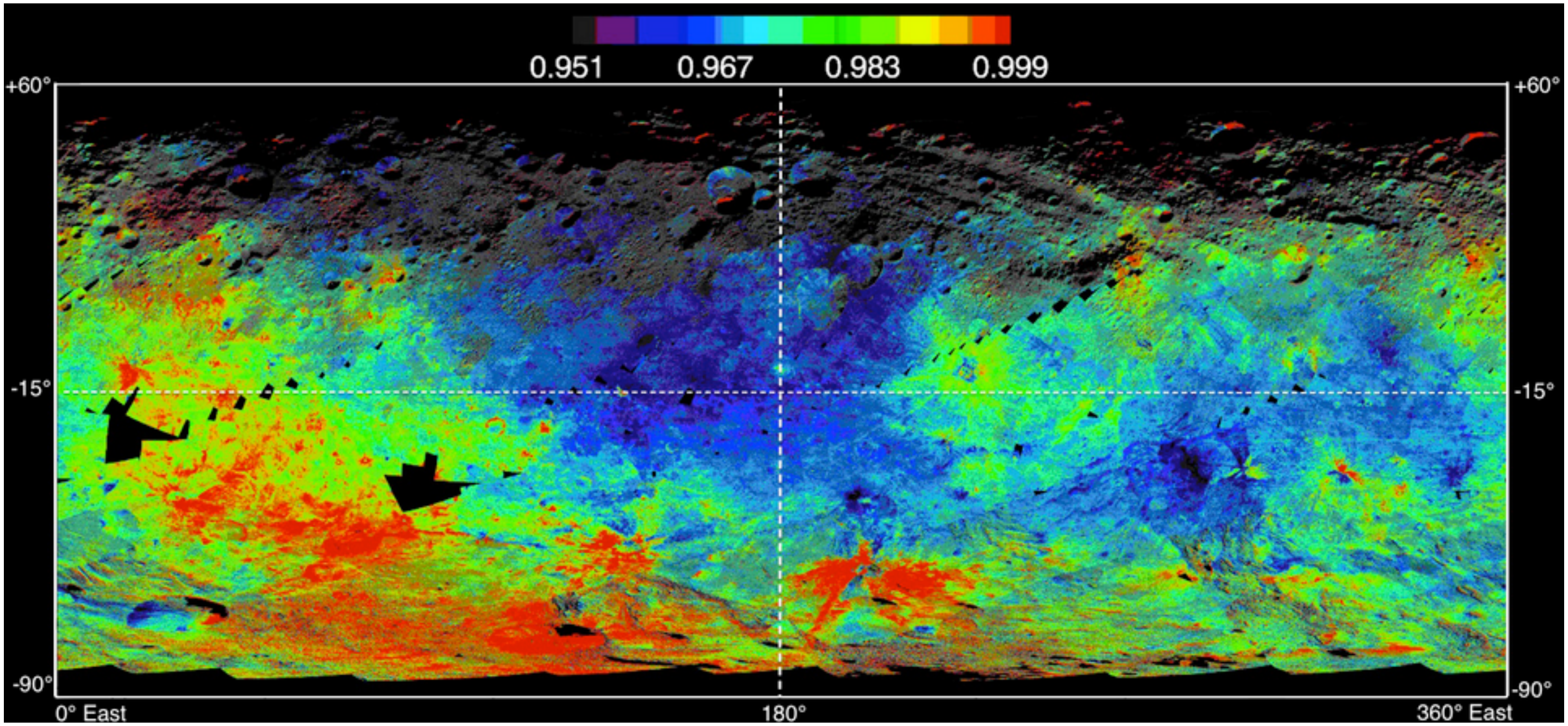

Figure 5: Compositional Surface Map of 4-Vesta
Visible and Near-infrared (VNIR) spectral data collected by NASA's Dawn Mission display HED lithologies as: blue, eucritic; green, howarditic; and red, diogenitic. From McSween et al. (2013b)

Clayton and Mayeda (1996) reported oxygen isotopic data that Wasson (2013) suggested could link HEDs to Main-group pallasites and IIIAB iron meteorites, which plot along the low ∂O^{18} end of the EFL in Figure 2 (section 2.1.1, page 5). He suggested that this would preclude the possibility that HEDs originated from 4-Vesta, because iron meteorites presumably formed at the core of their parent bodies, and could only be excavated by total disruption via impact events. Additionally, arguments against a Vesta-HED connection include orbital dynamic evidence (Wasson et al., 1979; Nesvorny et al., 2008; Parker et al., 2008) and cosmic ray exposure ages (Herzog et al., 2005; Marchi et al., 2012), which constrain the length of time that a meteorite was exposed to bombardment by the solar wind, suggesting that HEDs could plausibly be sourced from basaltic asteroids other than 4-Vesta and its dynamical relatives.

McSween et al. (2013a) stated that if HEDs are crustal material of a completely disrupted parent body from which IIIAB irons also formed, then the lack of mantle material (presumably dunitic) must be accounted for. Wasson (2013) pointed out that very few dunitic meteorites exist at all in the meteoritical record, suggesting that some mechanism must contribute to the destruction of olivine. Burbine et al. (1996) noted that dunitic asteroids would be quite brittle in comparison with basaltic asteroids and iron asteroids. This could, in part, explain the apparent lack of dunitic meteorites or asteroids. In fact, McSween et al. (2013b) reported that Dawn instruments recorded a lack of olivine-rich material in Vesta's massive Rheasilvia impact basin, despite the fact that the impact should have sampled upper-mantle material. Beck et al. (2012) suggested that olivine may have an indistinct spectral signature when orthopyroxene is in the same mineral assemblage. It is possible that this spectroscopic characteristic contributes to the absence mantle-material asteroids in the astronomical record. Taking these factors into consideration, Wasson (2013) concluded that the argument of McSween et al. (2013b) did not necessitate a vestan origin for HEDs.

Greenwood et al. (2014) refuted Wasson's (2013) $\Delta^{17}O$ association between HEDs, pallasites, and IIIAB irons by measuring $\Delta^{17}O$ for 22 diogenites. They observed a very narrow range in values for diogenites (-0.246 ± 0.018‰ relative to the TFL), and both basaltic and cumulate eucrites also show a similar $\Delta^{17}O$ range (-0.241 ± 0.016‰; Barrat et al., 2008), suggesting a homogeneity of the HED parent body magma ocean (Greenwood et al., 2005). Similarly, olivines found in thirteen Main-group pallasites yielded $\Delta^{17}O$ values within a narrow, but clearly distinct range of -0.183 ± 0.018‰ (Greenwood et al., 2006). The difference in oxygen isotopic ratios between HEDs and main-group pallasites seems to preclude the plausibility of a common parent body, as the large scale homogenization for each group would most likely not create such distinct $\Delta^{17}O$ groups according to their findings (Greenwood et al., 2005; 2014).

Currently, the majority of evidence appears to support an HED-Vesta connection, but until samples can be directly collected from 4-Vesta (which unfortunately is not considered a priority in near-future planned missions), the issue of the HED parent body cannot be fully resolved.

2.4 Stannern-group eucrites

Basaltic eucrites have historically been subdivided into three geochemical groups (Main, Nuevo Laredo, and Stannern) according to molar Mg-number ($Mg/[Mg + Fe_{total}]$) and Ti content (Figure 6; Stolper, 1977). Mg-number is used to discern the degree of differentiation, where a less extensively fractionated magma and its constituent cumulates would have more magnesian compositions (i.e. a higher Mg-number). More evolved magmas have lower Mg-numbers. Alternatively, the same degrees of differentiation can be expressed as FeO_{total}/MgO, with a greater ratio indicating a more extensively differentiated magma. Ti is an incompatible element (defined as having a bulk distribution coefficient of $D \ll 1$; Norman et al., 2005) in the plagioclase-and-pyroxene-dominated eucrite mineral assemblage. Consequently, Ti concentration can be used to indicate the degree of differentiation of a parent magma, as incompatible elements are preferentially distributed to the residual liquid during fractionation.

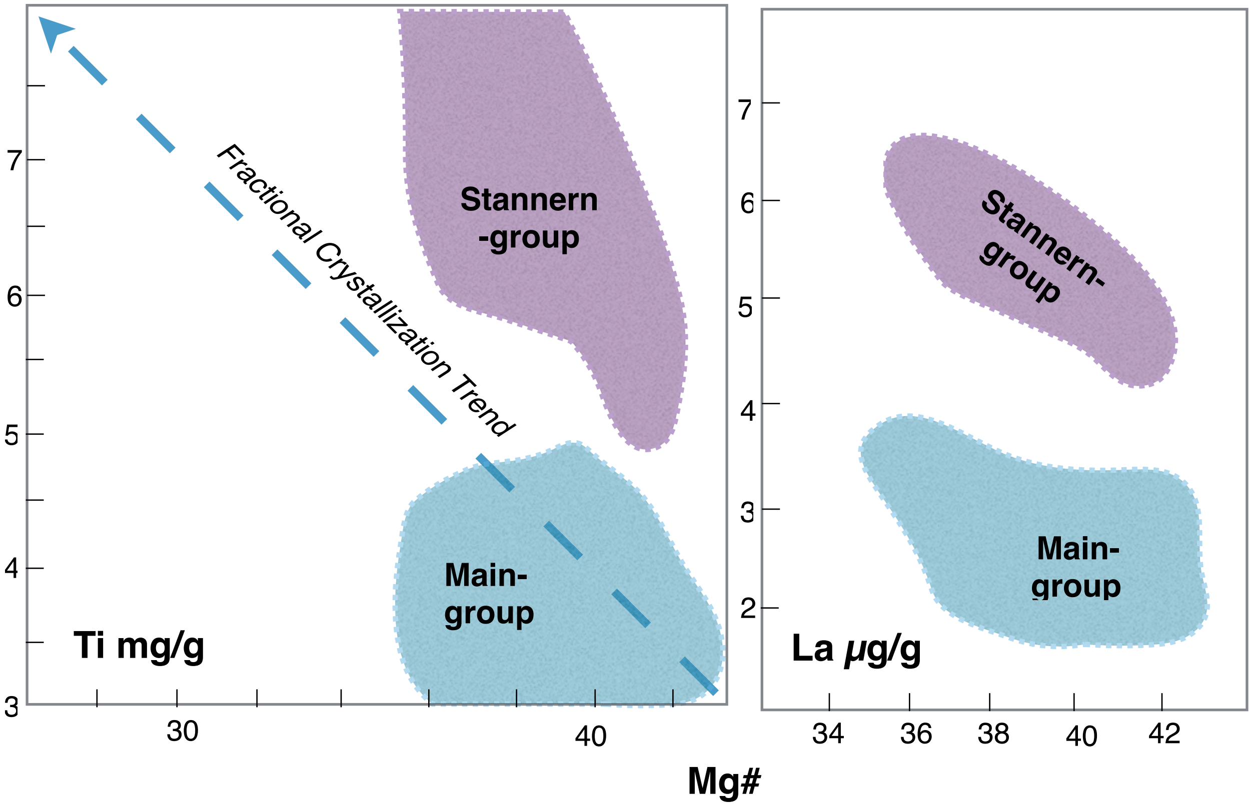

Figure 6: Eucrite Geochemical Subgroups
Eucrites are divided into geochemical subgroups according to incompatible element abundances, shown here with Ti and La. The fractional crystallization trend is drawn from Stolper (1977). Fields for Stannern and Main-group eucrites are drawn after Barrat et al. (2007) and Mittlefehldt (2015).

The Main-group comprises the majority of eucrites in the meteoritic record, with Mg-numbers of ~36-42 and Ti concentrations of ~2.3-4.9 mg/g. When plotted according to differentiation indices (e.g. Ti or Hf vs. Mg-number or Sc), Nuevo-Laredo-group eucrites fall tightly clustered near the most ferroan margins of Main-group compositions, and may be derived from the same fractionation sequences that produced the Main-group eucrites (Stolper, 1977; McSween et al., 2011). For this reason, Main-group and Nuevo Laredo group eucrites are often collectively referred to as the Main-group-Nuevo-Laredo (MG-NL) group eucrites. For the purposes of this study, we will refer to the MG-NL trend collectively as "Main-group" eucrites. Lastly, the Stannern-group eucrites, described by Stolper (1975), fall within the same range in Mg-number, but are distinguished by significantly higher concentrations of Ti and other incompatible lithophile elements (Figure 6), such as the rare-earth elements. Stannern-group eucrites also show marked negative Eu, Sr, and Be anomalies with respect to the MG-NL group, likely due to equilibration of melt material with fractionating plagioclase (Barrat et al., 2007). Although these groups were historically thought to follow related geochemical trends, recent regrouping of anomalous eucrites and the discovery of new, compositionally intermediate eucrites suggest that no clear trend exists from evolved (Ti-rich) eucrites to main-group (high Mg-number) eucrites (e.g. Mittlefehldt, 2005, 2015).

2.5 HED Petrogenesis

HED petrogenesis has been poorly constrained by most models (e.g. Stolper, 1977; Ruzicka et al., 1997; Barrat et al., 2007), as understanding the context in which these meteorites formed is limited to conclusions based on modeling of the parent body according to a very limited geochemical, geophysical, and petrographic data set. The following sections discuss the currently accepted and most historically significant models of HED petrogenesis.

2.5.1 Global Melting

HED mineralogy and petrology were integral in forming the first theories of asteroidal differentiation (Mason, 1962). These early models suggested that HEDs comprise an igneous suite that crystallized within a totally melted parent body in sequence from orthopyroxenites (diogenitic material) to eucritic material. As magnesian material fractionally crystallized from the bulk primitive magma, increasingly ferroan residual melts crystallized to form the pigeonite and plagioclase assemblage that is characteristic of basaltic eucrites. This process of differentiation would result in the formation of an iron core, dunitic mantle, and basaltic crust.

2.5.2 Partial Melting

Melting experiments carried out by Stolper (1977) suggested an alternative model of eucrite petrogenesis involving fractional crystallization from primary partial melts of bulk HED parent body composition. His study found that at specific temperatures and oxygen fugacities, a bulk eucritic liquid had could be derived from partial melting of an ordinary chondritic precursor. Low-pressure fractionation of plagioclase and pigeonite could reproduce the range of Fe abundances in eucrites: increasing degrees of crystallization would yield more evolved, ferroan residua. Incompatible lithophile trace element abundances for most eucrites could also be accounted for in this model (Consolmagno and Drake, 1977; Mittlefehldt and Lindstrom, 2003). It was inferred from these studies that basaltic eucrites would represent very early partial melts, which rose to the surface and formed a basaltic crust. Cumulate eucrites and diogenites would have subsequently crystallized from increasing degrees of low-pressure melting of the source region. Some eucrites could not be accounted for in the sequence proposed by Stolper (1977). To account for these outliers, Stolper (1977) suggested that the composition of the HED parent body was heterogeneous, and that a source region composed of olivine (Fo_{65}), pigeonite (Wo_5En_{65}), plagioclase (An_{94}), Cr-rich spinel, and metal (6-8% Ni and 0.5% Co) could yield compositions that include anomalous eucrites. The scarcity of these types of eucrites was thought to result from the difficulty in extracting low percent partial melts from their source regions while low-density phases were still present in the residue.

2.5.3 Partial Melting Models: Contradictory Evidence

If HEDs could be explained by varying degrees of partial melting of a heterogeneous parent body, then it could be assumed the oxygen isotopic ratios for eucrites would be highly variable, as multiple chondritic precursors would likely have a wide range in isotopic compositions. As mentioned in section 2.1.1, the majority of HEDs share common oxygen isotopic ratios (Δ17O = ±0.24‰), which suggests a large-scale homogenization of the source material (Greenwood et al., 2005).

Warren (1985) utilized mass-balance constraints for Al in HED parent magmas and found that the majority of HEDs were formed from residual melt fractions rather than from primary melt products. Melting experiments with CM chondrites (Jurewicz et al., 1993,1995) showed that Na-poor end members contained enough normative pyroxene for the formation of diogenites, but subsequent, lower temperature mineral constituents of cumulate and basaltic eucrites could not be reproduced.

Additionally, moderately siderophile elements (Co, Mo, and W) in basaltic eucrites do not fit calculations that involve equilibration with metal, as these elements would have been partitioned along with metals during differentiation (McSween et al., 2011; Palme and Rammensee, 1981). Instead, these elements, in addition to P and Ni, can be more adequately explained by a scenario in which both metals and silicates are completely molten (Righter and Drake, 1997).

2.5.4 Simple Magma Ocean Models

The aforementioned studies have led many authors (e.g. Ikeda and Takeda, 1985; Righter and Drake, 1997; Ruzicka et al., 1997; Mandler and Elkins-Tanton, 2013; Neumann et al., 2014) to explore evidence in the context of a magma ocean model, which would involve much more extensive melting than implied by Stolper (1977), but less than the complete global melting suggested by Mason (1962). Ikeda and Takeda (1985) pointed to the depletion of Na in basaltic eucrites as evidence of a magma ocean, as Na would be lost to space via volatile liberation nearer to the surface of Vesta. More plutonic specimens (cumulate eucrites and diogenites) showed a greater retention of Na, according to this study. Others (e.g. Righter and Drake, 1997; Ruzicka et al., 1997) have calculated trace element distributions during fractional crystallization of a magma ocean to constrain the compositional range in the eucrite suite. Ruzicka et al. (1997) inferred from their calculations that the HED parent body extensively melted and differentiated into a metallic core, dunitic mantle, and orthopyroxenite (diogenitic) lower crust. The residual liquid then crystallized in equilibrium, producing the range of most eucrite compositions. Stannern-group eucrites (enriched in incompatible elements), however, could not be accounted for in the study, as enrichment of incompatible elements decoupled from major phases cannot be produced through fractional crystallization alone (Stolper, 1977; Ruzicka et al., 1997). Righter and Drake (1997) came to similar conclusions by calculating trace element distributions among HEDs, but suggested an alternate sequence of differentiation, in which harzburgite and orthopyroxene crystallized in equilibrium after metal segregation. The residual liquid then crystallized in equilibrium, accounting for the range of most eucrites. The enrichment in incompatible trace elements in the Stannern-group could not be explained in this model either, and that group was assumed to represent residua from another source region.

2.5.5 Simple Magma Ocean Models, Maybe too Simple

Diogenites range in incompatible element content, which may result from significant variation in the degree of fractional crystallization, but the restricted Mg-number seems to suggest otherwise (Mittlefehldt, 1994). Shearer et al. (1997) suggested that diogenites could have accumulated from low percent (10-20%) fractional crystallization of parental basaltic magmas, but only if those magmas were compositionally distinct from one another, which would necessitate either the equilibrium melting of heterogeneous sources or the fractional melting of a homogeneous source. Neither of these scenarios are compatible with a magma ocean model. Barrat et al. (2008) examined the trace element abundances of 18 diogenites, and found significant diversity in REE patterns among the specimens (Figure 7). In their interpretation, the diversity in diogenites implies a diversity of parental melts, in contrast to a scenario involving a single magma ocean. Additionally, the wide range in estimated Fe/Mn ratios in parental melts (1.4–3.5), which overlaps values that are found in cumulate eucrites, would preclude the possibility of diogenitic material crystallizing from melts more primitive than those of eucrites. The variations in HREE abundances may also be produced from the remelting of cumulates

(Barrat et al., 2008). The melt fraction derived from cumulates would then be brought to the surface via diapirs, due to the contrast in density with an overlying basaltic shell (Barrat et al., 2008).

Yamaguchi et al. (2011) examined the petrology of thirteen diogenites and classified them as either equilibrated or unequilibrated, suggesting either a high or low grade of metamorphism. In unequilibrated diogenites, orthopyroxene crystals exhibit chemical zonation, which is indicative of rapid cooling from a melt with little to no subsequent exposure to the crustal metamorphism experienced by many eucrites. The lack of post-crystallization alteration casts some doubt on the idea that all diogenites are products of crystallization from a global magma ocean (e.g. Righter and Drake, 1997), and suggests that at least some diogenites are products of later stages of magmatism on Vesta (Yamaguchi et al., 2011). The geochemical and petrologic characteristics of HEDs found in these studies imply a geologic history of Vesta that is more complicated than proposed by models discussed above.

2.5.6 A More Robust Magma Ocean Model

Some of the variations among diogenitic incompatible element contents that contradict simple magma ocean models have been accounted for by Mandler and Elkins-Tanton (2013). Their model includes an early stage of equilibrium fractionation similar to Righter and Drake (1997), but then envisions a scenario involving polybaric fractionation and magma recharge within plutons located in the basaltic crust. Following ~60-70% equilibrium fractionation,

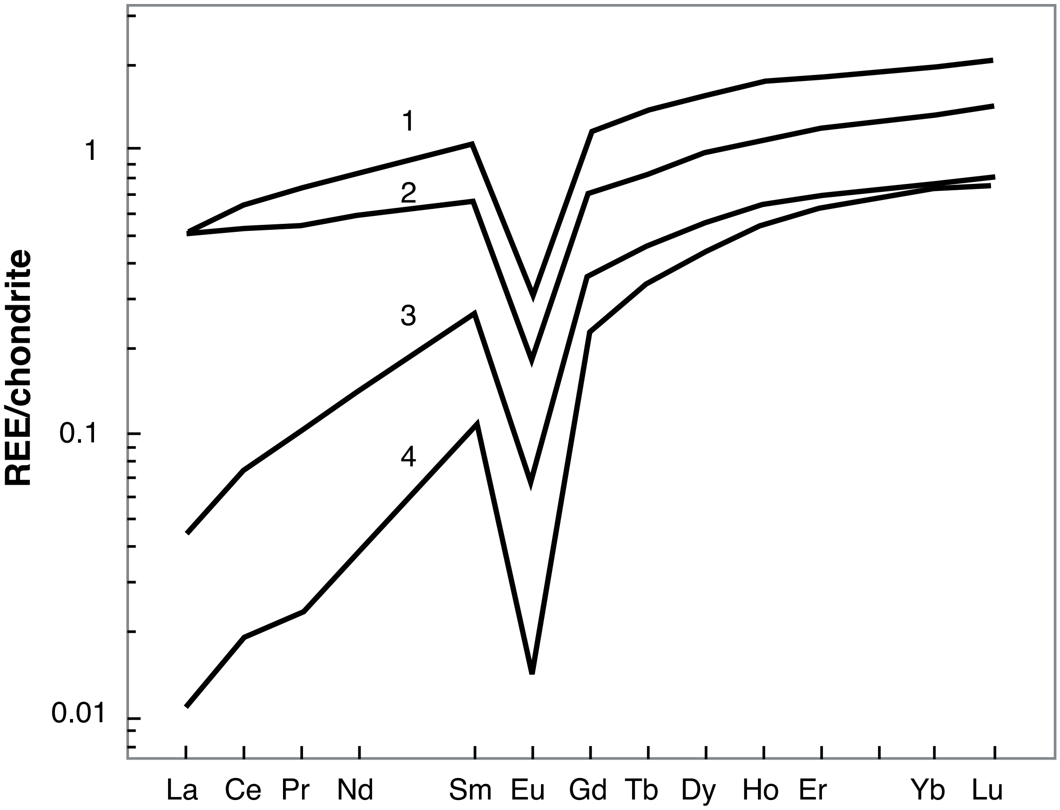

Figure 7: REE Abundances in Diogenites
Variations in REE abundances among diogenites appear to contradict simple, global magma ocean models, as crystallization within a global magma ocean would presumably produce homogeneous diogenites. (1) NWA 4272, (2) Johnstown, (3) Bilanga, and (4) Dhofar 700 residue. Adapted from Barrat et al. (2008). REEs are normalized to chondritic values to aid in the interpretation of geochemical trends.

convective lock-up of the magma ocean would cause the residual liquid to ascend, and gradually replace the original, presumably chondritic, crust with a basaltic one via burial and melting. Further melt residua would infiltrate the basaltic crust, forming plutons in which cumulate diogenites and eucrites could form. As the plutons crystallized, magma recharge from the residual ocean could account for the range in incompatible element concentrations contrasting with relatively consistent Mg#.

Not all incompatible trace element concentrations in diogenites can be explained by the model of Mandler and Elkins-Tanton (2013). The wide range in Dy/Yb ratios (and other HREEs) for diogenites cannot be reproduced in this scenario, as the assimilation magma from the underlying magma ocean would not significantly increase HREE concentrations to the levels seen in diogenites (Barrat and Yamaguchi, 2014). Mandler and Elkins-Tanton (2013) also fail to distinguish between the Main-group eucrites and the Stannern-group, providing no explanation for the anomalous incompatible element concentrations seen in these basaltic eucrites, though their model does provide plutons in which Stannern-group eucrites may form (section 2.5.7, page 23).

In a similar model, Neumann et al. (2014) also attempted to constrain the inconsistencies in HED petrogenesis by examining the effects of radioisotopic heat distribution within the HED parent body (Figure 8). According to a number of geochronological studies (e.g. Ghosh and McSween, 1998; Gupta and Sahijpal, 2010), the assumption can be made that accretion ceased on Vesta within three million years of the formation of CAIs, the first solid matter that formed in the solar system. Neumann et al. (2014) suggested that the origin of eucrites could be more narrowly constrained by considering the heat generated by short-lived radionuclides during formation, such as ^{26}Al and ^{60}Fe, and the efficiency with which that heat was partitioned from the interior. Their model suggested that a global magma ocean could only form if ^{26}Al was transported toward the surface early in the history of the HED parent body.

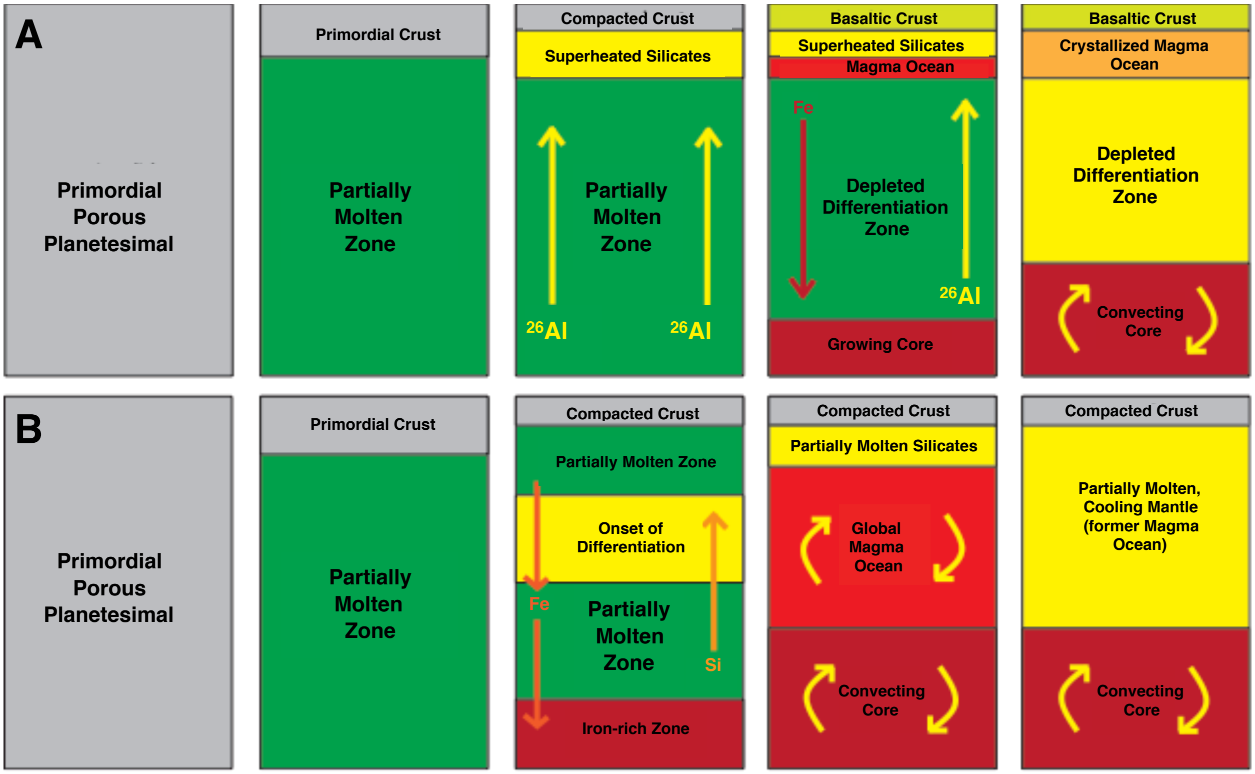

Figure 8: Neumann et al. (2014) Magma Ocean Model
The evolutionary sequences of the HED parent body are presented here in two potential scenarios: (A) The top row sequence is generated in geophysical models (Neumann et al. 2014) as a result of the partitioning of live ^{26}Al into the first low percent partial melts, which buoyantly ascend to the surface. (B) The bottom row represents the formation of a more massive global magma ocean (e.g. Ruzicka et al., 1997; Righter and Drake, 1997), in which partitioning of active ^{26}Al is not accounted for. Adapted from Neumann et al. (2014).

Otherwise, eucrites and diogenites must have formed from partial melts of the interior. Neumann et al. (2014) concluded that the partitioning of ^{26}Al would likely have resulted in the formation of a thin, sub-surface magma ocean (Figure 8, top row). Melt from the magma ocean permeated the overlying superheated silicate layer, due to a contrast in density (Neumann et al., 2014). This would place the magma ocean more closely beneath the basaltic crust, where the magma then crystallized to form cumulate eucrites and diogenites. At this point, the bulk mantle was depleted in the least refractory elements, but continued to differentiate material. The sequence of crystallization for basaltic eucrites, cumulate eucrites, and diogenites is supported by ^{26}Al-^{26}Mg isochrons for HEDs, which imply that basaltic eucrites are older than both cumulate eucrites and diogenites (Hublet et al., 2013). In the final phase of this model, the magma ocean crystallized, but the metallic core continued to convect, providing a mechanism for evident magnetism preserved in some eucrites during the late stages of HED parent body formation (e.g. Fu et al., 2012).

Magma ocean models provide the rapid, successive basaltic eruptions employed in some models of eucrite metamorphism (Yamaguchi et al., 1997). Thermally metamorphosed eucrites were first explained as impact products (Nyquist et al., 1986), but the ubiquity of metamorphosed eucrites and corresponding clasts in howardites (e. g. Fredrikkson and Keil, 1963) cast doubt on an impact origin. Yamaguchi et al. (1997) found the large number of metamorphosed eucrites to imply a global metamorphic event, and developed a model of thermal metamorphism driven by rapid, successive burial of basaltic flows. In the model, eruption rates were very high in the early history of the HED parent body (presumed to be Vesta in the study). The oldest lava flows were consequently exposed to the most heat from the mantle, thermally metamorphosing and annealing them, possibly to the extent of partial melting (Yamaguchi et al., 2013). This process culminated in a geothermal gradient that accounts for the full range of eucrite metamorphism, with the highest degree of metamorphism occurring in the oldest rocks at the bottom, and the unequilibrated rocks being the youngest near the surface.

2.5.7 Stannern-group Eucrites as Partial Melt Contaminants

Barrat et al. (2007) proposed that Stannern-group eucrites resulted from the contamination of MG-NL eucritic magmas by crustal partial melts (Figure 9). They pointed out that if the petrogenetic sequences in Stolper (1977) were correct, then one could make the assumption that Stannern-group eucrites would be among the first eucritic magmas produced, because they result from smaller degrees of partial melting. However, petrologic evidence contradicts this assumption, as Stannern-group eucrites exhibit significantly less thermal metamorphism than MG-NL group eucrites (Barrat et al., 2007). Thermal metamorphism can be used as an indicator of relative age in eucrites, as most current models suggest that eucritic lavas erupted on the surface of 4-Vesta sequentially buried older eucritic basalts, exposing them to increasing degrees of thermal metamorphism (Yamaguchi et al., 1997). The residual magma ocean envisioned in some models (e.g. Mandler and Elkins-Tanton, 2013; Neumann et al., 2014) would supplied additional heat to the largely nonporous, superheated silicate layer (Neumann et al., 2014; Mandler and Elkins-Tanton, 2013). Heat from these layers thermally metamorphosed the overlying eucritic crust and may have heated some regions to the point of partial melting (Barrat et al., 2007; Yamaguchi et al., 2009; Yamaguchi et al., 2013). Low-percent melt fractions produced are enriched in incompatible elements (Yamaguchi et al., 2013), as they are preferentially distributed into the least refractory components, or mesostasis minerals, which are the lowest temperature phases. In eucrites, mesostasis minerals can include fayalite, tridymite, apatite, and merrillite (e.g. Duke and Silver, 1967; Hsu and Crozaz, 1996). As magma buoyantly ascended from the residual ocean through regions where partial melting occurred, it may have assimilated crustal partial melts, producing magma mixtures similar in composition to that of the Stannern-group eucrites, which then quickly crystallized as they ascended to the surface or cool in large-scale dikes and sills. (Barrat et al., 2007). Logically, this would place Stannern-group eucrites later in the petrogenesis of the vestan surface than suggested by Stolper (1977).

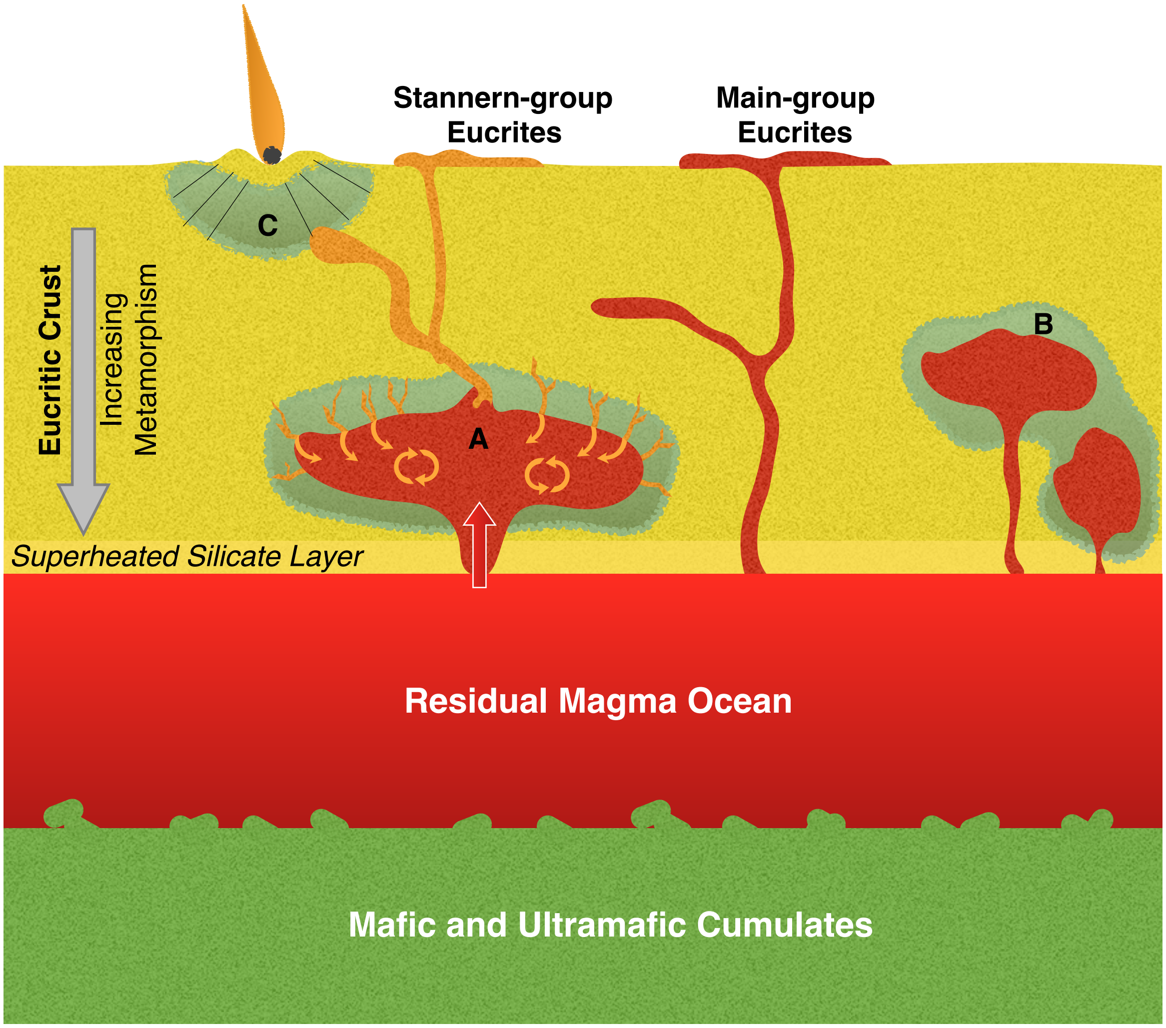

Figure 9: Stannern-group Eucrite AFC Petrogenesis
This model of Stannern-group eucrite petrogenesis (not to scale) incorporates assimilation-fractional-crystallization (AFC) processes to explain incompatible trace element enrichments in the Stannern group. (A) provides the scenario in which assimilation of crustal partial melts could have occurred (see text), fueled by magma recharge from the residual magma ocean. (B) shows contact metamorphism caused by the release of thermal energy from plutons. (C) is shock metamorphism due to impact. Drawn after Barrat et al. (2007), incorporating additional elements from models by Neumann et al. (2014) and Mandler and Elkins-Tanton (2013).

Though the Barrat et al. (2007) model offers a plausible explanation for the formation of Stannern group eucrites, the model has yet to be experimentally verified. Yamaguchi et al. (2013) performed melting experiments with HaH 262, an unbrecciated basaltic eucrite, which showed that heating of otherwise unaltered, mesostasis-rich eucrites would mobilize partial melts within 24 hours. The highest temperature reached in the experiment was 1100°C, which yielded chemically homogeneous melt pockets and veins of melts between relict pyroxene and plagioclase. The melts produced were enriched in Ti and REEs, largely derived from melting of mesostasis minerals. These experiments yielded melts that showed some of the compositional aberrations seen in Stannern-group eucrites in terms of incompatible trace element enrichment. Metamorphosed eucrites show what could be interpreted as a corresponding trend in REE depletion (Yamaguchi, et al., 2009). However, conclusively explaining these meteorites as residues of Stannern-group eucritic compositions is problematic, as the chemical composition of the residual lithology, resulting from the formation of Stannern-group eucrites, is difficult to model from existing experimental data (Yamaguchi et al., 2009, 2013). Granoblastic textures like those seen in highly metamorphosed eucrites have been reproduced in 100-hour experiments with San Carlos olivines (Whattam et al., 2008), but it is unlikely that such textures could be reproduced in eucrites without also volatilizing the accessory carrier phases of incompatible elements (apatite and and merrillite [Hsu and Crozaz, 1996]), which would render the data useless in terms of testing the Barrat et al. (2007) model. Partial melting in the model also only includes the major minerals, pyroxene and plagioclase, yet in-depth petrographic and geochemical analyses have shown that the most important carriers for REEs and other incompatible elements are among mesostasis phases, specifically apatite (e.g. Yamaguchi et al., 2013; Hsu and Crozaz, 1996). This illustrates the fact that petrogenetic models involve the most ideal conditions, simplified in order to make calculations manageable and predictable.

Further experimental analyses are required to assess implications of the Barrat et al. (2007) model and place further constraints on petrogenetic processes that occurred on the HED parent body. Partial melt fractions in the lowest temperatures in the experiments of Yamaguchi et al. (2013) were too small to be analyzed (F = 0.01-0.02), but increasing temperature should result in a greater melt fraction. Compositional analyses of those melt products can be used to calculate resultant magma mixtures as modeled in Barrat et al. (2007).

We have acquired a suitable meteorite in order to perform melting experiments similar to those in Yamaguchi et al. (2013). After performing these experiments at conditions that reflect the environment in which magma mixing occurred (according to the model in question), we measured the compositions of the experimental melt fractions, utilized them in calculations for magma mixing, and compared our results to those modeled in Barrat et al. (2007) in order to assess its validity.

3.0 Methods

3.1 Sample Acquisition

In order to accurately replicate eucrite petrogenesis, the starting material should be an unbrecciated, unequilibrated, Main-group eucrite that is rich in mesostasis minerals. These characteristics are representative of the liquid from which the majority of MG-NL eucrites fractionated (Stolper, 1977). Preferably, the material should also be fine grained to maximize surface area for melting to occur, producing melts that would be more representative of the bulk composition, as shown in Stolper (1977). These criteria were particularly difficult to meet in the present study, as many of the available unbrecciated, unequilibrated eucrites were considered too valuable for destructive experimentation, or were held by collectors who were reluctant to fragment pristine masses. Many of the available Antarctic samples were too small for experimentation, and other samples that may have been well-suited for experimentation would not be available in time for this study to be conducted, due to the timing of the Meteorite Working Group, which assigns Antarctic meteorites to research groups on a bi-annual basis. After several months of searching, the Monnig Meteorite Collection at Texas Christian University purchased the main mass (510 g) of NWA 8562 (Figure 10) in June 2015. The meteorite is an unbrecciated, unequilibrated eucrite. The sample is a find, rather than an observed fall, but its interior is still unaltered by terrestrial contamination, making it ideal for experimentation. We have also determined the geochemical subgroup classification of NWA 8562, and the results are presented in this study.

Figure 10: NWA 8562 Main Mass
The main mass of the eucrite NWA 8562 prior to cutting for analytical samples.

3.2 Experimental Techniques

3.2.1 Establishing Experimental Parameters

In order to accurately replicate eucrite petrogenetic processes, the experiments must be conducted and controlled at specific temperatures, oxygen fugacities, and pressures that reflect conditions of their source lithologies on the HED parent body. Stolper (1997) conducted multiple low-pressure melting experiments (Figure 11) on eucites, and found that at metal-saturated conditions, pigeonite, plagioclase, ± olivine, spinel, and metal can crystallize from Main-group eucritic magma compositions. The simultaneous crystallization of pyroxene, plagioclase, and

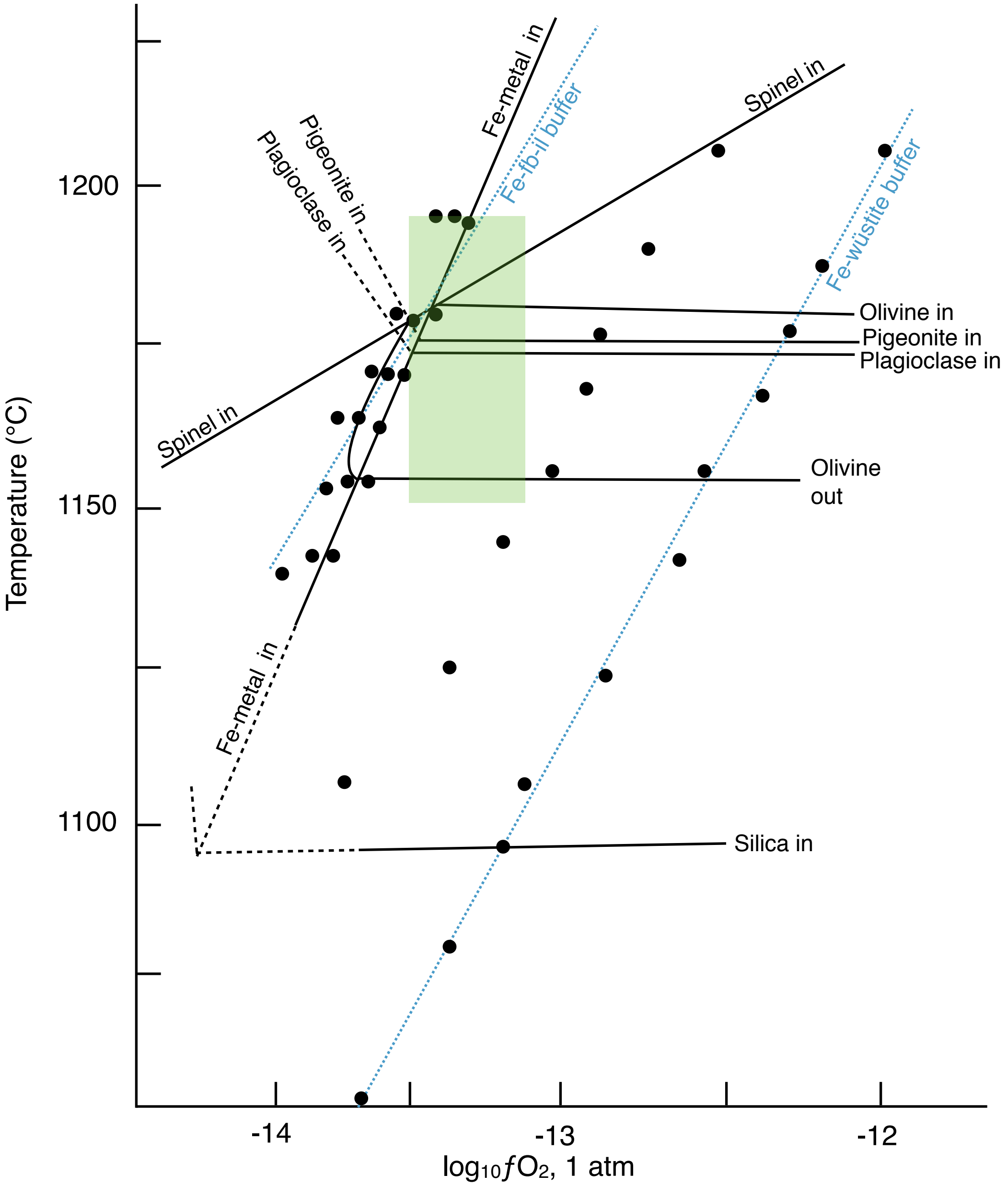

Figure 11: P-$f O_2$-T Constraints from Eucrite Melting Experiments
Low-pressure melting experiments with the Main-group basaltic eucrite, Juvinas, at variable $f O_2$ and T. Stolper (1977) found that eucrite major mineral assemblages could be reproduced when crystallization occurred from 1150-1190°C and $f O_2 = 10^{-13.2 \pm 0.2}$ (added by this study as the green field). This places the field for eucrite petrogenesis at about one log unit below the iron-wüstite buffer (hence, $\log f O_2 =$ IW-1). Solid lines indicate the presence or absence of a phase in the experimental melt product, dashed lines represent inferred presence of a phase where not all melt had fully crystallized before quenching, blue dotted lines are oxygen buffers, and solid black points are experimental conditions. The Fe-fb-il line represents the iron-ferrobrookite-ilmenite buffer. Adapted from Stolper (1977).

possibly olivine can account for the majority of eucrites through pyroxene-plagioclase fractionation at a pressure of 1 atm, as predicted by petrographic analyses (Mason, 1962; Duke and Silver, 1967). Simultaneous crystallization of three or more minerals suggests igneous quenching of a liquid in equilibrium with liquidus phases at low pressure (e.g. Duke and Silver, 1967)). Additionally, Mason (1962) and Duke and Silver (1967) found no evidence of high-pressure igneous processes. Greater pressures in the system would likely increase temperatures for the appearance of pyroxene and olivine, removing them from the metal-saturated liquidus (O'Hara, 1968; Merrill and Williams, 1975). A temperature range of 1150-1190°C can be defined for the onset of crystallization in the experiments by Stolper (1977), because the temperature of crystallization for olivine, pigeonite, and plagioclase did not vary greatly with variable oxygen fugacity (fO_2) between the Fe-fb-il and Fe-wüstite buffers (Figure 11). When oxygen fugacity was increased above metal saturation, the temperature for spinel crystallization rose dramatically, possibly due to increased Cr^{3+}/Cr^{2+} above IW-1. Fugacities below metal saturation resulted in significantly more precipitation of Fe metal at the expense of FeO, and consequently increased the crystallization temperatures for pigeonite and pyroxene, while lowering the temperatures of spinel and olivine. Together, these constraints place redox conditions of eucrite formation at $\log_{10}fO_2 = -13.3$, which is one log unit below the iron-wüstite buffer, IW-1 (Figure 11; Stolper, 1977).

3.2.2 Melting Experiments

Following constraints from Stolper (1977) and methods by Yamaguchi et al. (2013), low-pressure, 1 atm, 24-hour melting experiments were conducted on fragments of NWA 8562 at 1050, 1100, 1150, and 1200°C in a Deltech-DT-31-VTHN-C 1 atm gas mixing furnace at the Smithsonian Institution's National Museum of Natural History (N.M.N.H.) in Washington, D.C.. The fragments were selected from the most pristine, unaltered areas available in the main mass, and were free from fusion crust. fO_2 was controlled by a mixture of CO-CO_2, and measured using a thermocouple attached to a Pt-Rd wire that ran from inside the furnace and through a tube of standardized oxygen fugacity. The difference in oxidation potential between the two environments generates an electromotive force along the wire that can then be used to calculate the oxygen fugacity inside of the furnace. Due to limitations of the equipment used, the lowest achievable oxygen fugacity for the experiments was log fO_2= IW-0.5. Although this is slightly above the inferred oxygen fugacity for eucrites, it should not make for an appreciable difference in the melting temperatures of most of the relevant mineral phases, which show little variation between metal saturation (Fe-fb-il buffer) and the Fe-wüstite buffer (Stolper, 1977). The melting temperature of spinel may prove more problematic for our experiments, as it has been shown to increase with fO_2 above metal saturation (Stolper, 1977), but this was not observed (see section 4.2.1, pages 43-52). In order of increasing experimental temperatures, each of the four fragments weighed 441, 352, 386, and 316 mg, and were placed in an alumina crucible that was suspended inside the furnace by a Pt wire. At the end of each experimental run, a powerful electrical current was passed through the Pt wire, rupturing it and drop-quenching the crucible and its contents into water. The samples were then mounted in epoxy, cut, and polished for analyses by Dr. Nicole Lunning at the Mineral Sciences Department of the Smithsonian Institution’s N.M.N.H. in Washington, D.C.

3.3 Analytical Techniques

3.3.1 Petrographic Characterization

Two 1-inch round thin sections of NWA 8562 were prepared by Dr. David Mann at High Mesa Petrographics. Petrographic analysis was conducted via optical microscopy with an Olympus BX51 polarizing light microscope at the Oscar Monnig Meteorite Collection at Texas Christian University. Modal analysis was performed manually using a point-counting method, with ~500 points examined per sample (Appendix II), quantifying mineral abundance and melt percentage.

3.3.2 Oxygen Isotopic Composition

Two grams of NWA 8562 were sent to the Oxygen Isotope Laboratory in the Department of Physical Sciences at the Open University, where Drs. Richard Greenwood and Ian Franchi powdered and analyzed the samples in duplicate. Bulk oxygen isotope composition was analyzed with a Thermo Scientific MAT 253 gas source mass spectrometer, equipped with a CO_2 laser to assist in fluorination. The sample was heated in the presence of BrF_5 in order to liberate oxygen, which was then further decontaminated by two cryogenic nitrogen traps and a bed of KBr. Oxygen was then passed through the spectrometer, which separated and quantified the three constituent isotopes. Modifications were made to improve the accuracy of procedures outlined by Miller et al. (1999), as explained in (Greenwood et al., 2015).

3.3.3 Major Element Geochemistry

The two unheated 1-inch round thin sections of NWA 8562 and the four experimental charges were taken to the Smithsonian Institution's Department of Mineral Sciences in the National Museum of Natural History and analyzed with the FEI Nova NanoSEM 600 scanning electron microscope (SEM). Backscatter electron (BSE) maps were generated for each thin section, and an in-built ThermoFisher energy dispersive x-ray spectrometer (EDS) was used to generate high-resolution elemental maps of the two thin sections to facilitate subsequent quantitative major phase analysis. Tiles were produced for each element examined, with the pixel value corresponding to the relative concentration of an element at each point, and were joined together as a mosaic and layered in Adobe Photoshop. Merging values of particular elemental layers rendered qualitative mineralogic maps (Appendix I) of the thin sections, which were useful when prospecting for analytical points. EDS was also used to determine the distribution of major elements in the melt products of the experimental charges. Originally, the elemental maps were also intended to be used in an automated method of modal analysis, but irregular calibration of pixel values in each tile for several key elements rendered this method ineffective (Appendix I).

All major element data were measured by a Cameca SX-100 electron microprobe analyzer (EMPA) at Oklahoma University's Electron Microprobe Laboratory with the assistance of Dr. George Morgan. Operating conditions were a 40° takeoff angle, 20 keV beam energy, and 2 nA beam current. Beam size for all samples was 20 μm, apart from melts in the 1050°C run, which were analyzed with a beam size of 5 μm, because most of the melt fractions were <20 μm in diameter. This narrow beam size may have resulted in some loss of Na due to volatization, but other relevant major elements should have been unaffected (personal correspondance, Dr. George Morgan, Oklahoma University). Samples were analyzed in separate compositional runs, individually examining silicates (pyroxenes, plagioclase, and silica polymorphs), oxides/sulfides (chromite, ilmenite, and spinels), and glass (melt products in experimental charges) in order to maintain a high degree of accuracy. Bulk composition of NWA 8562 was calculated by averaging the major oxide compositions of analytical points for the 1200°C experimental charge, which was nearly completely melted and homogeneous. Molar abundances of elements were calculated using a basis of 6 oxygen atoms in pyroxene, 8 in plagioclase, and 4 in olivine.

3.3.4 Trace Element Geochemistry

Bulk trace element composition of NWA 8562 was conducted at the GeoAnalytical Laboratory at Washington State University via a Finnigan Element2 high resolution single collector inductively coupled plasma mass spectrometer (HR-ICP-MS). The ~3 g sample was powdered with an agate mortar and pestle and dissolved in a solution of HF.

Trace element data for individual mineral crystals in all samples and melt products were collected using an ESI UP193FX ArF excimer laser coupled to a Thermo Element XR high-resolution inductively coupled mass spectrometer (LA-ICP-MS) at the Plasma Analytical Facility of the National High Magnetic Field Laboratory at Florida State University by Shuying Yang and

Dr. Munir Humayan. Spot sizes of the analyses were 25-50 μm for silicates (i.e. pyroxene and plagioclase) in both heated and unheated samples, and 75 μm for a rastered analysis of the bulk composition of the starting material. Unfortunately, the melt pockets in the 1050°C run were too small to be analyzed, and minor phases (i.e. olivine, oxides, and sulfides) could not be distinguished in reflected light during analysis.

3.3.5 Calculating Binary Magma Mixtures

Barrat et al. (2007) utilized simple binary mixing equations (DePaolo, 1981) to model the assimilation of melt material into a main-group magma:

when D<<1,

$$\frac{C_m}{C_m^o} = 1 + \frac{M_a C_a}{M_m C_m^o} \quad , \qquad [3]$$

when D≥1,

$$\frac{C_m}{C_m^o} = \frac{C_a}{D C_m^o}\left[1 - e^{\frac{-DM_a}{M_m}}\right] + e^{\frac{-DM_a}{M_m}} \quad , \qquad [4]$$

where C_m= concentration of an element in the resultant magma mixture, C°_m= concentration of an element in the original magma, D= bulk distribution coefficient, C_a= concentration of an element in the assimilated component, M_a= mass of the assimilated component, and M_m= mass of original magma. Simple binary mixing equations were used, because assimilation-fractional-crystallization (AFC) equations (DePaolo, 1981) only yielded Stannern-group enrichment of incompatible elements when the ratio of the rate of assimilation to the rate of fractionation was greater than 5, yielding values similar to simple binary mixing (Barrat et al., 2007).

4.0 Results

4.1 Starting Material

4.1.1 Petrographic Characterization

Modal analysis of NWA 8562 provides a mineral assemblage of 45 wt% pyroxene, 40 wt % plagioclase, 10 wt% silica, and 3 wt% olivine, with accessory troilite, chromite, and spinel. Pyroxene and plagioclase define subophitic texture (Figure 12). Pyroxene crystals, which range from < 1 μm to 1.18 mm in diameter, exhibit mosaic texture, a shock-induced feature in which larger crystals fracture into a myriad of smaller constituents in response to impact (e.g. Krot et al., 2014). Crystals of plagioclase range from several microns to phenocrysts that measure ~2.2 mm in diameter, and have ubiquitous inclusions of troilite (generally < 1 μm in diameter). Plagioclase is not maskelynitized, which places an upper limit on the degree of shock experienced by the minerals during impact (Krot et al., 2014). Mesostasis minerals (i.e. silica, olivine, oxides, and sulfides) are difficult to identify using polarizing light microscopy, due to their small crystal sizes (generally < 100 μm) and the mosaic nature of neighboring pyroxene. However, correlating this method with BSE images shows that mesostasis minerals occur along pyroxene-plagioclase crystal boundaries, with silica laths (< 1 to ~100 μm) penetrating into the crystal lattices of both constituents. Olivine (usually <100 μm) often occurs with chromite, ilmenite, troilite, spinel, and silica. Chromite forms the largest oxides (up to 200 μm), but tends to be less abundant than ilmenite and spinel, which are smaller (<5 and 50 μm, respectively), and often occur as inclusions in chromite. Additional maps (PPL, XPL, and BSE) of unheated NWA 8562 can be found in Appendix I.

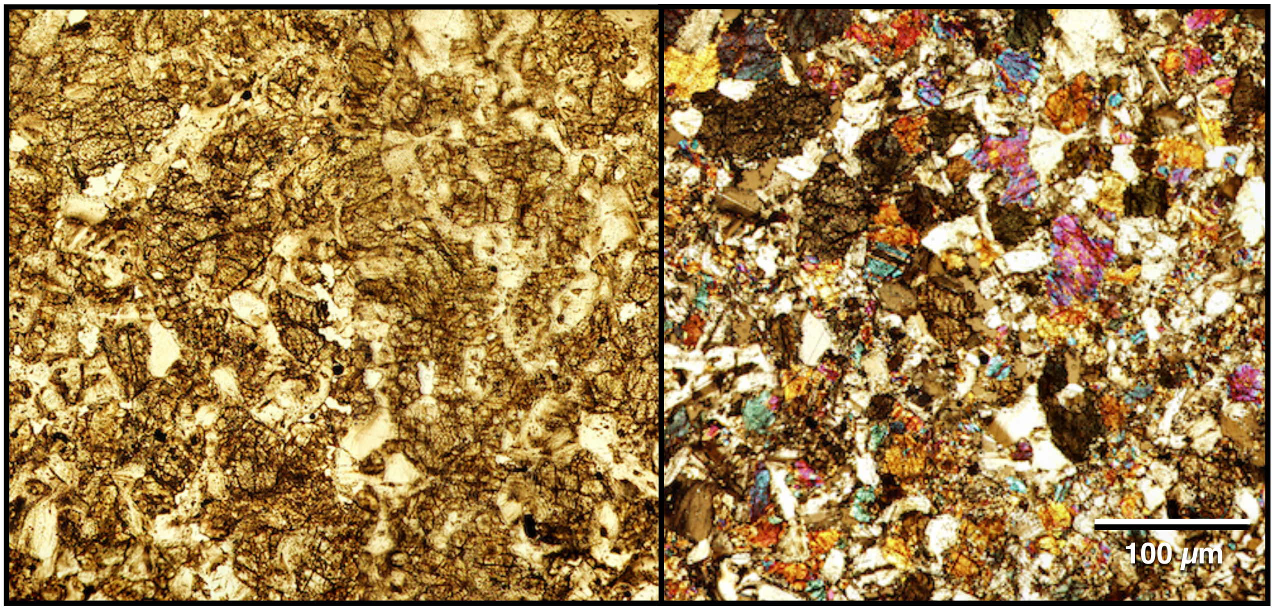

Figure 12: Photomicrographs of Unheated NWA 8562 Thin Sections
(A) and (B) show thin sections of unheated NWA 8562 in both plane-polarized (ppl) and cross-polarized (xpl) light. Crystals with high birefringence are pyroxene, and those with low birefringence are plagioclase. Whole thin section photomicrographs can be found in Appendix I.

4.1.2 Oxygen Isotope Composition

The results obtained for the oxygen isotopic composition on NWA 8562 are as follows (1σ):

$\delta^{17}O = 1.768 \pm 0.042‰$, $\delta^{18}O = 3.842 \pm 0.072‰$,

$\Delta\ ^{17}O = -0.246 \pm 0.004‰$ (linearized, slope: 0.5247)

The $\Delta^{17}O$ value of the sample plots close to and within error of the HED fractionation line of Greenwood et al. (2006) (Figure 2, section 2.1.1, page 5), and indicates that NWA 8562 is an isotopically normal member of the HED clan.

4.1.3 Major Element Geochemistry

The bulk major element composition for NWA 8562 is presented in Table 1. Additional major element data are presented in Appendix III. Pyroxene compositions range from pigeonite (endmember: ~$En_{52}Wo_{8}Fs_{40}$) to ferro-augite (endmember: ~$En_{15}Wo_{33}Fs_{52}$) [Figure 13]. Minor

Table 1: Major Oxides for Silicate Phases and Bulk Unheated NWA 8562.

Unheated NWA 8562 Phases, Average Wt %

Major Oxides	Plagioclase n=53	2σ	Pyroxene n=127	2σ	Olivine n=47	2σ	Bulk[1]
SiO_2	43.08	0.27	48.34	1.28	30.14	0.29	39.40
TiO_2	0.19	0.01	0.59	0.32	0.15	0.04	0.34
P_2O_5	0.04	0.01	0.02	0.02	0.08	0.07	0.03
Al_2O_3	20.24	0.39	1.32	0.32	0.03	0.01	8.68
Cr_2O_3	0.11	0.01	0.41	0.09	0.03	0.01	0.22
FeO	19.09	0.11	29.25	2.08	62.04	0.62	22.50
MnO	0.51	0.01	0.94	0.04	1.43	0.03	0.66
MgO	4.29	0.01	12.58	3.97	6.1	0.57	7.40
NiO[2]	bdl	0.01	bdl	0.01	bdl	0.01	0.00
CaO	12.22	0.10	7.26	3.20	0.68	0.05	8.07
Na_2O	0.57	0.04	bdl	0.01	bdl	0.00	0.23
K_2O	0.04	0.01	0.01	0.01	0.00	0.00	0.02
Total	100.37		100.73		100.69		87.55[3]
	Plagioclase		Pyroxene			Olivine	
%An	90.52		%En	36.04		%Fo	13.67
%Ab	9.11		%Fs	47.80		%Fa	86.33
%Or	0.36		%Wo	16.16			
			Fe/Mn	30.09			

Average major oxide weight percentages are given above for individual phases and bulk NWA 8562. The average values for the bulk material were calculated by multiplying the average major oxide data for individual phases (Appendix III) by the weight percent of those phases in NWA 8562, which was determined by modal analysis (Appendix II). [1]Includes homogeneous SiO_2 polymorphs. [2]NiO content reported from EMPA was below detection limits (bdl). [3]The remaining 12.45 wt% includes accessory chromite, ilmenite, spinel, and troilite.

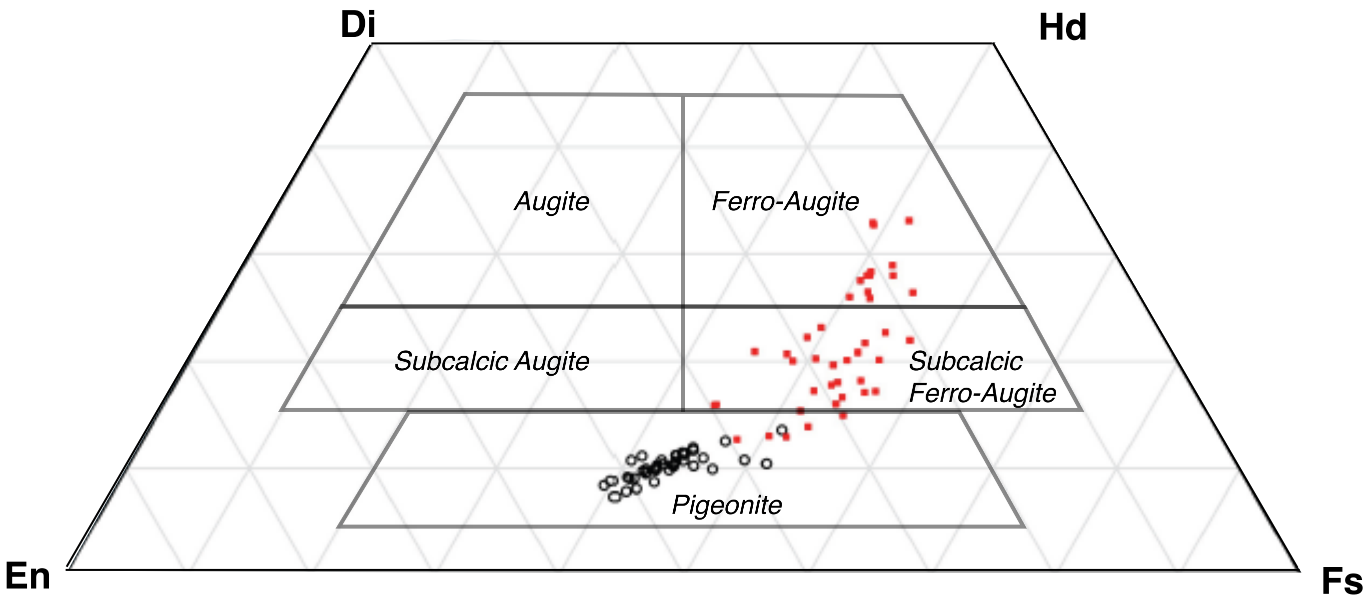

Figure 13: Pyroxene Compositions in NWA 8562
Pyroxene in the bulk unheated material is zoned from pigeonite cores to ferro-augite rims. Core compositions are shown as hollow circles, and rim compositions are red squares. Intermediate values that fall within subcalcic ferro-augite compositions may be due to the 20 μm beam size used in EMPA, which likely overlapped regions of both core and rim in pyroxene.

elements in pyroxene cluster mostly around Al, but trend toward Ti (Figure 14). Mg-numbers for pyroxenes increase toward the cores of individual crystals and from cracks. Fe/Mn ratios do not deviate far from the average (~30), which is typical for eucrites (Papike, 1998). Plagioclase composition (An_{89-92}) is homogeneous throughout both sections. Olivine is relatively homogeneous and extremely ferroan (Fa_{83-89}). It also appears to carry more phosphate (up to 0.26 wt%) than the other silicates. This perhaps is a result of apatite or merrillite inclusions in the mesostasis olivine. Ülvospinels are approximately 20 wt% TiO_2 and 44 wt% FeO (Table 2). The average composition for chromite is 33 wt% FeO, 5 wt% Al_2O_3, and 33 wt% Cr_2O_3 (Table 2). Because ilmenite occurs as very small inclusions in chromite, its exact composition could not be resolved. However, its presence likely contributes to some of the TiO_2 variations in chromite composition.

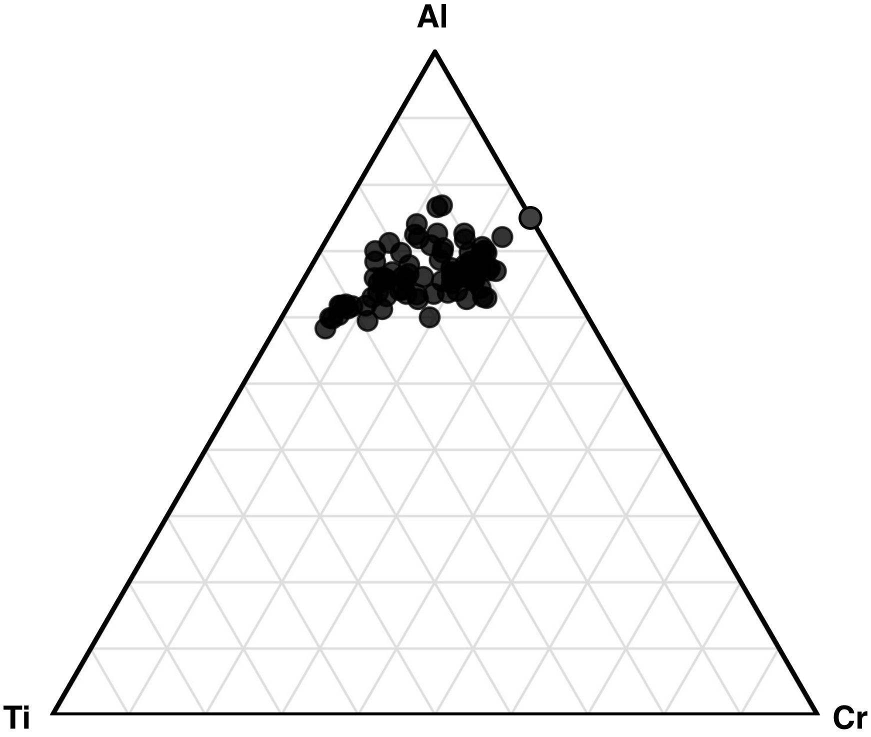

Figure 14: Minor Element Variations in NWA 8562 Pyroxenes
NWA 8562 pyroxenes are Cr-depleted and show slight variation in Al-Ti content, trending toward Ti.

Table 2: Major Element Compositions in Unheated NWA 8562 Oxides, Average Wt %

Major Oxides	Chromite n= 60	Ülvospinel[1] n= 1
SiO_2	0.1	—
TiO_2	3.8	32.22
Al_2O_3	8.5	1.81
CaO[2]	—	0.21
Cr_2O_3	51.6	7.36
FeO	34.8	56.88
MnO[2]	—	0.73
MgO	1.4	0.78
NiO[2]	—	—
Total	100.2	99.99

[1] Data for the analyzed ülvospinel is taken from spectral analysis during EMPA (Appendix III). [2] NiO wt % was below detection limits. [2] Not measured by EMPA of oxides.

4.1.4 Trace Element Geochemistry

Trace element bulk and phase compositions for the unheated NWA 8562 sample are presented in Table 3 and Figure 15. La and Hf, diagnostic incompatible trace elements in geochemical subgroup classification, (2.52 and 1.3 *μ*g/g, respectively) are consistent with Main-group eucrites. Figure 15 shows chondrite-normalized REE-enrichment that is broadly similar to the Main-group eucrite, Juvinas, which was used to represent Main-group compositions in the Barrat et al. (2007) model. NWA 8562 is slightly enriched in HREEs relative to LREEs, and possesses small positive Eu and Ce anomalies sourced from plagioclase. Pyroxene trace element content is variable in NWA 8562.1, ranging from 2-6 standard deviations for REEs (see Appendix III).

Table 3: Major and Trace Element Concentrations in Unheated NWA 8562 Phases and Bulk from LA-ICP-MS

	Na_2O	**MgO**	**Al_2O_3**	**SiO_2**	**P_2O_5**	**K_2O**	**CaO**	**TiO_2**	**MnO**	**$^1FeO_T$**				
Pyroxene	0.13	10.41	3.32	50.85	0.04	0.03	7.05	0.56	0.85	26.41				
Plagioclase	1.04	0.22	32.38	46.87	0.04	0.08	17.35	0.12	0.04	1.84				
Bulk	0.5	5.99	13.42	46.86	0.05	0.05	12.13	0.66	0.59	19.53				
	Rb	**Sr**	**Y**	**Zr**	**Nb**	**Ba**	**Hf**	**Ta**	**Th**	**U**				
Pyroxene	0.42	19.98	16.61	32.41	1.29	14.27	1.06	0.08	0.17	0.05				
Plagioclase	0.55	190.79	5.07	19.09	1.26	71.31	0.54	0.07	0.18	0.05				
Bulk	0.48	96.85	18.51	44.05	2.61	45.46	1.3	0.13	0.27	0.09				
	La	**Ce**	**Pr**	**Nd**	**Sm**	**Eu**	**Gd**	**Tb**	**Dy**	**Ho**	**Er**	**Tm**	**Yb**	**Lu**
Pyroxene	1.27	3.3	0.55	3.09	1.25	0.18	1.83	0.39	2.66	0.59	1.91	0.29	1.84	0.31
Plagioclase	2.71	5.82	0.74	3.11	0.83	1.44	0.95	0.16	0.99	0.21	0.6	0.08	0.57	0.08
Bulk	2.52	7.36	1.02	5.09	1.75	0.72	2.3	0.46	3.17	0.68	2.05	0.3	1.98	0.31

Measurements above for trace elements are given in *μ*g/g ad in wt% for major oxides. The values obtained for individual phases are average values from two sections adjacent to areas from which thin sections were taken. Bulk concentrations were averaged from rasterized analysis of unheated material. $^1FeO_T = FeO + (Fe_2O_3*0.8998)$.

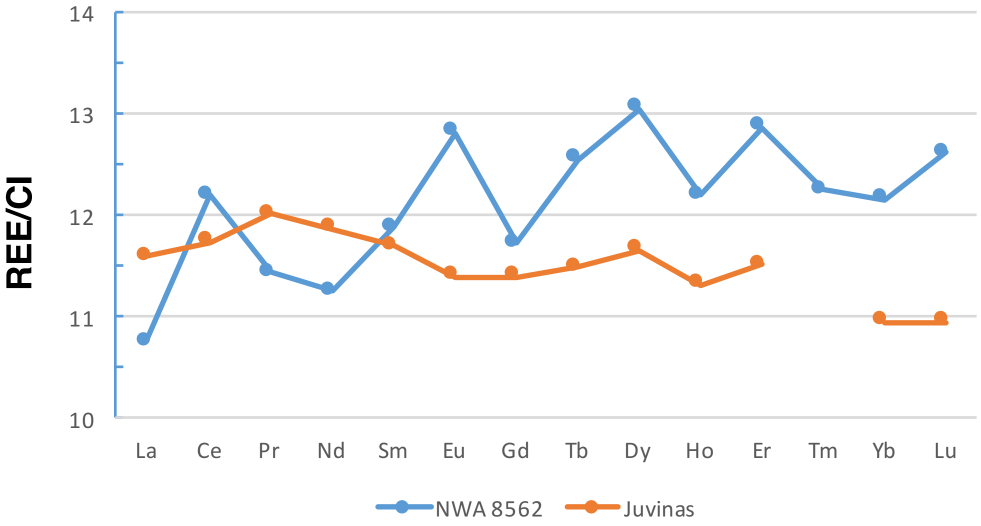

Figure 15: Rare-Earth Element Content in Bulk Unheated NWA 8562
Bulk REE content for unheated NWA 8562 normalized to CI chondrite abundance (Anders and Grevesse, 1989). The unheated sample is relatively enriched in HREEs compared to LREEs (apart from Ce, which preferentially is distributed in plagioclase). Overall, REE enrichment is comparable to Juvinas (~12x CI), but with small variations in individual REE content.

4.2 NWA 8562 Experimental Suitability

From our analyses, we have confirmed that NWA 8562 is an unbrecciated, unequilibrated eucrite, and also that it belongs to the Main-group geochemical subdivision (Figure 16). Its fine-grained texture, reasonably unaltered composition, availability of material, abundance of mesostasis, and major, minor, and trace element composition make it ideal for experimentation. These attributes reflect those of the bulk eucritic crust in the Barrat et al. (2007) model that undergoes partial melting and assimilation.

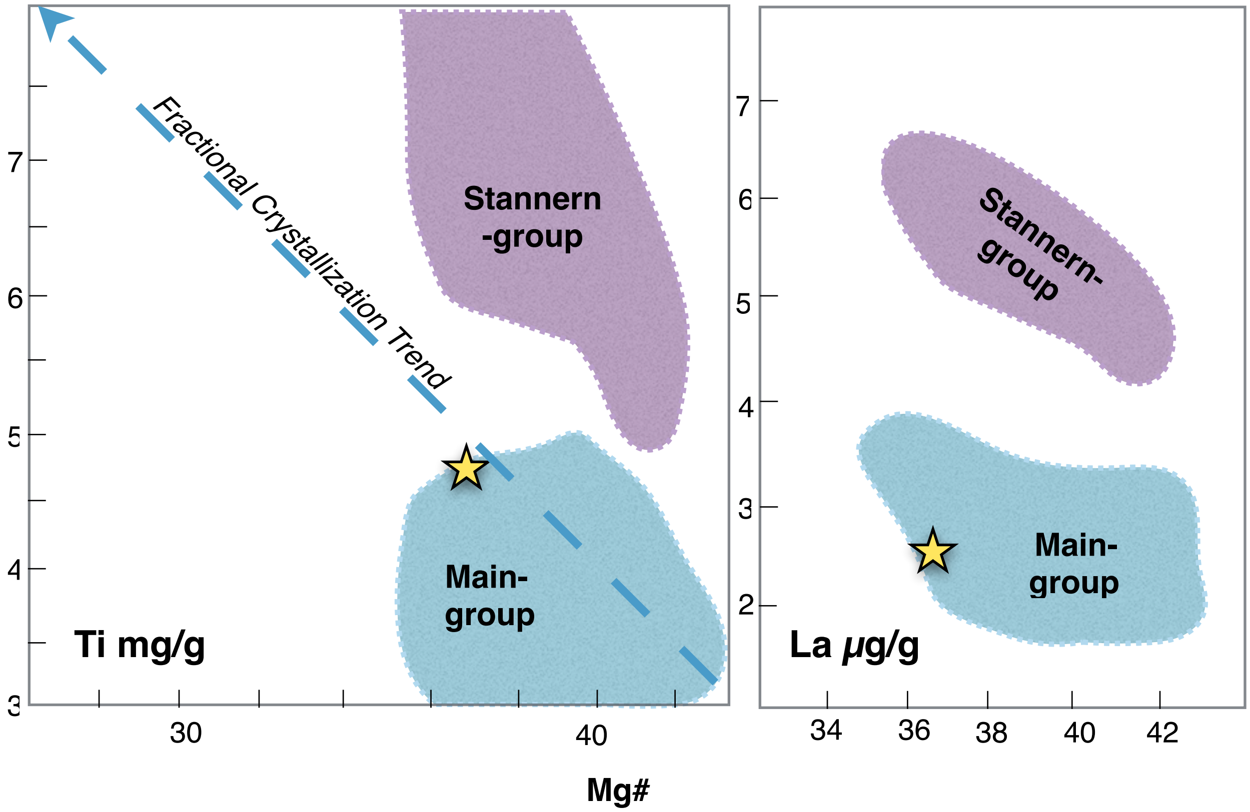

Figure 16: Geochemical Subgroup Classification of Unheated NWA 8562
Ti and La concentration versus Mg# place NWA 8562 at the more evolved end of the Main-group compositional field, with Ti = 4.8 mg/g, La = 2.52 *µ*g/g, and Mg# = 36.5. Fields are drawn from Barrat et al. (2007), Mittlefehldt (2015), and Stolper (1977).

4.3 Experimental Products

4.3.1 Petrographic Characteristics

The 1050°C run produced a 5% partial melt with the majority of melt pockets <20 *μ*m in diameter (Figure 17). In general, the texture of this run is similar to unheated material, as major phases did not experience significant partial melting. The melt is sourced from mesostasis minerals, whose relict grains (Figure 18) now possess irregular and rounded boundaries characteristic of partial melting (e.g. Yamaguchi et al., 2013). Partial laths of silica remain, although their textures have been altered by heating (Figure 18). Ferroan olivine is still present, although its boundaries have also been altered. Small melt pockets (<15 *μ*m) are seen most frequently near olivine. Plagioclase crystal boundaries appear largely unaffected, with only areas of maximum surface exposure visibly altered. The interiors of plagioclase remain relatively unaffected, and some of the irregular boundaries of plagioclase could be due to the melting of mesostasis minerals that once fit there. Pyroxene zonation is largely retained, but Fe-rich surfaces abutting mesostasis regions appear to have also marginally contributed to melting. Narrow regions between adjacent plagioclase crystals also appear to have preferentially melted (Figure 19). Oxides appear relatively unphased by 1050°C experiments.

Melting occurred more extensively (18%) in the 1100°C run (Figure 20), forming small (up to 150 *μ*m), sub-rounded vesicles in the quenched glass. Few solid silica phases remain in this run (<5 wt.%), mostly consisting of <20 *μ*m rounded tabular crystals; the remainder of mesostasis minerals appear to have completely melted (Figure 21). The largest accumulations of pyroxenes appear to retain zonation with a Mg-rich core, but the Fe-rich rims of these grains have preferentially melted. At pyroxene-plagioclase crystal boundaries, melting of Fe-rich pyroxene rims occurred more extensively, leaving behind only the relict Mg-rich cores. Plagioclase is still largely unaffected, but its rims have been partially digested, especially in

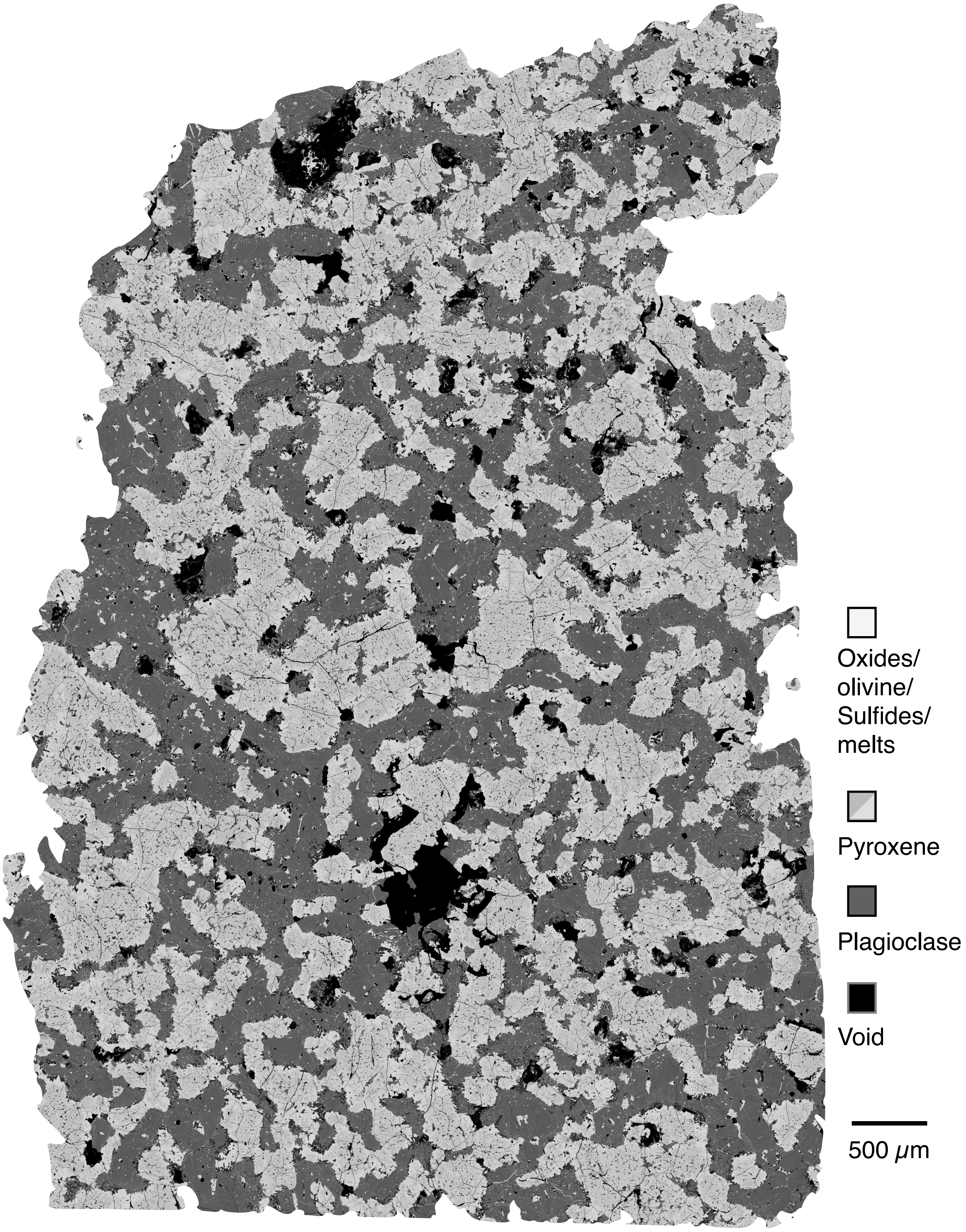

Figure 17: 1050°C Experimental Product
BSE of the 1050°C experiment, in which ~5% melting occurred (F = 0.05). Pixel value corresponds to atomic number. At this scale, original texture is largely preserved.

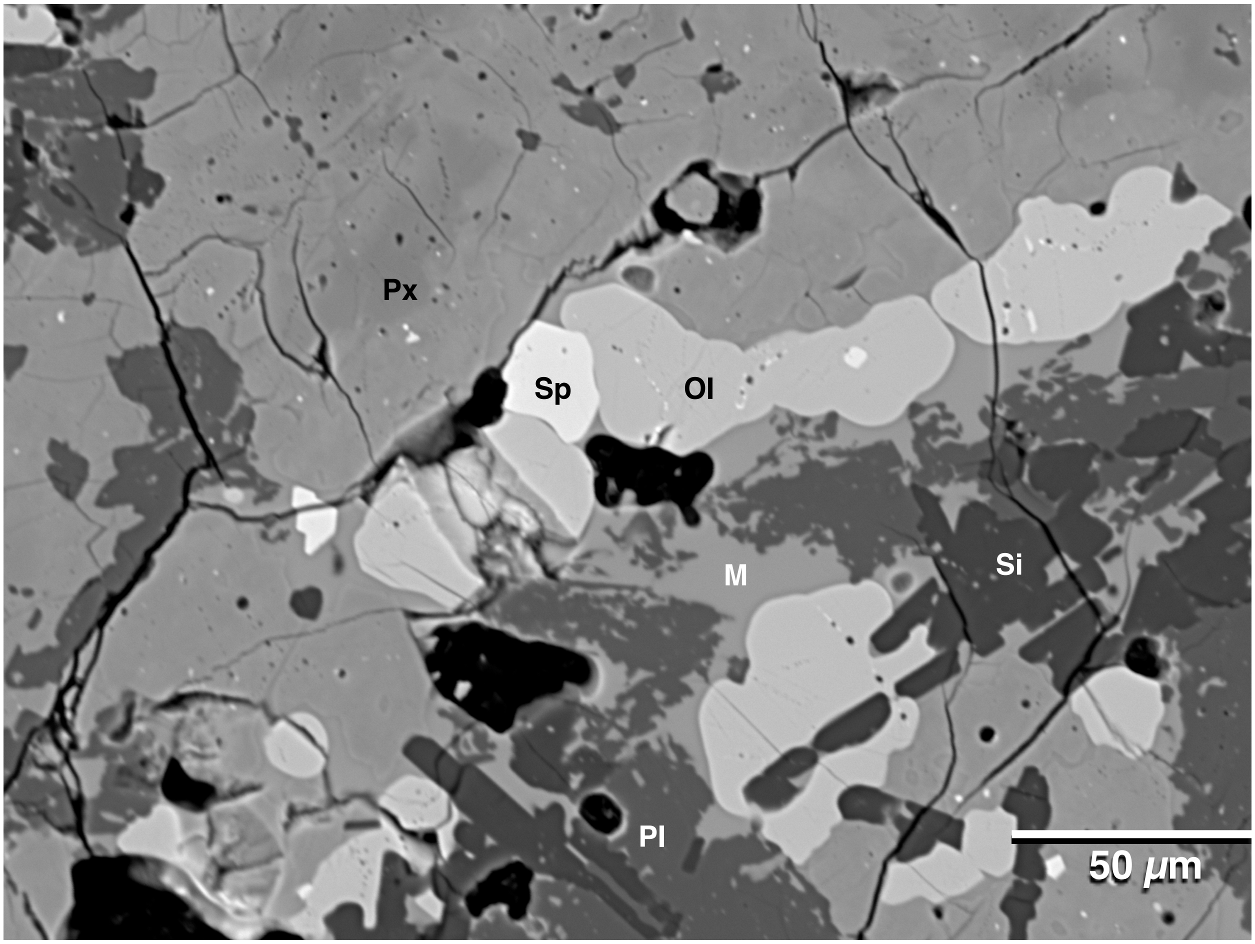

Figure 18: 1050°C Melt Region
Fine-scale BSE image of mesostasis in 1050°C experiment. Texturally, olivine and silica appear to be the most significant contributors to the melt product. The irregular boundaries of plagioclase are typical of unheated NWA 8562 material. Inclusions of ilmenite and spinel also appear to contribute to the melt, possibly accounting for observed enrichment in Ti (see section 4.2.2). Px= pyroxene, Pl= plagioclase, Ol= olivine, Sp= spinel, Si= Silica, and M= melt.

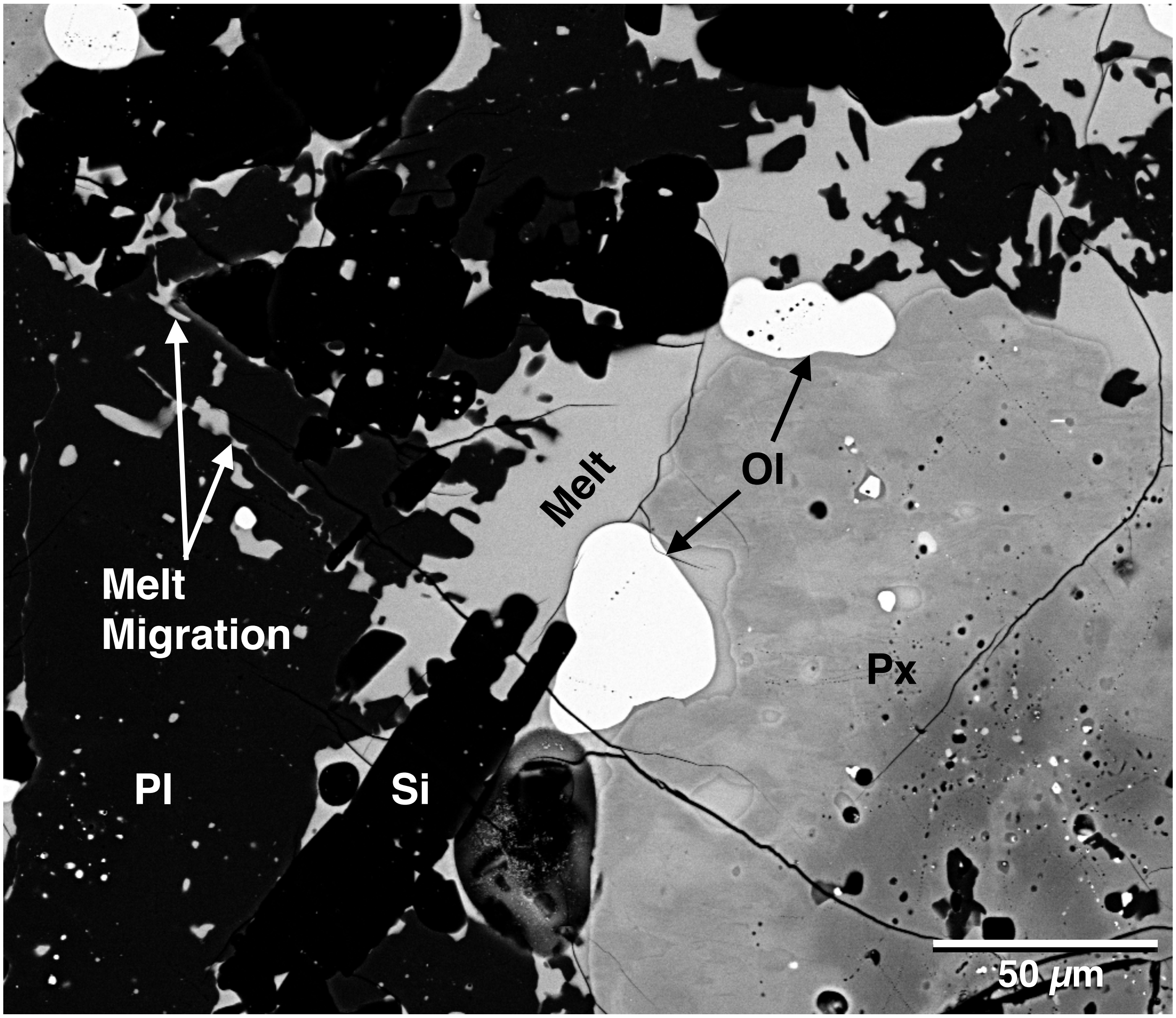

Figure 19: Low-T Melt Migration
BSE image shows the migration of melts through cracks in plagioclase at low temperature (1050°C). Ol= olivine, Pl= plagioclase, Px= pyroxene (zoned), and Si= silica phase.

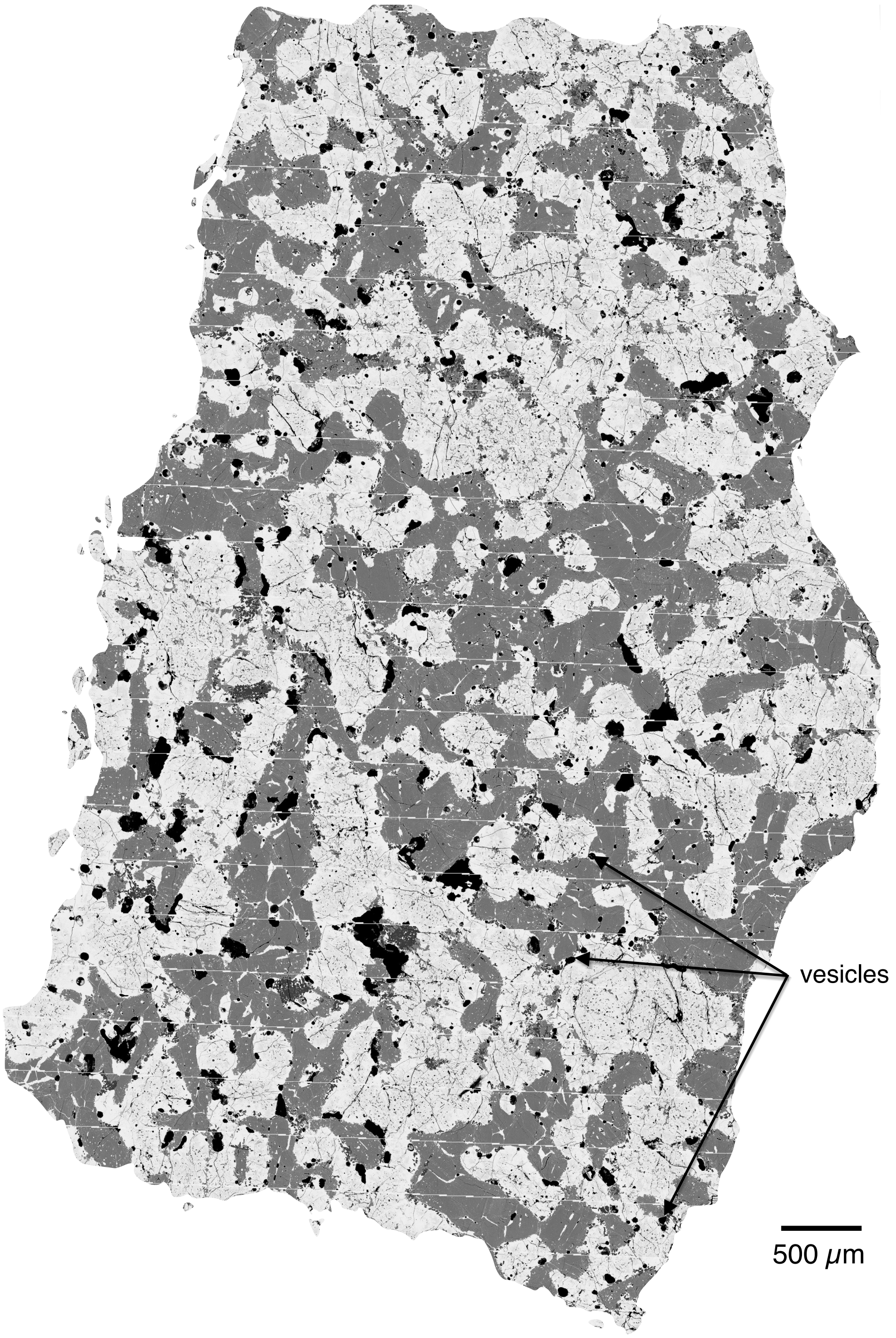

FIGURE 20: 1100°C Experimental Product
BSE composite image of the 1100°C experimental run, which produced 18% melting (F = 0.18). Irregular grain boundaries have been smoothed by melting, and pockets of melt can be seen along plagioclase-pyroxene boundaries, often spotted with vesicles. Improper calibration of the camera mounting due to user error resulted in offset tiling. Colors are the same as in Figure 14.

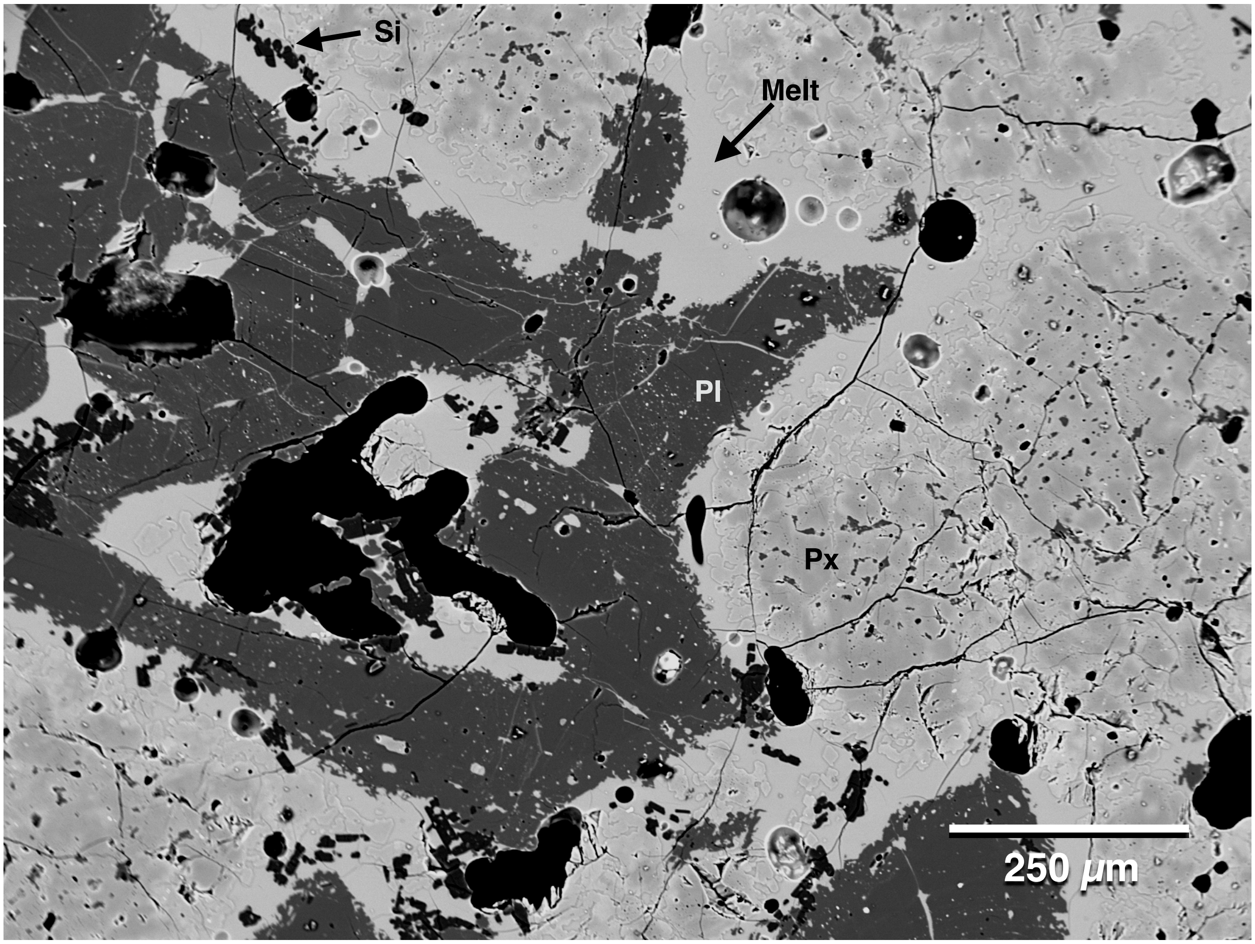

Figure 21: 1100°C Melt Region
BSE image of a typical 1100°C melt product. Melts are more clearly visible in the higher melt fraction runs, marked by a distinct boundary with pyroxene. Fe-rich rims of pyroxene were preferentially melted, leaving Mg-rich cores relatively unaltered. Plagioclase has still not contributed significantly to the melt, as evidenced by its relict, highly irregular boundaries. Most mesostasis phases have been consumed, although small laths of silica phases can still be seen, mostly clustered together as small (<50 *μ*m) agglomerations. Vesicles dot the melt product due to volatilization of the least refractory elements. Px = pyroxene, Pl = plagioclase, and Si = silica.

protuberances from the regular surfaces that were exposed to more melt material. Apparent planes of weakness within individual plagioclase crystals and between adjacent grains filled with melt material, which likely facilitated the breakdown of plagioclase at higher temperature. Several oxides and sulfides can still be seen in BSE images, and appear to be relatively intact.

At 1150°C (Figure 22), both plagioclase and pyroxene appear to have contributed equally to a 52% melt fraction. Rounded vesicles ranging in size from < 20 to > 300 μm populate the melts. Mg-rich pyroxene crystals (Figure 23) are relict cores of the original, zoned pyroxene seen in unheated material. Oxides and sulfides appear to have been largely digested in this experimental product. Melting occurred so extensively in this run that it collected and pooled against the side of the alumina crucible.

The 1200°C experiment almost completely melted the specimen (97% melt), with only a few fragments of plagioclase, Mg-rich pyroxene, and spinel remaining (Figure 24).

4.3.2 Major Element Geochemistry of Melt Products

Major element results are listed in Table 4 (and Appendix III) and are representative of the average partial melt composition in each experimental run. Contents of major oxides in the melts relative to bulk composition are presented in Figure 25. Due to the almost complete melting of the 1200°C run, its composition was used as proxy for bulk composition to calculate the major oxide distribution in melts. The melt products in all experimental runs were first examined using electron dispersive spectroscopy (EDS) to seek for heterogeneities in the melt compositions. This technique showed that the melts were homogeneous in each experiment.

Notably, in the 1050°C melt product, TiO_2 content is 7.01 times greater than the bulk composition, and P_2O_5 is 9.66 times greater than that of the original unheated bulk material. K_2O and SO_3 are also dramatically enriched (4.3 and 6.1 times the original composition, respectively). The enrichment of SO_3 in the lowest temperature experiments could be due to the preferential contribution of mesostasis troilite or due to sulfur loss via volatilization of

Figure 22: 1150°C Experimental Product
BSE composite image of the 1150°C experimental run. Melting occurred much more extensively (F = 0.51) than lower-T melts, incorporating all major phases. Vesicles are ubiquitous throughout melt glass. Colors are the same as in Figure 14.

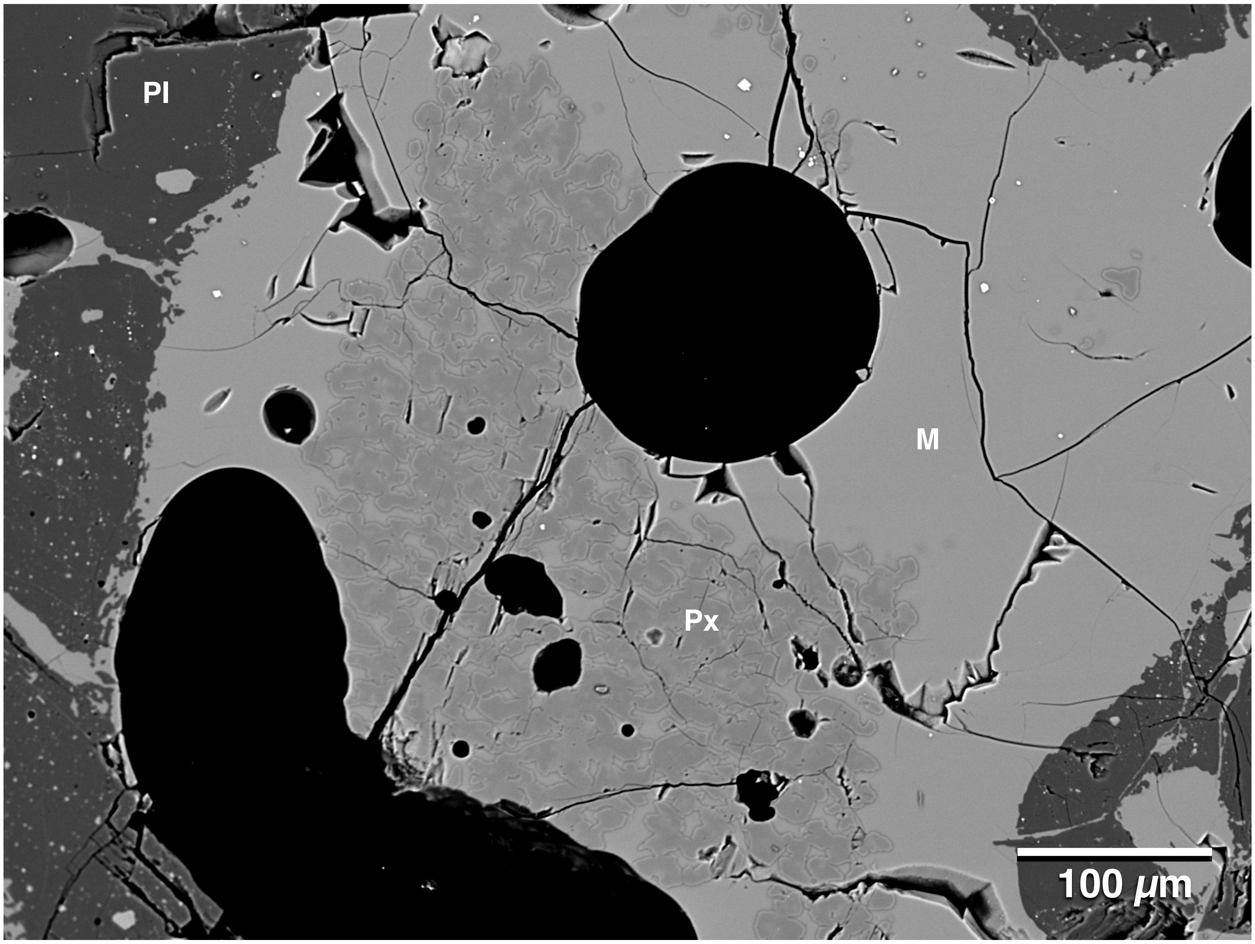

Figure 23: 1150°C Melt Region
BSE image of a melt pocket in the 1150°C experimental charge. The irregular boundaries of plagioclase seen in lower-T experiments and unheated samples have begun to smooth out at this temperature, suggesting that plagioclase has also begun to contribute to the melt. This observation is supported by trace element data for the melt (see section 4.2.3, pages 59 and 61). Remnant pyroxene is chiefly composed of its Mg-rich endmember, which are probably relict cores of the original pyroxenes of products. Px= Pyroxene, Pl = plagioclase, M = melt.

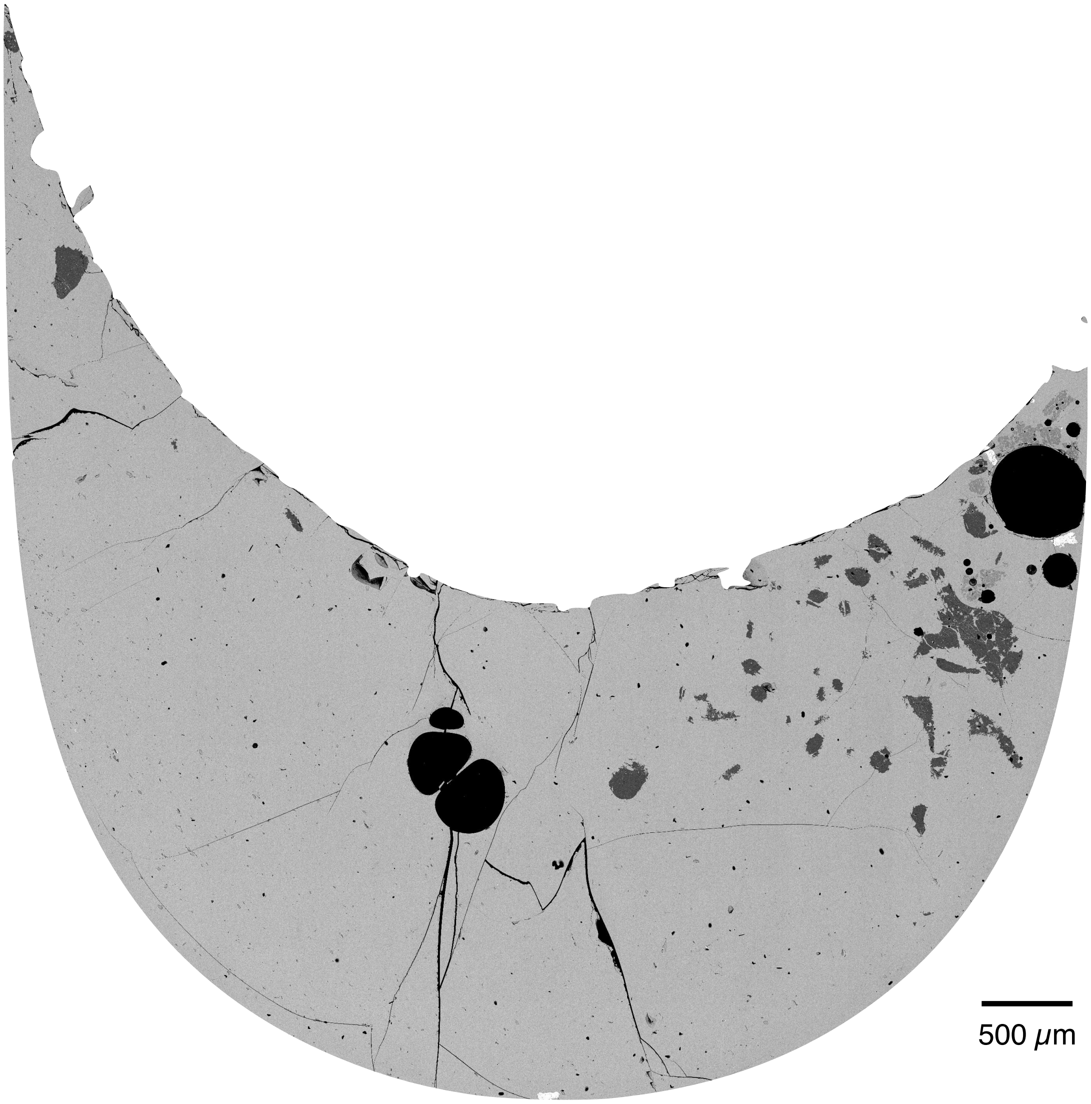

Figure 24: 1200°C Experimental Product
BSE composite image of the 1200°C experimental charge, which experienced nearly complete melting (F= 0.97). A few grains of relict plagioclase can be seen in the upper-right portion of the material. Several relict cores of pyroxene can be found in upper-right isthmus of melt, and three small oxides (shown in white) are still extant, although they are only found along vesicle and crucible walls. Colors are still the same as in Figure 14.

Table 4: Major Oxide Compositions of Experimental Melt Products

	Experimental NWA 8562 Phases Average Wt%						
Major Oxides	*1050°C*	*Relative Enrichment*	*1100°C*	*Relative Enrichment*	*1150°C*	*Relative Enrichment*	*1200°C*[1]
SiO_2	42.99	0.89	48.42	1.00	48.59	1.00	48.48
TiO_2	4.62	7.00	1.63	2.47	0.89	1.35	0.66
P_2O_5	0.6	10.00	0.13	2.17	0.08	1.33	0.06
Al_2O_3	7.19	0.55	9.46	0.72	11.34	0.86	13.18
Cr_2O_3	0.05	0.25	0.12	0.60	0.18	0.90	0.2
FeO	31.26	1.55	25.6	1.27	22.3	1.11	20.17
MnO	0.67	1.31	0.59	1.16	0.56	1.10	0.51
MgO	1.68	0.26	2.86	0.44	4.94	0.76	6.51
NiO	0.00	0.00	0.00	0.00	0.00	0.00	0.00
CaO	9.5	0.96	9.94	1.01	10.03	1.02	9.85
Na_2O	0.26	0.76	0.37	1.09	0.39	1.15	0.34
K_2O	0.12	4.00	0.04	1.33	0.03	1.00	0.03
SO_3	0.73	6.08	0.35	2.92	0.3	2.50	0.12
Total	99.67		99.52		99.54		100.11

Major element compositions for experimental melt products collected via EMPA at Oklahoma University. [1]1200°C melt composition is used as a proxy for bulk composition in subsequent major element figures, as it generated a melt fraction of F = 0.97.

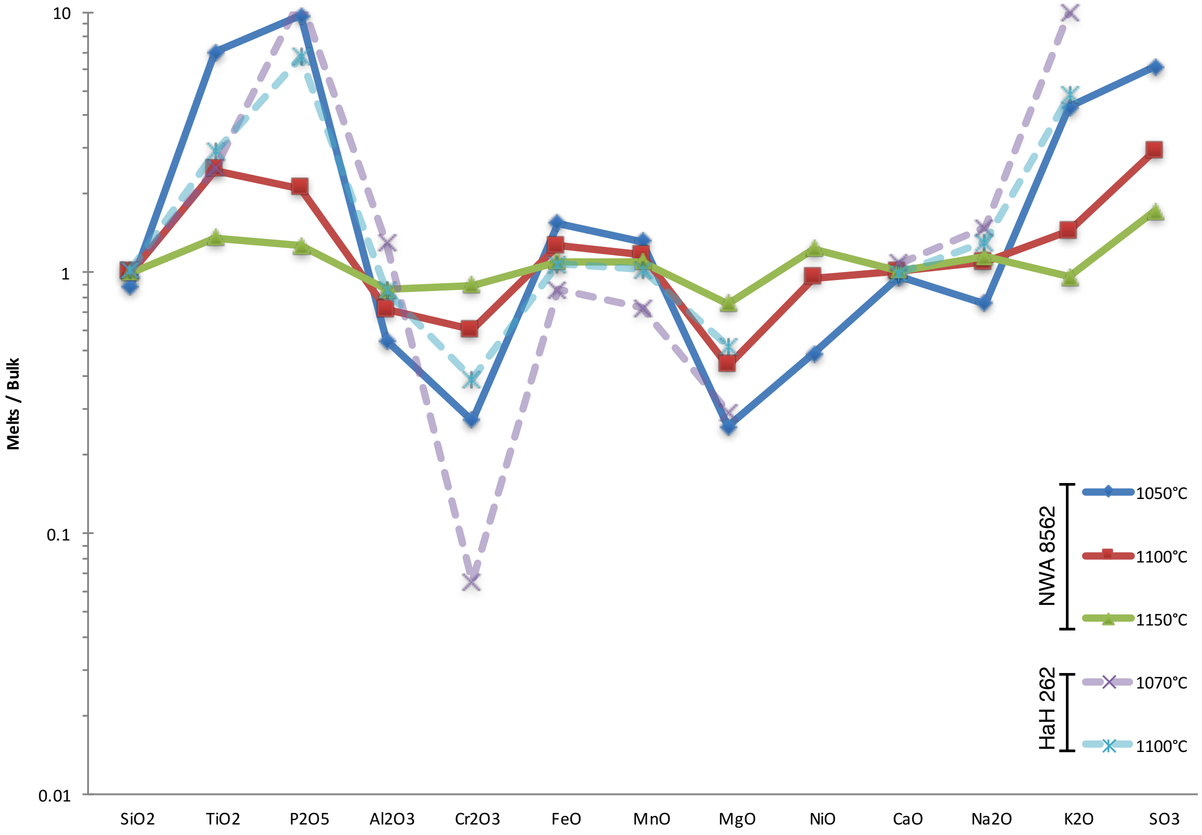

Figure 25: Major Oxide Distribution in Melt Products
Major oxide content in melt products relative to bulk composition for the three lower temperature experimental runs (1050, 1100, and 1150°C) are shown in the figure. The 1200°C melt was used as a proxy for bulk composition of NWA 8562. HaH 262 data is from Yamaguchi et al. (2013), which produced low-T melts roughly similar in major element distribution.

contributing phases at higher temperatures (e.g. Zhang et al., 2013). Without SO_3 data for the original unheated material, the distinction cannot be made without some speculation. Depleted constituents include Al_2O_3 (55% of original bulk Al_2O_3), Cr_2O_3 (27%), MgO (26%), and Na2O (24%). FeO and MnO are both enriched (55 and 32%, respectively) relative to bulk composition. Results for a similar set of melting experiments with the eucrite HaH 262 (Yamaguchi et al., 2013) are also presented in Figure 21. Overall, the trend of major oxide enrichment in the melt products is similar that of NWA 8562. In contrast to our results, FeO is relatively constant in the 1070°C melting experiments for HaH 262. Our FeO-enrichment is possibly due to contribution from Fe-rich mesostasis phases, such a fayalite and ilmenite. SiO_2 and CaO in NWA 8562 melts are very close to bulk composition, deviating less than 15% from the unheated material. NiO content was below detection limit in our experimental melts.

Melt compositions produced at 1100°C show a less dramatic variation in major oxide variation from bulk composition, due to the significantly higher melt fraction. TiO_2 content is 2.5 times that of the bulk composition, and P_2O_5 fell to 2.1 times the original. HaH 262 yielded greater P_2O_5 enrichment in their 1100°C melt, likely due to the presence of apatite in their sample. K_2O is 44% more abundant than in the bulk composition, and SO_3 is enriched 2.9 times that of the bulk composition. Cr_2O_3 and MgO are still depleted (40 and 56% less than the unheated sample, respectively). HaH 262 showed much stronger Cr_2O_3 depletions in the lowest temperature melts. The remainder of the major oxides are within several percent of the bulk composition. These are most likely due to compositional differences in the two starting materials. MgO enrichment is consistent across both sets of experiments.

Major oxide abundances in the 1150°C were largely similar to bulk composition of the unheated material, due to the large melt fraction. Most were within a few percent variation, with notable exceptions being TiO_2 (35% greater than bulk), P_2O_5 (26% greater), and MgO (24% less).

4.3.3 Trace Element Geochemistry

Unfortunately, the 1050°C melt product trace element composition could not be measured, due to its very low melt fraction (F= 0.05). However, a qualitative assessment of melt composition can be made if it is assumed that LREEs (i.e. La) increase in concentration comparably to other highly incompatible elements (i.e. P_2O_5). This will be examined in section 5.3. Major phase REE contents for each experimental run are presented in Table 5, and chondrite-normalized REE contents can be found in Table 6, Figure 26, and Figure 27. The trend of REE abundance in 1050°C pyroxene (Figure 26b) remains relatively unchanged compared to unheated pyroxene, with variations likely due to the small sample size of analyzed pyroxenes crystals (n= 4). The REEs are less abundant than in the average unheated pyroxene composition, so some pyroxene likely contributed to the melt product, even at the lowest temperature. Concentrations of lighter REEs (La-Sm) are approximately half that of the unheated pyroxene. The remainder of the REEs range from 24-37% less than the original composition. Plagioclase composition changes rather dramatically, becoming up to ~30% enriched in all REEs, apart from Eu. The enrichment of plagioclase is unexpected, and may be due to the small sample size collected (n= 5). Alternatively, the apparent enrichment of plagioclase could be due to analytical error, in which some of the regions sampled may have overlapped melt product, which would explain the enrichment of LREEs, specifically.

In 1100°C melt products, REEs are enriched (~2-3x) relative to bulk composition of the unheated sample. Broadly, the shape of the REE trend shows pyroxene signatures: negative Ce, Yb, and deep Eu anomalies, as well as HREE enrichment. This indicates that pyroxene was preferentially added to the melt over plagioclase at this temperature. The LA-ICP-MS technician additionally analyzed regions described as “black areas” in reflected light. The enrichment of REEs relative to bulk unheated composition and the general shape of the trend suggest that these areas are possibly overlapping regions of relict mesostasis and melt product. Only the

Table 5: Major and Trace Element Data for Experimental Charges

	Pyroxene			*Plagioclase*			*“Black Area”*	*Melt Product*		*Bulk*
T=	*1050*	*1100*	*1150*	*1050*	*1100*	*1150*	*1100*	*1100*	*1150*	*1200*
	n=4	*n=7*	*n=3*	*n=5*	*n=5*	*n=4*	*n=5*	*n=10*	*n=5*	*n=4*
Na_2O	0.08	0	0	1.03	0.8	0.22	0.2	0.22	0.14	0.43
MgO	11.22	11.82	13.14	0.32	0.36	0.29	3.5	4.51	4.7	5.4
Al_2O_3	2.43	2.04	2.84	30.93	31.8	32.51	11.6	8.5	10.97	12.44
SiO_2	51.41	48.63	52.47	47.78	46.62	48.96	55.38	46.9	51.77	50.48
P_2O_5	0.03	0.04	0.03	0.07	0.06	0.04	0.09	0.09	0.08	0.06
K_2O	0.01	0.03	0	0.05	0.08	0	0.06	0.06	0.01	0.03
CaO	6.08	6.64	5.32	16.17	16.9	15.82	10.57	10.26	9.72	10.07
TiO_2	0.38	0.45	0.28	0.28	0.18	0.1	0.87	1.13	0.7	0.59
MnO	0.86	0.95	0.84	0.08	0.08	0.06	0.52	0.77	0.61	0.59
FeO(t)	27.08	28.98	24.9	3.28	3.11	2.03	17.12	27.36	21.13	19.68
Rb	0.3	0.37	0	0.37	0.57	0	0.7	0.33	0	0.33
Sr	11.25	11.14	13.34	165.34	188.1	167.51	83.42	77.67	60.59	70.23
Y	10.16	12.49	7.61	10.15	8.16	4.82	27.43	31.19	19.44	14.87
Zr	16.8	22.01	14.26	37.64	31.79	19.53	66.36	71.42	44.24	35.76
Nb	0.57	0.89	0.72	2.72	2.36	1.41	3.46	4.32	2.83	2.17
Ba	7.71	10.49	7.34	62.54	71.33	65.27	51.67	59.66	34.17	34.24
La	0.59	0.95	0.63	3.45	2.82	2.65	3.68	4.48	2.4	2.2
Ce	1.49	2.31	1.64	7.66	6.13	5.35	7.57	10.63	5.87	5.5
Pr	0.27	0.43	0.26	1.1	0.87	0.67	1.4	1.79	1.04	0.87
Nd	1.68	2.56	1.44	5.63	4.22	3.61	7.83	10.11	5.87	4.57
Sm	0.74	1.07	0.51	1.48	1.17	1.27	2.7	3.43	2.16	1.52
Eu	0.12	0.12	0.16	1.43	1.58	1.42	0.79	0.96	0.68	0.68
Gd	1.3	1.77	0.89	1.9	1.49	0.95	3.91	4.97	2.84	2.29
Tb	0.23	0.32	0.18	0.35	0.25	0.21	0.74	0.9	0.47	0.44
Dy	1.79	2.39	1.32	2.05	1.68	1.37	4.61	6.67	3.68	2.8
Ho	0.42	0.53	0.29	0.42	0.37	0.23	0.89	1.5	0.73	0.64
Er	1.27	1.72	0.77	1.2	0.96	0.75	3.36	4.45	2.24	1.83
Tm	0.21	0.27	0.15	0.2	0.17	0.1	0.41	0.66	0.36	0.24
Yb	1.31	1.39	1.26	1.12	1.05	0.7	2.81	4.07	2.13	1.63
Lu	0.22	0.26	0.12	0.15	0.13	0.13	0.49	0.73	0.4	0.3
Hf	0.78	0.97	0.59	1.06	1.01	0.74	1.87	2.61	1.49	1.21
Ta	0.03	0.07	0.04	0.15	0.16	0.07	0.23	0.36	0.19	0.13
Th	0.1	0.17	0.07	0.38	0.4	0.25	0.4	0.56	0.33	0.29
U	0.02	0.05	0.02	0.11	0.11	0.05	0.1	0.18	0.09	0.07

LA-ICP-MS analyses of experimental charges. Temperatures (T=1050, 1100, 1150, and 1200) are given in °C, oxides are given in wt%, and trace element concentrations are given in *μ*g/g, and were averaged from individual spot analyses. “Black areas” were not specifically identified by the LA-ICP-MS technician, but may be overlapping areas of relict mesostasis phases and melt products.

Table 6: Chondrite-Normalized Trace Elements in Melt Products

Trace Element	*Bulk*	*1100°C Melt*	*1150°C Melt*	*1200°C Melt*
La	10.75	19.08	10.23	9.39
Ce	12.20	17.63	9.73	9.12
Pr	11.43	20.14	11.62	9.76
Nd	11.25	22.34	12.97	10.09
Sm	11.88	23.32	14.65	10.35
Eu	12.82	17.09	12.08	12.19
Gd	11.72	25.26	14.43	11.65
Tb	12.55	24.67	12.97	12.04
Dy	13.04	27.50	15.17	11.55
Ho	12.19	26.97	13.15	11.52
Er	12.87	28.01	14.11	11.53
Tm	12.25	27.27	15.07	9.74
Yb	12.16	25.07	13.10	10.01
Lu	12.61	29.88	16.41	12.17

Chondrite-normalization for melt products was calculated according to CI abundance in Anders and Grevesse (1989).

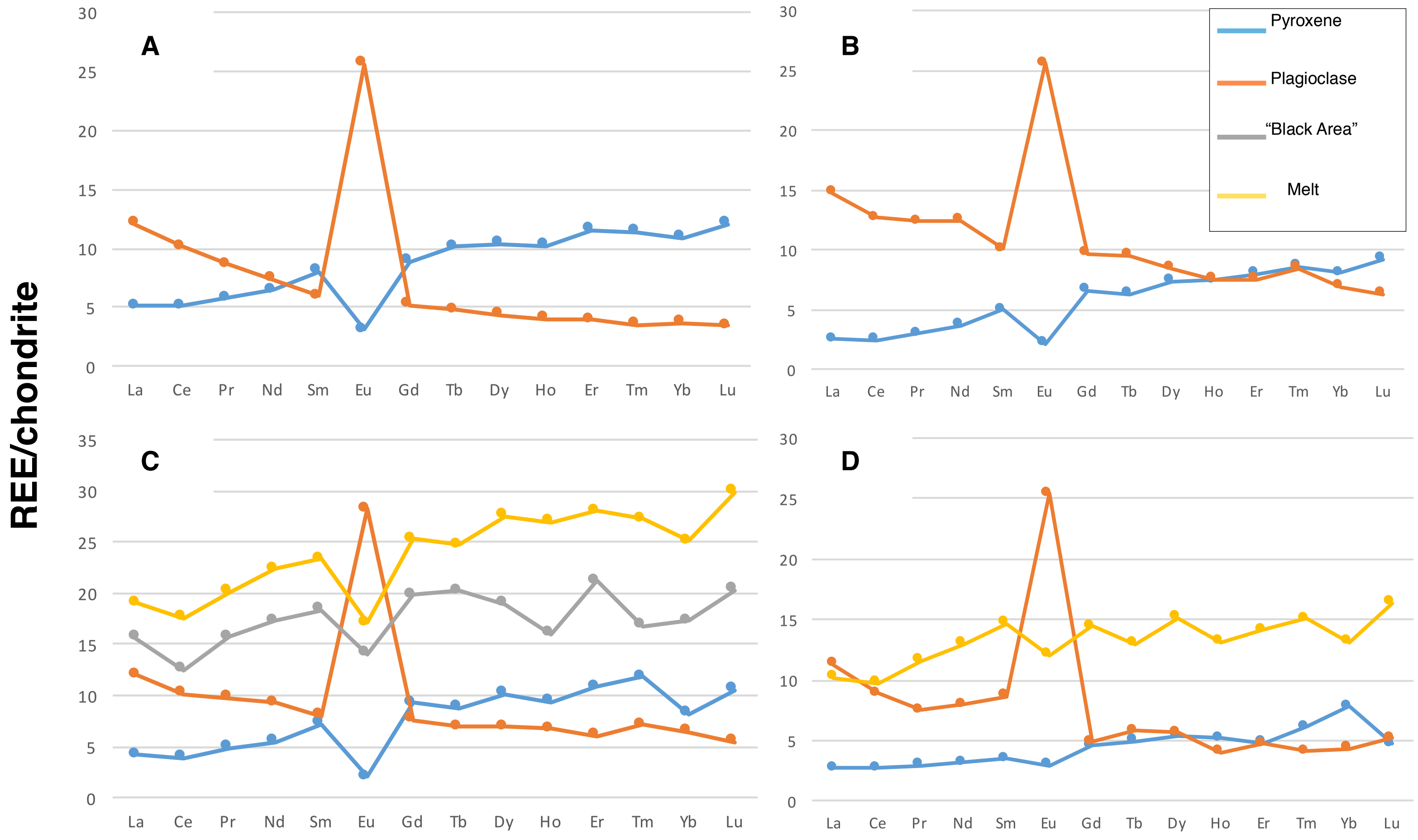

Figure 26: REE Content for Major Phases in Unheated and Experimental Samples
REE measurements for a) Pyroxene and plagioclase in unheated NWA 8562; b) 1050°C pyroxene and plagioclase; c) 1100°C pyroxene, plagioclase, unidentified "black area" (possibly overlapping regions of relict mesostasis and melt), and melt product; and d) 1150°C pyroxene, plagioclase, and melt product.

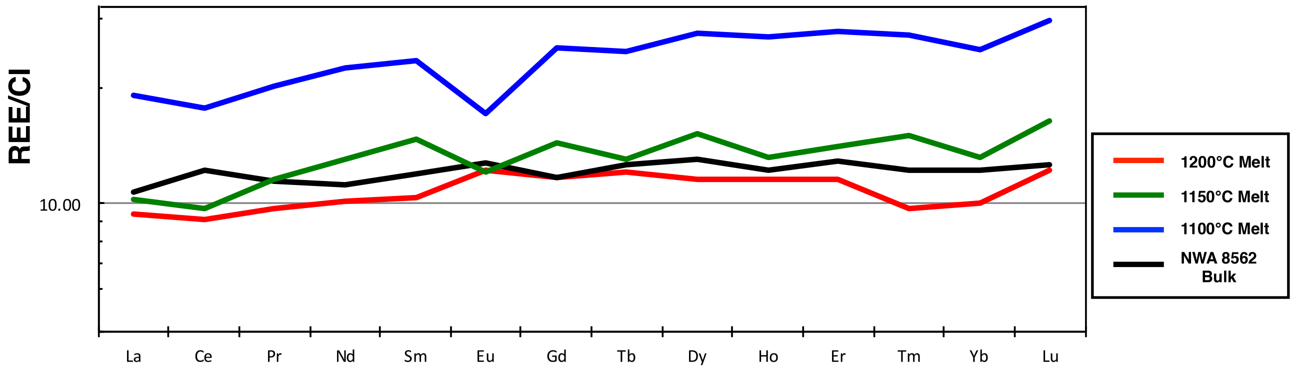

Figure 27: REE Compositions of Bulk NWA 8562 and Melt Products
The above figure shows REE compositions of the melt products relative to CI in each of the experimental charges analyzed. The 1100°C melt is enriched approximately twice that of the bulk REE content.

1100°C sample analysis included this category, which makes interpretation of the results somewhat tenuous. The assumption that this includes mesostasis and melt product seems to be plausible, because no resolvable mesostasis minerals remain in the higher temperature experiments. Some typical features of mesostasis phases and/or melt products (roughly equivalent CaO, intermediate values of Sr, etc.) can be seen in Table 5 and Figure 26(c), but variations from average melt composition also suggest inclusion of pyroxene and plagioclase. It seems plausible that these areas are fine-grained intergrowths of pyroxene, plagioclase, and mesostasis phases seen throughout the sample. Pyroxene composition in this run is slightly depleted in LREEs relative to HREEs (Figure 26c). Plagioclase shows a variable enrichment in many REEs, but this may again be due to the small sample sized of analyzed crystals (n= 5), as no other evidence (i.e. enrichment of Eu) suggests that plagioclase contributed to the melt.

The 1150°C run (Figure 26d) yielded a melt that much more closely resembles the unheated REE composition. La and Ce are approximately equal to bulk composition. Heavier elements (Pr-Lu) are enriched 30-50% greater than bulk. The lack of a distinctive Eu anomaly suggests that plagioclase contributes appreciably to the melt at this temperature, along with pyroxene. Residual pyroxene compositions are further depleted in all REEs (~50% lower than the 1100°C pyroxenes), apart from Eu and Yb.

The 1200°C run yielded a melt that is similar to the composition of the unheated starting material. Small discrepancies between the two REE patterns are likely due to the ~3% relict material, which is mostly plagioclase with a few oxides and remnant Mg-rich pyroxene.

5.0 Discussion

5.1 Petrogenetic History of NWA 8562

NWA 8562 is sourced from Main-group compositional magma that cooled rapidly from ~1200°C at or near the surface of the HED parent body (Stolper, 1977). Pyroxene and plagioclase crystallized simultaneously, as indicated by subophitic textural relationships (Mason, 1962, Duke and Silver, 1968), and Al-Ti minor element trends in pyroxenes support this interpretation (Figure 28). Cr-depletion in pyroxene also implies that crystallization occurred after the depletion of Cr in the eucrite petrogenetic sequence, due to its compatibility in early-crystallized pyroxene (Pun and Papike, 1996). Pyroxene and plagioclase then competed for Al, and pyroxene was pushed toward more Ti-rich compositions. The Mg-rich pigeonite cores were the first pyroxene constituents to crystallize. This can be observed in the 1150°C melt experiments in this study (Figure 23, page 51), where fine-grained, Mg-rich pigeonite is the only extant pyroxene, likely denuded from original ferro-augite rims. The homogeneous composition of plagioclase indicates that the phase did not change significantly during crystallization, and the lack of a negative Eu anomaly suggests that the magma did not fractionate a significant amount of plagioclase, as it would if temperature had decreased more slowly at depth. Additionally, the slight depletion in LREEs would suggest that NWA 8562 magma originated from a somewhat depleted mantle source. However, the Ti-rich and ferroan nature of the sample suggest that the magma is more evolved. Clearly, other factors were at play in the petrogenesis of NWA 8562. As temperature dropped below 1090°C, silica laths began to crystallize along pyroxene-plagioclase boundaries, followed by mesostasis phases (Stolper, 1977). Alternatively, silica, olivine, and secondary augite along primary pyroxene boundaries may result from the breakdown of metastable ferro-augite, but unfortunately the beam size (20μm) of EMPA conducted in this study failed to clearly resolve fine-scale compositional variations in pyroxene.

5.1.1 Post-Crystallization Alteration

A wide range in the degree of metamorphism has been observed in many eucrites, allowing their further subdivision into petrologic types 1-6, where increasing number reflects increasing metamorphic grade (Figure 29) (Takeda and Graham, 1991; Pun and Papike, 1996; Mayne et al., 2009). The degree of metamorphism is indicated by equilibration of igneous pyroxene exsolution lamellae and the presence or absence of mesostasis glass (Takeda and

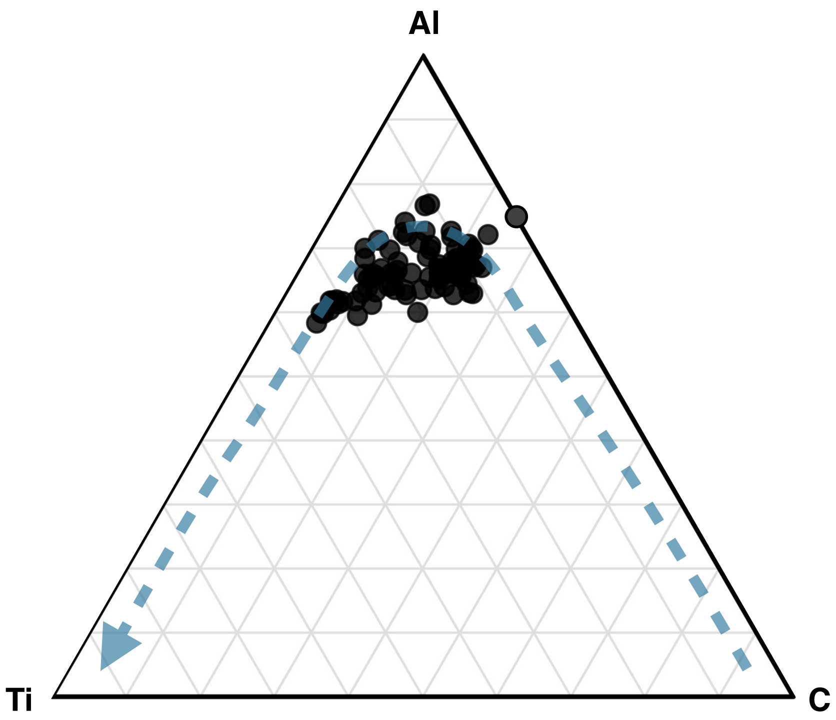

Figure 28: Minor Element Variations in NWA 8562 Pyroxenes
The magmatic trend (dashed blue line) for pyroxene minor element content was drawn after Pun and Papike (1996).

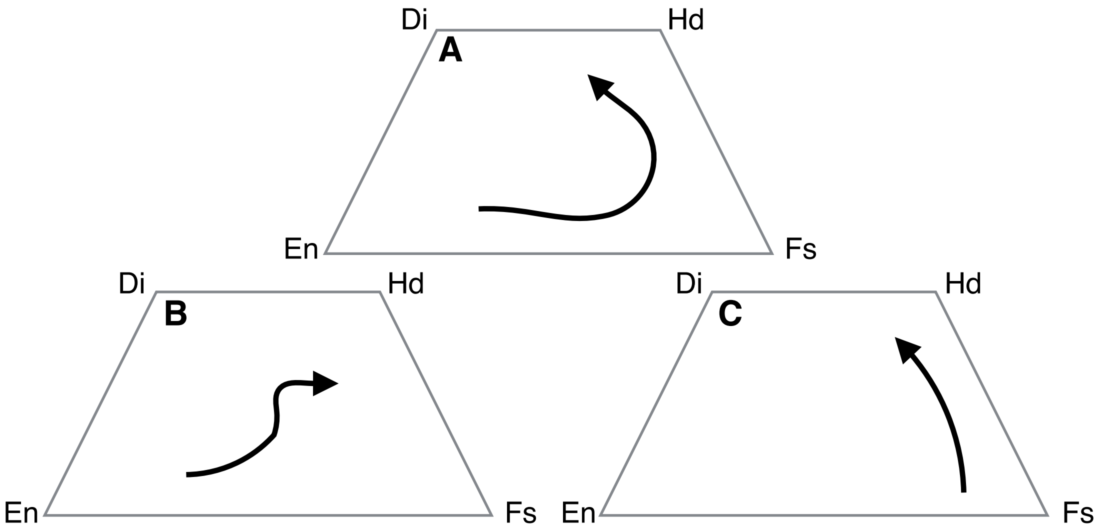

Figure 29: Eucrite Petrologic Types
Pyroxene compositions are used to determine petrologic types of eucrites. (A and B) Unequilibrated pyroxenes (type 1 and 2). Trend (A) corresponds to type 2 in the Takeda and Graham (1991) classification, while (B) reflects type 1 pyroxene zonation. (C) Shows the trends for equilibrated eucrites, tying exsolved augite lamellae to pigeonite. Trends are drawn after Pun and Papike (1996) and Mayne et al. (2009).

Graham, 1991). Type 1 eucrites preserve original igneous chemical zonation of major elements in pyroxenes, mesostasis glass, and very fine-scale (irresolvable by EMPA) exsolution lamellae of Ca-rich augite in pigeonite (more highly metamorphosed pyroxenes contain Ca-rich lamellae that can be distinguished by EMPA [Takeda and Graham, 1991]). NWA 8562 matches all of these criteria, confirming that it is an unequilibrated, type 1 eucrite (Figure 30) (Takeda and Graham, 1991; Pun and Papike, 1996; Mayne et al., 2009). Some discrepancies between the general trend for type 1 eucrites and NWA 8562 may be explained by the relatively wide 20 μm beam size used for analysis, as intermediate compositions could represent measurements that overlapped both core and rim compositions. It can also be inferred from the lack of thermal alteration that the source region for NWA 8562 is one of the youngest basaltic lithologies produced on its parent planet (Yamaguchi et al., 1997).

The breakdown of pyroxene, ubiquity of very fine-scale (<5 μm) troilite, presence of P_2O_5 in ferroan olivine, and Fe-enriched fractures in mosaic pyroxenes indicate that post-crystallization alteration occurred, either as products of impact or vapor-driven metasomatism (Schwartz and McCallum, 2005; Zhang et al., 2013; Warren et al., 2014). Similar features have been interpreted as products of metasomatism in HEDs, but the metasomatic agent and processes on the HED parent body are not well-constrained (e.g. Mittlefehdlt and Lindstrom, 1997; Treiman et al., 2004; Schwartz and McCallum, 2005; Barrat et al., 2011; Zhang et al., 2013; Warren et al., 2014). Distinctions between the possible sources of Fe-enriched rims in pyroxene can be found by utilizing Fe/Mn ratios in pyroxenes (e.g. Zhang et al., 2013), but samples analyzed with this technique appear much more significantly altered than NWA 8562. Highly metasomatized eucrites yield variable Fe/Mn ratios, which preclude igneous origins for Fe-enrichment (Mittlefehdlt and Lindstrom, 1997). Fe/Mn ratios in NWA 8562, however, are consistent (~30) across zoned pyroxenes, suggesting that Fe-enrichment is not metasomatically derived (Figure 31). Eucrite pyroxenes that have experienced low degrees of metasomatism

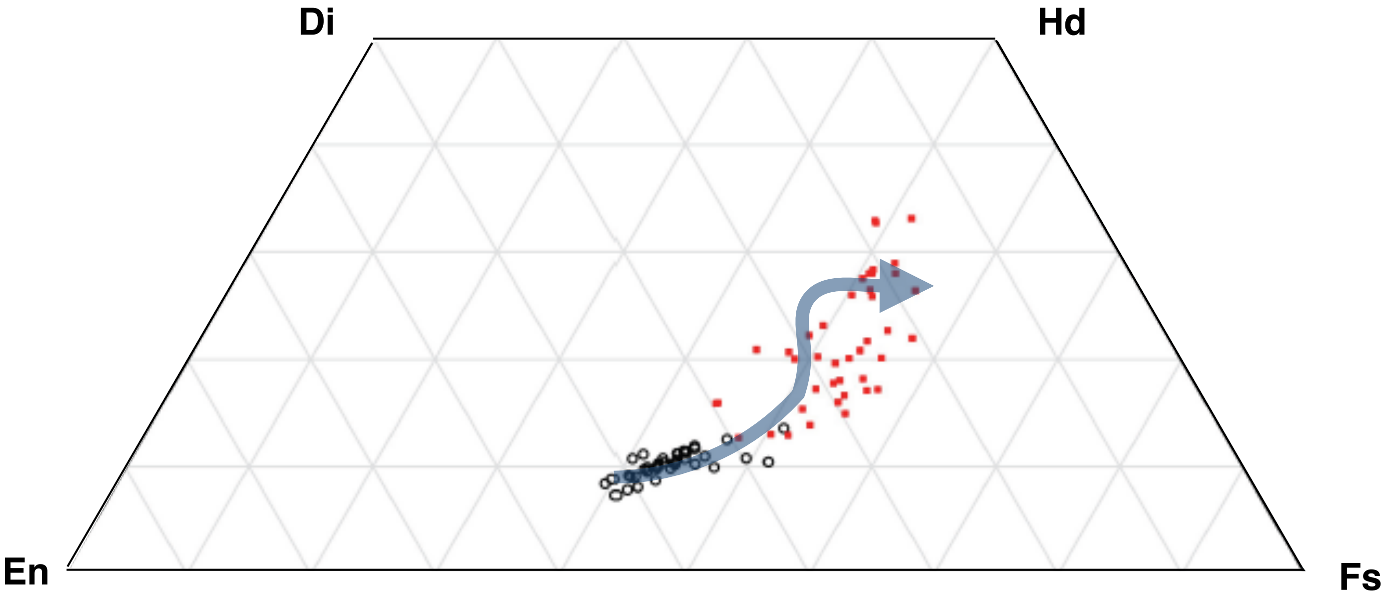

Figure 30: Pyroxene Type Classification
NWA 8562 pyroxenes generally follow the Mg-Fe trend seen in Type 1 eucrites, drawn as the blue arrow. (Pun and Papike,1996; Ikeda and Takeda, 1991). Intermediate compositions are likely the result of the 20 μm beam overlapping pyroxene cores (hollow circles) and rims (red squares).

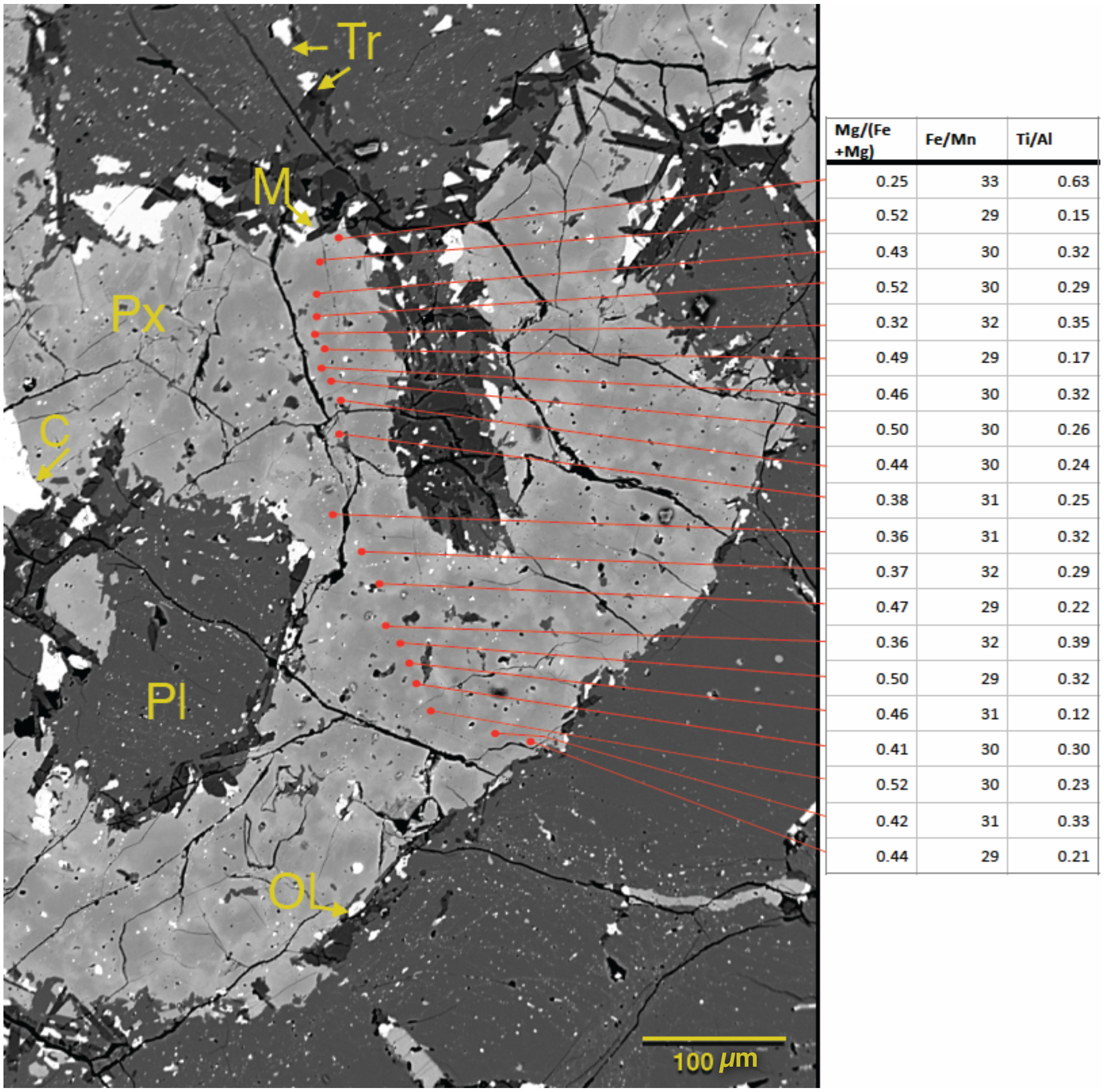

Mg/(Fe +Mg)	Fe/Mn	Ti/Al
0.25	33	0.63
0.52	29	0.15
0.43	30	0.32
0.52	30	0.29
0.32	32	0.35
0.49	29	0.17
0.46	30	0.32
0.50	30	0.26
0.44	30	0.24
0.38	31	0.25
0.36	31	0.32
0.37	32	0.29
0.47	29	0.22
0.36	32	0.39
0.50	29	0.32
0.46	31	0.12
0.41	30	0.30
0.52	30	0.23
0.42	31	0.33
0.44	29	0.21

Figure 31: EMPA Transect of NWA 8562 Pyroxene
BSE image of unheated NWA 8562 shows compositional variations across pyroxenes containing Ti/Al ratios that increase with decreasing Mg#, indicating a non-metasomatic origin (Mittlefehdlt and Lindstrom, 1997). Tr= troilite, M= mesostasis, Px= pyroxene, C= chromite, Pl= plagioclase, and Ol= olivine.

also possess Ti/Al ratios that do not vary significantly with changing Mg# (Barrat et al., 2011). NWA 8562 pyroxenes fit a magmatic trend, with Ti/Al increasing as Mg# decreases from core-to-rim (Figure 32). Warren et al. (2014), observed that the preservation of metasomatic textures implies post-metamorphic alteration on the HED parent body, implying that metasomatism would likely be driven by impact-volatilzation of the least refractory minerals. Barrat et al. (2011) observed Fe-rich compositions cross-cutting pyroxene crystals along fractures, along with fine-grained fayalite and anorthitic plagioclase, and suggested an aqueous, fluid-mediated metasomatism, based on terrestrial analogs. Schwartz and McCallum (2005) attributed Fe-enrichment of some pyroxenes to a late-stage, dry, Fe-rich, vapor-driven metasomatism. Zhang et al. (2013) observed the partial replacement of pigeonite and ferro-augite by fine-grained troilite, Mg-rich pyroxene, and a silica phase. Impact-volatilization is also the metasomatic mechanism put forward in their study, suggesting that mobilization of S and Fe-rich vapors could account for the alteration of pyroxenes seen in some eucrites and eucritic clasts in howardites. It is unclear if NWA 8562 experienced low-grade metasomatism. Although some of the aforementioned textures appear analogous to more significantly altered eucrites, the magmatic trend of Ti/Al in pyroxene suggests otherwise. NWA 8562 has possibly have experienced a very low degree of metasomatism. The mosaic texture of pyroxene implies that the NWA 8562 source region experienced impact, but the timing of that event cannot currently be constrained. Impact-volatilization, advocated by Warren et al. (2014) and Zhang et al. (2013), may account for the absence of apatite and merrillite in our analyses of NWA 8562, as well as the ubiquity of fine-grained troilite throughout mesostases and inclusions in plagioclase.

In summary, NWA 8562 crystallized at or near the surface from a Main-group magma rather late in the petrogenetic history of its parent body. Though major and minor elements suggest that NWA 8562 experienced little to no thermal metamorphism, minor alteration of the texture and composition of the mesostasis assemblage may have occurred during impact.

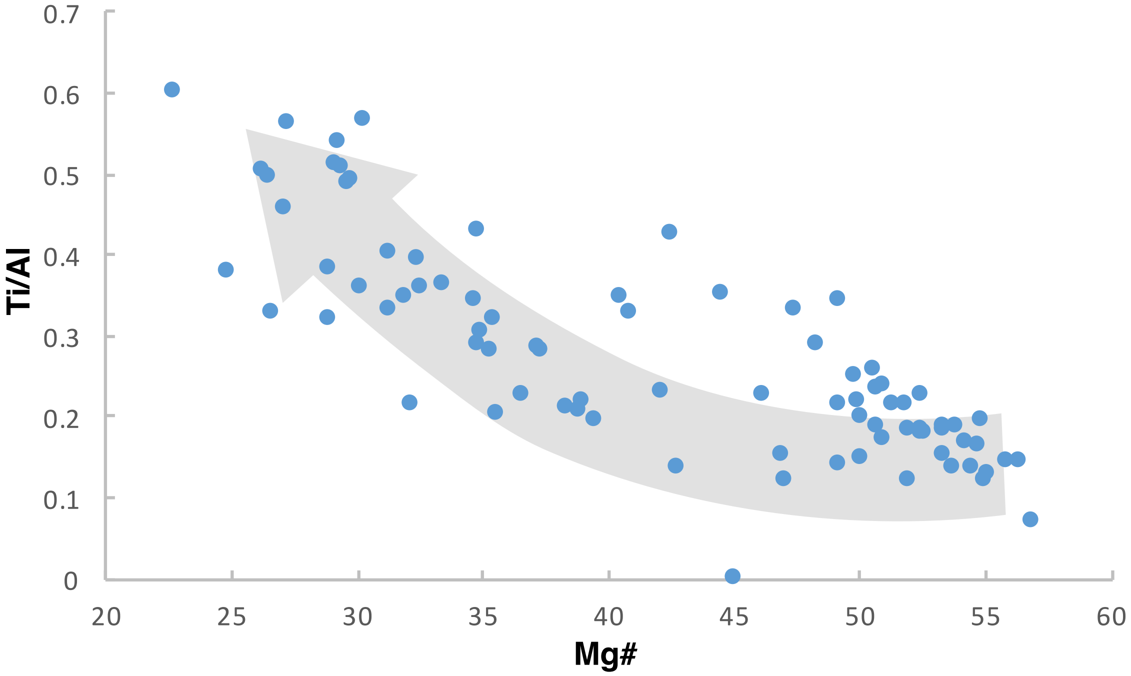

Figure 32: Ti/Al in NWA 8562 Unheated Pyroxenes
Ti/Al ratios in pyroxene follow a magmatic trend, shown by the gray arrow (Pun and Papike, 1996). More ferroan endmembers are correspondingly enriched in Ti and depleted in Al. Al_2O_3 wt% never falls below 0.05, suggesting that the Fe-enrichment seen in pyroxene rims is not metasomatically-derived. The magmatic trend is drawn after Barrat et al. (2011). It should be noted that analytical locations were not documented, so outliers from the magmatic trend may represent secondary pyroxenes. More precise analysis is required for further clarification.

5.2 Can Partial Melt Assimilation Produce Stannern-group Eucrites?

In the experiments, LREEs show an expected trend of being more enriched in smaller melt fractions. It is unfortunate that trace element compositions of the mesostasis minerals could not be determined using LA-ICP-MS techniques, as the majority of REEs in eucrites are contained in the mesostasis phases (e.g. Hsu and Crozaz, 1996; Yamaguchi et al., 2013). In NWA 8562, olivine is of particular interest, because it carries the majority of P_2O_5, likely as inclusions within the olivine crystals. Ca-phosphates were identified as an important carrier phase of most REEs (Hsu and Crozaz, 1996; Yamaguchi et al., 2013) in eucrites. Additionally, the inability to locate the 5% melt fraction in the 1050°C run during LA-ICP-MS analysis is problematic, because these melts should be the most dramatically enriched in incompatible elements, making them critical for testing the model in question. These two factors prohibit the calculation of distribution coefficients for REEs in the 1050°C melt, as the trace element compositions for all relevant phases are required for calculating bulk distribution coefficients (*D*) in mixing equations (DePaolo, 1981). A rough estimate of REE content in the low temperature experiment may be made by using major element distribution, specifically TiO_2 and P_2O_5, as a proxy for trace element distribution (Yamaguchi et al., 2013). It should be noted that these calculations likely do not accurately reflect real results, as even relatively simple geochemical systems involve the interplay of myriad factors that are unaccounted for here. These estimates, however, can be used to draw tentative conclusions and lead follow-up research in a productive direction. Bulk distribution coefficients for relevant major elements were calculated for incorporation into mixing equations (Hanson et al., 1978; DePaolo, 1981). Relative enrichment in P_2O_5 for the four melt products could be used as an upper limit for LREE content (specifically La). P_2O_5 is incompatible in eucritic mineral assemblages, as seen in the P_2O_5-enriched, smallest melt fractions in this study (calculated $K_d = 0.03$ and 0.04 for P_2O_5 in clinopyroxene and plagioclase, respectively), so it may be appropriately used here as a proxy for La. There is precedence for this approximation, as Yamaguchi et al. (2013) found that La enrichment was approximately equal to P_2O_5 enrichments in measured melt products. Ti is also considered an incompatible element in the eucrite mineral assemblage, with very similar K_d values to La with regard to plagioclase (~0.03). The La K_d value for clinopyroxene (~0.032) is an order of magnitude lower than that of Ti (~0.27), which can explain the greater enrichment of TiO_2 over P_2O_5 in the 1100°C melt, where pyroxene began to contribute appreciably to the melt product. Assuming that TiO_2 partitioning would decrease without the contribution of pyroxene at a lower partial melt fraction, we can assess the enrichment of these two components relative to bulk content, and provide upper and lower constraints on probable LREE enrichment within the 1050°C melt. This would yield an enrichment of La in the 5% melt fraction at 7.01 to 9.66 times the average bulk unheated material, with a resultant concentration of 17.67 to 24.34 μg/g La in the melt product (Figure 33).

5.2.1 Incorporation of Data into the Barrat et al. (2007) Model

Calculated magma mixture compositions for simple binary mixing are presented in Table 7 and Figure 34 for low melt fraction compositions (i.e. 1050°C and 1100°C experimental melts). The calculations were made under conditions in which melts were assimilated into Main-group magma (represented by bulk NWA 8562) at proportions of 5, 10, and 15% contaminant. Additionally, trace element contents for calculated mixtures of HaH 262 and Juvinas are presented for comparison. According to our calculations, a melt fraction of F= 0.05 (5% partial melt, as seen in our 1050°C run) from a Main-group eucritic source can produce Stannern-group La compositions at proportions of 10 and 15% contaminant, yielding La concentrations of 4.48 to 5.11 and 5.64 to 6.64 μg/g. Even at 5%, La concentration falls just below the boundary for the Stannern group (~ 4 μg/g, [Barrat et al. 2007]) at 3.44 to 3.73 μg/g. Calculated La content in mixtures of an equivalent melt fraction for Juvinas (Barrat et al., 2007) range from 4.83 to 8.00 μg/g, which is well within Stannern-group trace element compositions. Mixtures for the 18%

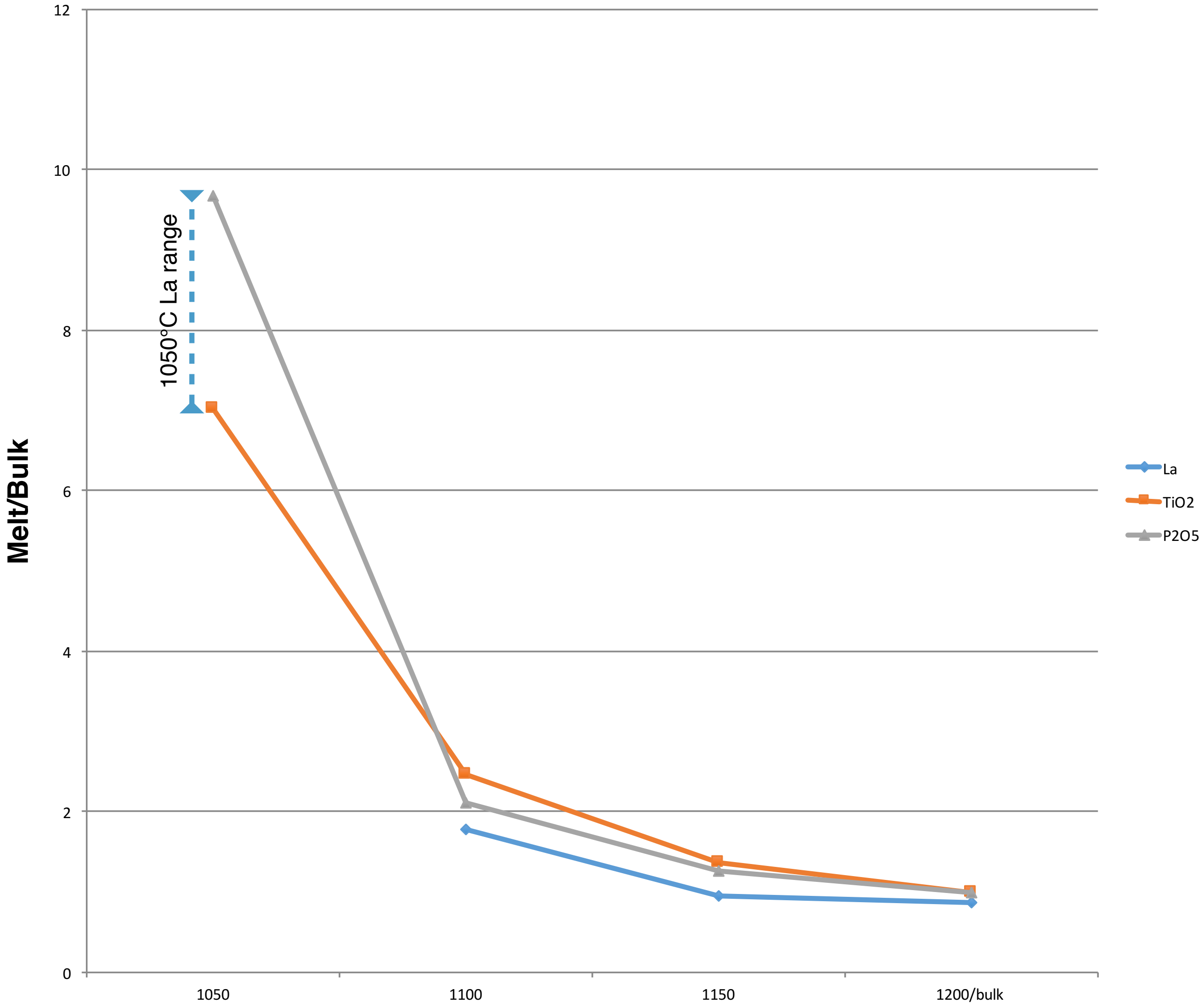

FIGURE 33: Interpolated La Enrichment in 1050°C Experiment
La enrichment was estimated using other incompatible elements (Ti and P) with similar bulk distribution coefficients as a proxy. With Ti as a lower limit and P as an upper limit, we can estimate that La enrichment would be ~700 to 970% greater in the 1050°C melt than in the bulk composition.

				La			FeO_T/MgO		
		La	FeO_T/MgO	5%	10%	15%	5%	10%	15%
NWA 8562	*Bulk*	2.52	3.64	▨	▨	▨	▨	▨	▨
	1050°C	17.67–23.34	18.61	3.44–3.73	4.48–5.11	5.64–6.64	3.88	5.12	6.90
	1100°C	4.48	8.95	2.75	3.00	3.31	3.91	4.20	4.53
HaH 262	*Bulk*	2.34	3.12	▨	▨	▨			
	1100°C	10.60	▨	2.90	3.52	4.21			
Juvinas	*Bulk*	2.72	2.61	▨	▨	▨			
	F = 0.05	40.61	▨	4.83	6.80	8.00			
	F = 0.1	23.42	▨	3.80	4.75	5.80			
	F = 0.15	16.45	▨	3.58	4.55	5.62			

Table 7: Calculated Magma Mixtures
Data for NWA 8562 is from this study, HaH 262 taken from Yamaguchi et al. (2013), and Juvinas from Barrat et al. (2007). Resultant compositions for La and FeO_T/MgO were calculated using simple binary mixing equations (DePaolo, 1981) for 5, 10, and 15% partial melt mixtures. Insufficient data from the other two studies prohibited calculation of resultant FeO_T/MgO mixtures for HaH 262 and Juvinas.

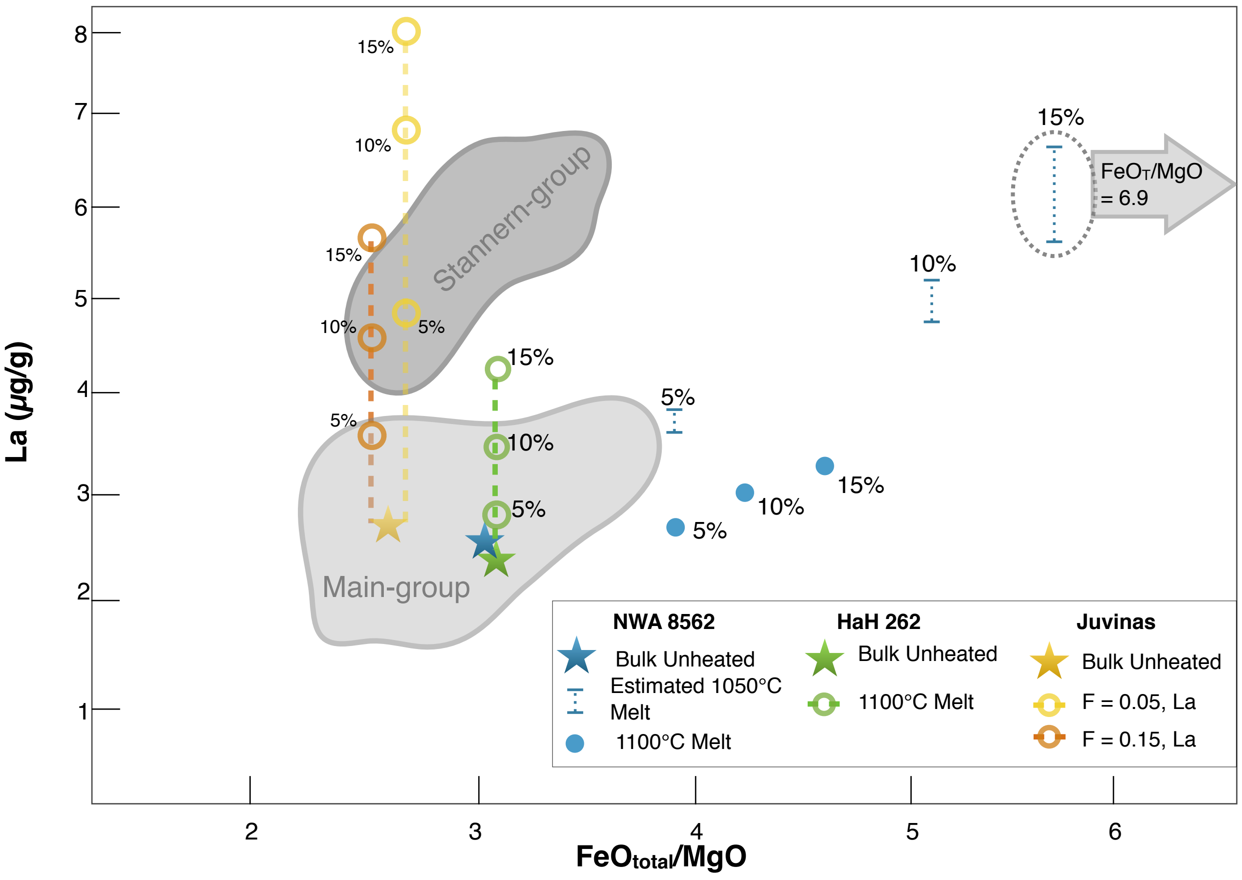

Figure 34: La vs. FeO_T/MgO Assimilation Trends
Compositional trends for 1100°C melt/bulk mixtures were calculated for NWA 8562 from LA-ICP-MS and EMPA results. Mixtures of 5, 10, and 15% contaminant were calculated according to simple binary mixing equations (DePaolo, 1981). La mixtures for HaH 262 were calculated from data in Yamaguchi et al. (2013). FeO_T/MgO for HaH 262 and Juvinas could not be calculated from available data (Barrat et al., 2007; Yamaguchi et al., 2013). These series are plotted as open circles along dashed lines, and have no x-axis value. Fields for Stannern and Main-group compositions were drawn from Barrat et al. (2007).

melt fraction (F= 0.18) produced in our 1100°C experiment did not produce Stannern-group compositions at any proportion, with the highest La concentration at 3.31 in the 15% contaminant mixture. In contrast, La content in the mixtures calculated for the 1100°C HaH 262 melt products (Yamaguchi et al., 2013) range from 2.9 to 4.2 *μ*g/g (Table 6, Figure 31). The HaH 262 mixture with the highest proportion of contaminant (15%) falls within limits of Stannern-group trace elements, unlike any of the proportions calculated for NWA 8562 melt products at the same temperature. This is likely due to the abundance of apatite in HaH 262 (Yamaguchi et al., 2013), which is an important carrier phase for REEs (Hsu and Crozaz, 1996). Juvinas mixtures at a melt fraction of 15% (F= 0.15) range from 3.58 to 5.62 *μ*g/g. Melt compositions for our 1150°C run only vary slightly from bulk compositions, so they will not be discussed in this section.

While trace element data alone may appear promising for the model, the distinction between Stannern-group and Main-group eucrites also rests on major element contents, and the correlation of incompatible trace element abundance with a differentiation index is necessary for full assessment of the model. Major element compositions of the magma mixtures are not only important in determining the degree of differentiation experienced by a eucrite, but they also determine the modal abundance of minerals that crystallize in equilibrium with the melt. Consequently, bulk composition that is not representative of the eucritic suite would probably not resemble the eucrite mineral assemblage. Data for major element modeling was not provided by Barrat et al. (2007), most likely because major element modeling during partial melting requires the consideration of variables such as crystal geometry (Hanson et al., 1978). However, our experimentally-derived values circumvent this complication. The results of our experiments are problematic for the model in question, as mixtures of melt contaminant and Main-group magmas produce compositions that are far too ferroan for eucritic assemblages (Figure 31). The extrapolated trace element compositions for 1050°C mixtures may fall within the Stannern-group, but Mg-numbers (correspondingly, FeO_T/MgO) do not. The 5% mixture yields a FeO_T/MgO ratio (3.88) at the ferroan end of the Main-group field. The 10 and 15% mixtures of the 1050°C contaminant are far too ferroan for eucritic compositions (FeO_T/MgO= 5.12 and 6.90, respectively). In fact, values for partial melt mixtures at this temperature appear to follow a magmatic fractionation trend from the Nuevo-Laredo group (bound by the most ferroan endmembers of the Main-group field in Figure 34). The processes outlined by Barrat et al. (2007) may instead more adequately explain the petrogenesis of Nuevo-Laredo group eucrites from the low-percent partial melting and assimilation of more magnesian, LREE-depleted eucrites into Main-group magmas. It is possible that melting of ferroan olivine in the mesostasis contributed appreciably to FeO enrichment in our experiments. For the 1100°C run, the 5% mixture plots near the ferroan end of the Main-group field (FeO_T/MgO = 3.91). The 10 and 15% mixtures yield greater La values (3.00–3.31), and the compositions of those mixtures are too ferroan for eucrites, with FeO_T/MgO ranging up to 4.53. One of the major weaknesses of the Barrat et al. (2007) model is that it does not take into account the contribution of minor and accessory phases, where the majority of REEs are held (Hsu and Crozaz, 1996; Yamaguchi et al., 2013). Additionally, partially melting pyroxene in the model is assumed to be 87% orthopyroxene (Barrat et al., 2007), which would seem to be a diogenite-like composition, rather than eucritic. This may be the Achilles heel of the Barrat et al. (2007) study, unless their choice of terminology included pigeonite, which is technically a clinopyroxene. The selection of Juvinas to represent Main-group magma compositions in their model may also have a role to play in the discrepancies between our results and their calculated values, as Juvinas is significantly less Fe-rich than NWA 8562 or HaH 262 (Table 6 and Figure 31). Potentially, a more Mg-rich eucrite that is enriched in incompatible elements may yield Stannern-group compositions under similar experimental conditions.

6.0 Conclusions

Lacking REE data for both the 1050°C experimental melt and the accessory phases in the unheated material prohibits us from fully assessing the Barrat et al. (2007) model of partial melt assimilation. However, we can place new constraints on the model, and further analyses based on those presented here may tell us if the model can reasonably explain Stannern-group eucrite petrogenesis.

- We have shown that Stannern-group compositions could not be reproduced by the calculated binary mixing of experimentally-derived, extensively melted ($F \geq 0.15$) Main-group eucritic material (specifically NWA 8562), as suggested by Barrat et al. (2007).
- According to our results, the model would only satisfy trace element constraints for Stannern-group petrogenesis at our lowest melt fractions ($F \approx 0.05$), as the interpolated values for La content in the 1050°C melt products yield Stannern-group compositions at proportions of >5% contaminant.
- Increasingly ferroan compositions of melt/magma mixtures for the lowest-percent melt fractions preclude the plausibility of Stannern-group petrogenesis via Barrat et al. (2007) for lithologies similar to NWA 8562. Additionally, experiments by Yamaguchi et al. (2013) found that the majority of REEs in their melt products were sourced form mesostasis apatite, which was not identified in NWA 8562. The majority of phosphorus observed in our unheated sample appears to exist as inclusions in mesostasis fayalite, according to EMPA data. If melts sourced from fayalite are major contributors to REE enrichment, then the ferroan melts produced in our experiments could be explained.

6.1 Future Work

The most pertinent subsequent research to be pursued is further analysis of the 1050°C experimental charge. We will thoroughly analyze both the melt and the accessory minerals in this sample and the original unheated material. The data we collect will allow us to more quantitatively assess the Barrat et al. (2007) model, and should yield results that are appropriate for publication. Furthermore, data obtained would be a valuable addition to the geochemical database for basaltic achondrites, as the acquisition of trace element data for the unheated accessory phases, 1050°C melts, and residual phases would allow us to calculate experimentally derived distribution coefficients for REEs in accessory minerals and partial melts. The choice of a 20 μm beam-size in EMPA of major phases in the present study was not suitable for detailed petrogenetic analysis of pyroxenes. A smaller beam-size would yield data that are far more suitable for purposes of publication. If further experimentation and/or analyses reveal that Stannern-group compositions can be generated from the assimilation of partial melts, it would place constraints on the type of environment in which this could occur, favoring models that employ serial magmatism as the source of the HED assemblage (e.g. Mandler and Elkins-Tanton, 2013; Neumann et al., 2014). Additionally, the energy required to melt crustal material of similar composition to the magma chamber would likely require recharge within magma chambers to result in simple binary magma mixing as suggested by Barrat et al. (2007), which would contrast with partial melting models that explain Stannern-trend eucrites as low-percent partial melts derived from source regions compositionally distinct from Main-group eucrites (Stolper, 1977).

Distribution of incompatible elements also has implications for the timing of petrological processes on the HED parent body: according to the model, Main-group and Stannern-group eucrites would have crystallized contemporaneously, in contrast to some Hf-W isotopic dating studies (e.g. Touboul et al., 2015) that placed Stannern-eucrite formation earlier in the history of the HED parent body than that of main-group eucrites. Hf-W isotopic ratios would be altered by partial melting events, obscuring the sequence of differentiation events.

If Stannern-group eucrite petrogenesis cannot be explained by the Barrat et al. (2007) model, then magma ocean models for HED parent body petrogenesis require modification, as they cannot account for the compositions of all eucrites (Barrat et al., 2007; Mandler and Elkins-Tanton, 2013; Mittlefehldt, 2015). Stolper (1977) suggested that Stannern-group eucrites may have crystallized from primary partial melts that were sourced from regions compositionally distinct from those of Main-group eucrites, or from early, low percent partial melts of a common source region. He explained the relative scarcity of Stannern-group eucrites in the meteoritical record by suggesting that primary, low melt percent magmas would not easily migrate to the surface of an undifferentiated body. Although partial melting models have historically contrasted with magma ocean models, the earliest stages of melting on a planetary body likely reflected many of the same conditions described in partial melting, prior to serial magmatism (e.g. Mandler and Elkins-Tanton, 2013; Neumann et al., 2014; Greenwood et al., 2005). If early, low percent partial melts became entrapped and crystallized in the outer regions of the HED parent body, then increasing degrees of magmatism may partially or completely melt those lithologies. Assimilation of this material within Main-group eucritic magmas would result in regional variations in basaltic magma compositions that could reflect those of the Stannern-group eucrites (Figure 35). Additional melt experiments at lower temperatures for longer periods (e.g. 1025°C for 48 hours) may yield a greater percent partial melt that is solely derived from mesostasis phases (e.g. Stolper, 1977; Yamaguchi et al., 2013), which would more accurately reflect primary, low percent partial melts. Incorporation of data obtained from these experiments may help to further constrain Stannern-group petrogenesis.

Follow-up research could analyze the major and trace element compositions of relict minerals, as well as petrographic features produced by partial melting. This data could then be compared to highly metamorphosed eucrites (e.g. Yamaguchi et al., 2011) to determine if any direct evidence of partial melting occurred according to processes described in the model in question. Highly metamorphosed eucrites are depleted in LREEs, and show a fine-grained granoblastic texture, suggesting that they are residues of partial melting (Yamaguchi et al., 2011). Preliminary investigations into the textures and LREE distribution of highly metamorphosed eucrites and the residual phases in our experiments suggest a potential correlation.

Yamaguchi et al. (2013) found that Ca-phosphates could carry REEs over significant (μm-scale) distances in as little as 24 hours at low pressure, providing a transport mechanism for extremely low partial melt fractions (F< 0.05). High-resolution CAT scans of the experimental

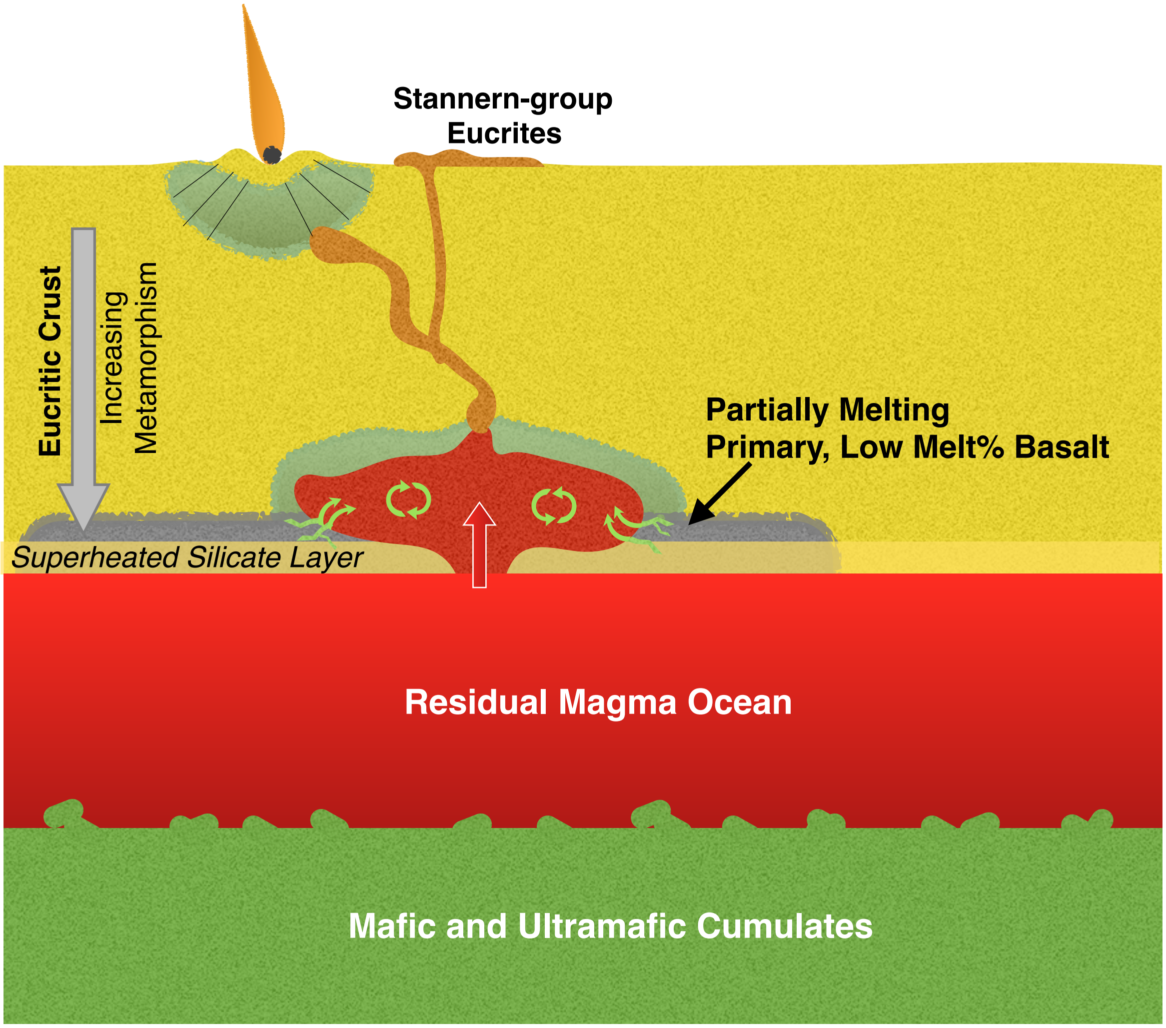

Figure 35: Alternate Model of Stannern-group Eucrite Petrogenesis
At a stage in the earliest, lowest melt fraction partial melts of the bulk HED parent body had not been completely consumed (e.g. Stolper, 1977; Neumann et al., 2014), partial melting of that material may account for compositional variations in the eucrite suite that are currently unexplained by petrogenetic models for the HED parent body. Adapted from Barrat et al. (2007), and Neumann et al. (2014). The partially melting primary basalt was added by this study.

charges may show further transport mechanisms for incompatible elements and help constrain factors such as how much time would be required for melt migration over a given distance. Dr. Wenlu Zhu at the University of Maryland has developed such a technique, and has expressed an interest in pursuing this research with me.

References

Anders, E., and Grevesse, N., 1989, Abundances of the elements: Meteoritic and solar: Geochimica Et Cosmochimica Acta, v. 53, p. 197-214, doi: http://dx.doi.org.ezproxy.tcu.edu/10.1016/0016-7037(89)90286-X.

Barrat, J., and Yamaguchi, A., 2014, Comment on "The origin of eucrites, diogenites, and olivine diogenites: Magma ocean crystallization and shallow magma processes on Vesta" by B. E. Mandler and L. T. Elkins-Tanton: Meteoritics and Planetary Science, v. 49, p. 468-472, doi: 10.1111/maps.12250.

Barrat, J.A., Yamaguchi, A., Bunch, T.E., Bohn, M., Bollinger, C., and Ceuleneer, G., 2011, Possible fluid-rock interactions on differentiated asteroids recorded in eucritic meteorites: Geochimica Et Cosmochimica Acta, v. 75, p. 3839-3852, doi: 10.1016/j.gca.2011.04.013.

Barrat, J.A., Yamaguchi, A., Greenwood, R.C., Benoit, M., Cotten, J., Bohn, M., and Franchi, I.A., 2008, Geochemistry of diogenites; still more diversity in their parental melts: Meteoritics & Planetary Science, v. 43, p. 1759-1775.

Barrat, J.A., Yamaguchi, A., Greenwood, R.C., Bohn, M., Cotten, J., Benoit, M., and Franchi, I.A., 2007, The Stannern trend eucrites: Contamination of main group eucritic magmas by crustal partial melts: Geochimica Et Cosmochimica Acta, v. 71, p. 4108-4124, doi: http://dx.doi.org.ezproxy.tcu.edu/10.1016/j.gca.2007.06.001.

Beck, A.W., Sunshine, J.M., McCoy, T.J., and Hiroi, T., 2012, Challenges to Finding Olivine on the Surface of 4 Vesta, Lunar and Planetary Science Conference, XLIII, #2218.

Bogard, D., 1983, A meteorite from the Moon: Geophysical Research Letters, v. 10, p. 773-773, doi: 10.1029/GL010i009p00773.

Burbine, T.H., Meibom, A., and Binzel, R.P., 1996, Mantle material in the main belt: Battered to bits? Meteoritics & Planetary Science, v. 31, p. 607-620, doi: 10.1111/j.1945-5100.1996.tb02033.x.

Clayton, R.N., Grossman, L., and and Mayeda, T.K., 1973, A component of primitive nuclear composition in carbonaceous meteorites: Science, v. 182, p. 485-488.

Clayton, R.N., and Mayeda, T.K., 1996, Oxygen isotope studies of achondrites: Geochimica Et Cosmochimica Acta, v. 60, p. 1999-2017, doi: http://dx.doi.org.ezproxy.tcu.edu/10.1016/0016-7037(96)00074-9.

Clayton, R.N., and Mayeda, T.K., 1983, Oxygen isotopes in eucrites, shergottites, nakhlites, and chassignites: Earth and Planetary Science Letters, v. 62, p. 1-6, doi: http://dx.doi.org.ezproxy.tcu.edu/10.1016/0012-821X(83)90066-3.

Clayton, R.N., Mayeda, T.K., Goswami, J.N., and Olsen, E.J., 1991, Oxygen isotope studies of ordinary chondrites: Geochimica Et Cosmochimica Acta, v. 55, p. 2317-2337, doi: http://dx.doi.org.ezproxy.tcu.edu/10.1016/0016-7037(91)90107-G.

Clayton, R.N., Mayeda, T.K., and Rubin, A.E., 1984, Oxygen isotopic compositions of enstatite chondrites and aubrites; Journal of Geophysical Research, v. 89, p. 245-249.

Consolmagno, G.J., and Drake, M.J., 1977, Composition and evolution of the eucrite parent body; evidence from rare earth elements: Geochimica Et Cosmochimica Acta, v. 41, p. 1271-1282.

DePaolo, D.J., 1981, Trace element and isotopic effects of combined wallrock assimilation and fractional crystallization: Earth and Planetary Science Letters, v. 53, p. 189-202, doi: http://dx.doi.org/10.1016/0012-821X(81)90153-9.

De Sanctis, M.C., Ammannito, E., Capria, M.T., Tosi, F., Capaccioni, F., Zambon, F., Carraro, F., Fonte, S., Frigeri, A., Jaumann, R., Magni, G., Marchi, S., McCord, T.B., McFadden, L.A., McSween, H.Y., Mittlefehldt, D.W., Nathues, A., Palomba, E., Pieters, C.M., Raymond, C.A., Russell, C.T., Toplis, M.J., and Turrini, D., 2012, Spectroscopic characterization of mineralogy and its diversity across Vesta: Science, v. 336, p. 697-700, doi: http://dx.doi.org.ezproxy.tcu.edu/10.1126/science.1219270.

Duke, M.B., and Silver, L.T., 1967, Petrology of eucrites, howardites and mesosiderites: Geochimica Et Cosmochimica Acta, v. 31, p. 1637-1665, doi: http://dx.doi.org.ezproxy.tcu.edu/10.1016/0016-7037(67)90112-3.

Fredriksson, K., and Keil, K., 1963, The light-dark structure in the Pantar and Kapoeta stone meteorites: Geochimica Et Cosmochimica Acta, v. 27, p. 717, doi: 10.1016/0016-7037(63)90038-3.

Fu, R.R., Weiss, B.P., Shuster, D.L., Gattacceca, J., Grove, T.L., Suavet, C., Lima, E.A., Li, L., and Kuan, A.T., 2012, An ancient core dynamo in Asteroid Vesta: Science, v. 338, p. 238-241, doi: http://dx.doi.org.ezproxy.tcu.edu/10.1126/science.1225648.

Gaffey, M.J., 1976, Spectral reflectance characteristics of the meteorite classes: Journal of Geophysical Research, v. 81, p. 905-920, doi: http://dx.doi.org/10.1029/JB081i005p00905.

Ghosh, A., and McSween Jr., H.Y., 1998, A Thermal Model for the Differentiation of Asteroid 4 Vesta, Based on Radiogenic Heating: Icarus, v. 134, p. 187-206, doi: http://dx.doi.org.ezproxy.tcu.edu/10.1006/icar.1998.5956.

Greenwood, R.C., Barrat, J., Scott, E.R.D., Haack, H., Buchanan, P.C., Franchi, I.A., Yamaguchi, A., Johnson, D., Bevan, A.W.R., and Burbine, T.H., 2015, Geochemistry and oxygen isotope composition of main-group pallasites and olivine-rich clasts in mesosiderites: Implications for the "Great Dunite Shortage" and HED-mesosiderite connection: Geochimica Et Cosmochimica Acta, v. 169, p. 115-136, doi: 10.1016/j.gca.2015.07.023.

Greenwood, R.C., Franchi, I.A., Jambon, A., Barrat, J.A., and Burbine, T.H., 2006, Oxygen isotope variation in stony-iron meteorites: Science, v. 313, p. 1763-1765, doi: http://dx.doi.org.ezproxy.tcu.edu/10.1126/science.1128865.

Greenwood, R.C., Franchi, I.A., Jambon, A., and Buchanan, P.C., 2005, Widespread magma oceans on asteroidal bodies in the early Solar System: Nature, v. 435, p. 916-918, doi: 10.1038/nature03612.

Greenwood, R.C., Barrat, J., Yamaguchi, A., Franchi, I.A., Scott, E.R.D., Bottke, W.F., and Gibson, J.M., 2014, The oxygen isotope composition of diogenites: Evidence for early global melting on a single, compositionally diverse, HED parent body: Earth and Planetary Science Letters, v. 390, p. 165-174, doi: http://dx.doi.org.ezproxy.tcu.edu/10.1016/j.epsl.2013.12.011.

Gupta, G., and Sahijpal, S., 2010, Differentiation of Vesta and the parent bodies of other achondrites: Journal of Geophysical Research, v. 115, p. Citation E08001, doi: http://dx.doi.org.ezproxy.tcu.edu/10.1029/2009JE003525.

Hanson, G. N., Langmuir, C. H., Drake, M. J., & Holloway, J. R., 1978, Modeling of major elements in mantle-melt systems using trace element approaches. Geochimica et Cosmochimica Acta, v. 42, p. 725-742

Herzog, G.F., Davis, A.M., Holland, H.D., and Turekian, K.K., 2005, Cosmic-ray Exposure Ages of Meteorites: Treatise on Geochemistry, v. 1, p. 347-380.

Hsu, W., and Crozaz, G., 1996, Mineral chemistry and the petrogenesis of eucrites: I. Noncumulate eucrites: Geochimica Et Cosmochimica Acta, v. 60, p. 4571-4591, doi: 10.1016/S0016-7037(96)00277-3.

Hublet, G., Debaille, V., Wimpenny, J., and Yin, Q.Z., 2013, Geological history of 4-Vesta; (super 26) Al- (super 26) Mg dating on eucrites and diogenites: Mineralogical Magazine, v. 77, p. 1343, doi: http://dx.doi.org.ezproxy.tcu.edu/10.1180/minmag.2013.077.5.8.

Ikeda, Y., and Takeda, H., 1985, A model for the origin of basaltic achondrites based on the Yamato 7308 howardite: Journal of Geophysical Research, v. 90, p. 649-663.

Jurewicz, A.J.G., Mittlefehldt, D.W., and Jones, J.H., 1993, Experimental partial melting of the Allende (CV) and Murchison (CM) chondrites and the origin of asteroidal basalt: Geochimica Et Cosmochimica Acta, v. 57, p. 2123-2139, doi: 10.1016/0016-7037(93)90098-H.

Jurewicz, A.J.G., Mittlefehldt, D.W., and Jones, J.H., 1995, Experimental partial melting of the St. Severin (LL) and Lost City (H) chondrites: Geochimica Et Cosmochimica Acta, v. 59, p. 391-408, doi: 10.1016/0016-7037(94)00328-J.

Krot, A.N., Keil, K., Scott, E.R.D., Goodrich, C.A., and Weisberg, M.K., 2014, 1.1 - Classification of Meteorites and Their Genetic Relationships, in Holland, H.D. and Turekian, K.K., Treatise on Geochemistry (Second Edition): Oxford, Elsevier, p. 1-63.

Marchi, S., Massironi, M., Vincent, J.-., Morbidelli, A., Mottola, S., Marzari, F., Küppers, M., Besse, S., Thomas, N., Barbieri, C., Naletto, G., and Sierks, H., 2012, The cratering history of asteroid (21) Lutetia: Planetary and Space Science, v. 66, p. 87-95, doi: http://dx.doi.org.ezproxy.tcu.edu/10.1016/j.pss.2011.10.010.

Mason, B., 1962. Meteorites: (Wiley) New York, NY, p. 1-286

Mandler, B.E., and Elkins-Tanton, L.T., 2013, The origin of eucrites, diogenites, and olivine diogenites: Magma ocean crystallization and shallow magma chamber processes on Vesta: Meteoritics and Planetary Science, v. 48, p. 2333-2349, doi: 10.1111/maps.12135.

Mayne, R.G., McSween, H.Y., Jr., McCoy, T.J., and Gale, A., 2009, Petrology of the unbrecciated eucrites: Geochimica Et Cosmochimica Acta, v. 73, p. 794-819, doi: 10.1016/j.gca.2008.10.035.

McCord, T.B., Adams, J.B., and Johnson, T.V., 1970, Asteroid Vesta; spectral reflectivity and compositional implications: Science, v. 168, p. 1445-1447.

McSween, H.Y.,Jr, Binzel, R.P., De Sanctis, M.C., Ammannito, E., Prettyman, T.H., Beck, A.W., Reddy, V., Corre, L., Gaffey, M.J., McCord, T.B., Raymond, C.A., and Russell, C.T., 2013(a), Dawn; the Vesta-HED connection; and the geologic context for eucrites, diogenites, and howardites: Meteoritics & Planetary Science, v. 48, p. 2090-2104, doi: http://dx.doi.org/10.1111/maps.12108.

McSween, H.Y., Ammannito, E., Reddy, V., Prettyman, T.H., Beck, A.W., Cristina De Sanctis, M., Nathues, A., Corre, L.L., O'Brien, D.P., Yamashita, N., McCoy, T.J., Mittlefehldt, D.W., Toplis, M.J., Schenk, P., Palomba, E., Turrini, D., Tosi, F., Zambon, F., Longobardo, A., Capaccioni, F., Raymond, C.A., and Russell, C.T., 2013(b), Composition of the Rheasilvia Basin, a window into Vesta's interior: Journal of Geophysical Research: Planets, v. 118, p. 335-346, doi: http://dx.doi.org.ezproxy.tcu.edu/10.1002/jgre.20057.

McSween, H.Y., Mittlefehldt, D.W., Beck, A.W., Mayne, R.G., and McCoy, T.J., 2011, HED Meteorites and Their Relationship to the Geology of Vesta and the Dawn Mission: Space Science Reviews, v. 163, p. 141-174, doi: 10.1007/s11214-010-9637-z.

Merrill, R.B., and Williams, R.J., 1975, The system anorthite-forsterite-fayalite-silica to 2 kbar with lunar petrologic applications: Lunar and Planetary Science VI , p. 959-971.

Miller, M.F., Franchi, I.A., and Pillinger, C.T., 1999, The Mass-dependent Oxygen-Isotopic Fractionation Line: New Measurements and the Need for a Reporting Consensus: Ninth Annual V. M. Goldschmidt Conference, #7433.

Mittlefehldt, D., 2005, Ibitira: A basaltic achondrite from a distinct parent asteroid and implications for the Dawn mission: Meteoritics and Planetary Science, v. 40, p. 665, doi: 10.1111/j.1945-5100.2005.tb00972.x.

Mittlefehldt, D.W., 1994, The genesis of diogenites and HED parent body petrogenesis: Geochimica Et Cosmochimica Acta, v. 58, p. 1537, doi: 10.1016/0016-7037(94)90555-X.

Mittlefehldt, D.W., 2015, Asteroid (4) Vesta: I. The howardite-eucrite-diogenite (HED) clan of meteorites: Chemie Der Erde / Geochemistry, v. 75, p. 155-183, doi: 10.1016/j.chemer.2014.08.002.

Mittlefehldt, D.W., and Lindstrom, M.M., 1997, Magnesian basalt clasts from the EET 92014 and Kapoeta howardites and a discussion of alleged primary magnesian HED basalts: Geochimica Et Cosmochimica Acta, v. 61, p. 453-462, doi: 10.1016/S0016-7037(96)00357-2.

Mittlefehldt, D.W., and Lindstrom, M.M., 2003, Geochemistry of eucrites: genesis of basaltic eucrites, and Hf and Ta as petrogenetic indicators for altered antarctic eucrites: Geochimica Et Cosmochimica Acta, v. 67, p. 1911-1934, doi: 10.1016/S0016-7037(02)01411-4.

Nesvorný, D., Roig, F., Gladman, B., Lazzaro, D., Carruba, V., and Mothé-Diniz, T., 2008, Fugitives from the Vesta family: Icarus, v. 193, p. 85-95, doi: http://dx.doi.org.ezproxy.tcu.edu/10.1016/j.icarus.2007.08.034.

Neumann, W., Breuer, D., and Spohn, T., 2014, Differentiation of Vesta: Implications for a shallow magma ocean: Earth and Planetary Science Letters, v. 395, p. 267-280, doi: http://dx.doi.org.ezproxy.tcu.edu/10.1016/j.epsl.2014.03.033.

Norman, M., Garcia, M., Pietruszka, A., 2005, Trace-element distribution coefficients for pyroxenes, plagioclase, and olivine in evolved tholeiites from the 1955 eruption of Kilauea Volcano, Hawai'i, and petrogenesis of differentiated rift-zone lava: American Mineralogist, v. 90, p. 888-899, doi: 10.2138/am.2005.1780

Nyquist, L.E., Takeda, H., Bansal, B.M., Shih, C.-., and Wiesmann, H., 1986, Rb-Sr and Sm-Nd internal isochron ages of a subophitic basalt clast and a matrix sample from the Y75011 eucrite: Journal of Geophysical Research, v. 91, p. 8137-8150, doi: 10.1029/JB091iB08p08137.

O'Hara, M.J., 1968, The bearing of phase equilibria studies in synthetic and natural systems on the origin and evolution of basic and ultrabasic rocks: Earth-Science Reviews, v. 4, p. 69-133, doi: http://dx.doi.org.ezproxy.tcu.edu/10.1016/0012-8252(68)90147-5.

Papike, J.J., 1998, Comparative planetary mineralogy: comparison of melt-derived pyroxene, feldspar, and olivine: Lunar and Planetary Science, XXIX, #1008.

Papike, J.J., Karner, J.M., and Shearer, C.K., 2003, Determination of planetary basalt parentage: a simple technique using the electron microprobe: American Mineralogy, v. 88, p. 469-472.

Palme, H., and Rammensee, W., 1981, The cosmic abundance of molybdenum: Earth and Planetary Science Letters, v. 55, p. 356-362, doi: 10.1016/0012-821X(81)90163-1.

Parker, A., Ivezić, Ž., Jurić, M., Lupton, R., Sekora, M.D., and Kowalski, A., 2008, The size distributions of asteroid families in the SDSS Moving Object Catalog 4: Icarus, v. 198, p. 138-155, doi: http://dx.doi.org.ezproxy.tcu.edu/10.1016/j.icarus.2008.07.002.

Pun, A. and Papike, J.J., 1996, Unequilibrated eucrites and the equilibrated Juvinas eucrite: pyroxene REE systematics and major, minor, and trace element zoning: American Mineralogy, v. 81, p. 1438-1451.

Righter, K., and Drake, M.J., 1997, A magma ocean on Vesta; core formation and petrogenesis of eucrites and diogenites: Meteoritics & Planetary Science, v. 32, p. 929-944.

Ruzicka, A., Snyder, G.A., and Taylor, L.A., 1997, Vesta as the howardite, eucrite and diogenite parent body; implications for the size of a core and for large-scale differentiation: Meteoritics & Planetary Science, v. 32, p. 825-840.

Schwartz, J. M., & McCallum, I. S., 2005, Comparative study of equilibrated and unequilibrated eucrites; subsolidus thermal histories of haraiya and pasamonte: American Mineralogist, v. 90, p. 1871-1886. doi:http://dx.doi.org/10.2138/am.2005.1733

Shearer, C.K., Fowler, G.W., and Papike, J.J., 1997, Petrogenetic models for magmatism on the eucrite parent body: Evidence from ort hopyroxene in diogenites: Meteoritics and Planetary Science, v. 32, doi: 10.1111/j.1945-5100.1997.tb01578.x.

Stolper, E., 1977, Experimental petrology of eucritic meteorites: Geochimica Et Cosmochimica Acta, v. 41, p. 587-611, doi: http://dx.doi.org.ezproxy.tcu.edu/10.1016/0016-7037(77)90300-3.

Stolper, E., 1975, Petrogenesis of eucrite, howardite and diogenite meteorites: Nature (London), v. 258, p. 220-222.

Stolper, E., and McSween, H.Y., Jr., 1979, Petrology and origin of the shergottite meteorites: Geochimica Et Cosmochimica Acta, v. 43, p. 1475-1477, doi: 10.1016/0016-7037(79)90142-X.

Takeda, H., Mori, H., Ryder, G., and Schubert, G., 1985, The diogenite-eucrite links and the crystallization history of a crust of their parent body: Journal of Geophysical Research, v. 90, p. 636-648.

Takeda, H., and Graham, A.L., 1991, Degree of equilibration of eucritic pyroxenes and thermal metamorphism of the earliest planetary crust: Meteoritics, v. 26, p. 129-134.

Thomas, P.C., Binzel, R.P., Gaffey, M.J., Zellner, B.H., Storrs, A.D., and Wells, E., 1997, Vesta: Spin Pole, Size, and Shape from HST Images: Icarus, v. 128, p. 88-94, doi: http://dx.doi.org/10.1006/icar.1997.5736.

Touboul, M., Sprung, P., Aciego, S.M., Bourdon, B., and Kleine, T., 2015, Hf–W chronology of the eucrite parent body: Geochimica Et Cosmochimica Acta, v. 156, p. 106-121, doi: http://dx.doi.org.ezproxy.tcu.edu/10.1016/j.gca.2015.02.018.

Treiman, A.H., Lanzirotti, A., and Xirouchakis, D., 2004, Ancient water on asteroid 4 Vesta: evidence from a quartz veinlet in the Serra de Magé eucrite meteorite: Earth and Planetary Science Letters, v. 219, p. 189-199, doi: http://dx.doi.org.ezproxy.tcu.edu/10.1016/S0012-821X(04)00004-4.

Tsiganis, K., Gomes, R., Morbidelli, A., and Levison, H.F., 2005, Origin of the orbital architecture of the giant planets of the Solar System: Nature, v. 435, p. 459-461, doi: 10.1038/nature03539.

Warren, P.H., 1985, Origin of howardites, diogenites and eucrites - A mass balance constraint: Geochimica Et Cosmochimica Acta, v. 49, p. 577-586, doi: 10.1016/0016-7037(85)90049-3.

Warren, P.H., and Jerde, E.A., 1987, Composition and origin of Nuevo Laredo Trend eucrites: Geochimica Et Cosmochimica Acta, v. 51, p. 713-725, doi: http://dx.doi.org/10.1016/0016-7037(87)90082-2.

Warren, P.H., 1997, MgO-FeO mass balance constraints and a more detailed model for the relationship between eucrites and diogenites: Meteoritics and Planetary Science, v. 32, p. 945-963, doi: 10.1111/j.1945-5100.1997.tb01583.x.

Warren, P.H., Rubin, A.E., Isa, J., Gessler, N., Ahn, I., and Choi, B., 2014, Northwest Africa 5738: Multistage fluid-driven secondary alteration in an extraordinarily evolved eucrite: Geochimica Et Cosmochimica Acta, v. 141, p. 199-227, doi: 10.1016/j.gca.2014.06.008.

Wasson, J.T., 2013, Vesta and extensively melted asteroids: Why HED meteorites are probably not from Vesta: Earth and Planetary Science Letters, v. 381, p. 138-146, doi: http://dx.doi.org.ezproxy.tcu.edu/10.1016/j.epsl.2013.09.002.

Wasson, J.T., Wetherill, G.W., and Gehrels, T., 1979, Dynamical chemical and isotopic evidence regarding the formation locations of asteroids and meteorites: Asteroids, University of Arizona Press, p. 926-974.

Whattam, S.A., Hewins, R.H., Cohen, B.A., Seaton, N.C., and Prior, D.J., 2008, Granoblastic olivine aggregates in magnesian chondrules: Planetesimal fragments or thermally annealed solar nebula condensates? Earth and Planetary Science Letters, v. 269, p. 200-211, doi: http://dx.doi.org/10.1016/j.epsl.2008.02.013.

Yamaguchi, A., Barrat, J.A., Greenwood, R.C., Shirai, N., Okamoto, C., Setoyanagi, T., Ebihara, M., Franchi, I.A., and Bohn, M., 2009, Crustal partial melting on Vesta: Evidence from highly metamorphosed eucrites: Geochimica Et Cosmochimica Acta, v. 73, p. 7162-7182, doi: http://dx.doi.org.ezproxy.tcu.edu/10.1016/j.gca.2009.07.037.

Yamaguchi, A., Mikouchi, T., Ito, M., Shirai, N., Barrat, J.A., Messenger, S., and Ebihara, M., 2013, Experimental evidence of fast transport of trace elements in planetary basaltic crusts by high temperature metamorphism: Earth and Planetary Science Letters, v. 368, p. 101-109, doi: http://dx.doi.org/10.1016/j.epsl.2013.02.036.

Yamaguchi, A., Barrat, J., Ito, M., and Bohn, M., 2011, Posteucritic magmatism on Vesta; evidence from the petrology and thermal history of diogenites: Journal of Geophysical Research, v. 116, p. Citation E08009, doi: http://dx.doi.org.ezproxy.tcu.edu/10.1029/2010JE003753.

Yamaguchi, A., Taylor, G.J., and Keil, K., 1997, Metamorphic history of the eucritic crust of 4 Vesta: Journal of Geophysical Research, v. 102, p. 13-13,386, doi: http://dx.doi.org.ezproxy.tcu.edu/10.1029/97JE00519.

Zhang, A., Wang, R., Hsu, W., and Bartoschewitz, R., 2013, Record of S-rich vapors on asteroid 4 Vesta: Sulfurization in the Northwest Africa 2339 eucrite: Geochimica Et Cosmochimica Acta, v. 109, p. 1-13, doi: 10.1016/j.gca.2013.01.036.

Vita

Personal	Samuel Dean Crossley Born May 14, 1988, Fort Worth, Texas Son of Sanford Lyle Crossley and Nancy Reid Crossley
Education	University of Maryland, Geology, Ph.D. (beginning August 2016) Advisors: Dr. Jessica Sunshine, Dr. Richard Ash Texas Christian University, Geology, M.S. 2016 Advisor: Dr. Rhiannon G. Mayne Hardin-Simmons University, Geology, B.Sc. 2010 Advisors: Dr. Steven Rosscoe, Dr. Mark Ouimette
Experience	Teaching Assistant, Texas Christian University, 2014-2016 Assistant Curator, Monnig Meteorite Collection, 2015-2016. Secondary Science Teacher, U.S. Peace Corps, 2011-2013. Research Associate, Geological Research Center, 2009-2010.
Publications	Crossley S.D., Mayne R.G., Lunning N.G., McCoy T.J., Greenwood R.C., Franchi I.A., 2016, Stannern-trend eucrite petrogenesis: an assessment of partial melt contamination models via experimental petrology. LPSC XLVII, Abstract 2821 Mayne, R.G., Crossley, S., Gregory, J. 2015, Analyzing Unclassified Meteorites, LPSC XLVI, Abstract 2118
Memberships	Meteortitical Society, Fellow-in-Training, 2016-present

Abstract

ARE STANNERN-GROUP EUCRITES PRODUCTS OF PARTIAL MELT CONTAMINATION? CONSTRAINING THE PETROGENESIS OF THE H.E.D. PARENT BODY THROUGH EXPERIMENTAL PETROLOGY

by Samuel D. Crossley, M.S. 2016

School of Geology, Energy, and the Environment

Texas Christian University

Thesis Advisor: Dr. Rhiannon Mayne, Associate Professor of Geology

Partial melting experiments were conducted on the eucrite NWA 8562 to assess the validity of partial melt assimilation models for Stannern-group eucrite petrogenesis. NWA 8562 petrography and major/minor element geochemistry were analyzed to assure that the meteorite met experimental parameters. Four sets of experiments were run at 1050, 1100, 1150, and 1200°C. Experimental compositions were analyzed and factored into calculations that model the mixing of melt fractions into Main-group eucritic magmas. We have shown that while partial melt mixing models for Stannern-group eucites can satisfy trace element constraints at 5% partial melting and 10-15%-contaminant mixtures, the model fails to account for extreme Fe-enrichment in melts, which yield compositions that are outside the range of eucrites. Previously modeled pyroxene compositions seem to be erroneous and require correction. Further research into accessory phase melt-contribution is required, and should be incorporated into the model.